LANCASTER UNIVERSITY

Plasma flow boundaries in the high-latitude ionosphere

by

Hannah Laurens MPhys (Hons)

This thesis is submitted in partial fulfilment of the requirements
for the degree of Doctor of Philosophy

in the
Faculty of Science and Technology
Department of Physics

October 2019

Declaration of Authorship

I, Hannah Laurens, declare that this thesis titled 'Plasma flow boundaries in the high-latitude ionosphere' and the work presented in it are my own. I confirm that:

- This work was done wholly or mainly while in candidature for a research degree at this University.
- Where any part of this thesis has previously been submitted for a degree or any other qualification at this University or any other institution, this has been clearly stated.
- Where I have consulted the published work of others, this is always clearly attributed.
- Where I have quoted from the work of others, the source is always given. With the exception of such quotations, this thesis is entirely my own work.
- I have acknowledged all main sources of help.
- Where the thesis is based on work done by myself jointly with others, I have made clear exactly what was done by others and what I have contributed myself.

Signed: _____

Date: _____

"To Mum, Dad, Grandma Jean and Grandpa Jim"

Abstract

The main component of this thesis is to investigate ionospheric flow boundaries derived from plasma convection observations and their relationship to magnetospheric boundaries. Observations of ionospheric boundaries can provide useful information on the time-dependant dynamics of the coupled solar wind-magnetosphere-ionosphere system. Ionospheric convection boundaries were inferred using an archive of data from the SuperDARN HF radar network which operates in the auroral regions of both hemispheres. Regions where the ionospheric flow reveals a change in the east-west direction, the convection reversal boundary (CRB), is a common and widely-used criterion to identify boundaries in the convection data. However, this approach can be limited in certain regions. This thesis firstly presents a new boundary identification technique, the convection curvature boundary (CCB) that is derived using a more physical interpretation of where boundaries in the convection data should lie. A statistical analysis is performed between the two different ionospheric boundaries and their applicability as a proxy for the open closed field line boundary (OCB) is tested. The CCB is found to be more robust than the CRB which tends to identify boundaries at unphysical latitudes, for example, close to the pole and at noon and midnight magnetic local times (MLTs) where it becomes less well defined. The noon region in particular shows that the CCB identifies boundaries at latitudes more consistent with theoretical considerations, especially when asymmetries are introduced into the ionospheric convection as a result of a B_y-dominated interplanetary magnetic field (IMF). Results from a statistical analysis comparing the poleward auroral boundary revealed that the CCB aligned more closely at almost all MLTs. It was found that CRB and CCB location is dependant on the amount of local radar coverage at certain MLT sectors but that with sufficient coverage the CCB can provide an extremely good proxy for the poleward auroral boundary to within 1° magnetic latitude. Finally, a discussion of further work is given following some of the implications of the statistical results. In particular, the relationship between the effect of radar coverage and magnetotail phenomena (such as substorms), both of which have an effect on the resulting convection pattern, was investigated. Initial results suggest that measurements of the nightside ionospheric convection were modified by the location of radar coverage across the map and variations in the amount of radar coverage over the substorm period were ordered relative to the substorm onset location.

Acknowledgements

I would like to take a moment to recognise the people and institutions that have contributed to this thesis and enabled this work to be possible.

I cannot thank my PhD supervisor, Dr. Adrian Grocott enough. As a mentor he has always been available for discussions about my work, helping me develop my own ideas and encouraging me to believe in myself, especially when I felt I had lost my way. His guidance and patience throughout my PhD have been essential and I am grateful for every physics discussion, honest conversation and pep talk.

The SPP office crew will always hold a special place in my memory as colleagues and students became my friends. I am ever grateful to them for keeping my social life active, from 'one-drink' pub trips on a Friday, clambering the trees in Grizedale forest and eating too many treats in the 3-month long SPP bake-off competition. The relationships forged throughout my time at Lancaster University have defined my twenties and I am left with a lot of memories that wont soon be forgotten!

Although many people in my life have helped keep me going at one point or another there a few people that I feel should be mentioned by name. I say thank you to Jamie Walker for his continuing belief in me, for being my rock and for standing by my side when things were hard. I must also recognise my mum and dad, I am incredibly lucky to have such supportive, caring parents and their contribution to my PhD life cannot be understated.

Of course, this thesis would not have been possible without use of data provided by the SuperDARN radars. I want to thank the multiple institutions and PIs who contribute to the maintenance of the radars and provision of high-quality data for analysis. I have been lucky enough to present my work to the community at two SuperDARN workshops. I am so grateful for these opportunities to travel and experience other cultures as part of this friendly group of international scientists.

My final thank you is to Lancaster University, my home as a student for over 8 years. A thank you to the Faculty of Science and Technology for funding my PhD, without this scholarship, this thesis would certainly not be here today. I must also thank the Physics department for the rewarding teaching and outreach opportunities I have been able to be a part of. They have enriched my experiences of being a student here and although my time at Lancaster is nearly at its end, I will always remain a red-rose at heart!

Contents

List of Figures

List of Tables

Physical Constants

Astronomical Unit	AU	=	1.49598×10^{11} m
Boltzmann Constant	k_B	=	$1.38065 \times 10^{23}\mathrm{JK}^{-1}$
Electron Volt	eV	=	1.60218×10^{-19} J
Earth radius (mean)	R_E	=	6.371×10^{6} m
Solar mass	$M_\odot$	=	1.98855×10^{30} kg
Solar radius	$R_\odot$	=	6.995×10^{8} m
Speed of Light	c	=	2.99792×10^{8} ms$^{-\mathrm{s}}$
Vacuum Permittivity	ϵ_0	=	8.85419×10^{-12} Fm^{-1}

Chapter 1

Introduction and basic theory

This thesis is concerned with solar wind - magnetosphere coupling which describes the interaction between the Earth's magnetic field and the interplanetary environment. This coupling between the Earth's magnetic field and the solar wind induces characteristic plasma flows in the ionosphere at high latitudes. The nature of these ionospheric plasma flows are intricately related to physical processes that occur in the magnetosphere. For example, discontinuities in the flow pattern can relate to precipitation boundaries in the auroral oval. A change in the east-west direction of the flow is a simple and widely-used criterion to elucidate the locations of these discontinuities but this approach can be limited in certain regions. The main component of this thesis is the derivation of a new boundary based on a more physical interpretation of where the discontinuities should lie. The characteristics of this new boundary are explored and its relationship to the poleward auroral boundary is investigated. Discussion of the results presented in this thesis requires an understanding of the basic principles that govern solar terrestrial physics. An introduction to relevant space plasma physics material is thus provided in this chapter. A background of ionospheric convection is presented in chapter 2, before

an overview of the instrumentation used in this thesis in chapter 3. Chapter 4 presents the new boundary technique which is then applied to a large archive of ionospheric convection data that is analysed in detail in chapters 5 and 6. Finally, chapter 7 presents some preliminary results of ideas for further work.

1.1 Plasma Criterion

Solids, liquids and gases make up the majority of matter that are found on Earth and can be referred to as the primary states of matter. In the bigger picture a fourth state, plasma actually makes up most of the universe. Defining a plasma and understanding some of its basic properties is fundamental to the study of the solar-terrestrial environment. A plasma is created when enough energy is provided to remove at least the outer electron from the atom to create a roughly equal electron and ion mix. The energy can be provided by subjection to medium or high electric fields or bombardment of energetic radiation or particles. To qualify as a plasma the gas containing the charged particles must also exhibit collective behaviour and be quasi-neutral.

The coulomb force acts to establish electric neutrality, since like charges repel and opposites attract. Random perturbations are possible which agitate the particle mix and create local areas of non-neutrality. This is exacerbated in hotter plasmas which cause larger perturbations. To estimate the size of the non-neutral region an electrically dissociated region of size L is considered. Its total electric charge is approximately:

$$Q \sim ne \times L^3 \tag{1.1}$$

where n is the particle density, e is the electronic charge. The electric potential ϕ at the boundary of the region is on the order of:

$$\phi \sim \frac{Q}{(\epsilon_0 L)} \sim \frac{neL^2}{\epsilon_0} \tag{1.2}$$

For a pertubation to produce such a region the energy of each particle ($\sim k_B T$) has to equal the potential energy per particle $e\phi$. Thus the maximum allowed size of the non-neutral region (the Debye Length, L_D) is as follows:

$$L_D = \sqrt{\frac{\epsilon_0 k_B T}{ne^2}} \tag{1.3}$$

When a charge enters a plasma at equilibrium, opposite charges are attracted towards it and like charges repelled away leaving a region of size L_D containing a concentrated zone of particles. The overall effect of this is to create a charge distribution that shields the electrostatic field of the original charge. The electrostatic potential as a function of distance r of a charge q (Debye potential) is:

$$\Phi(r) = \frac{q}{4\pi\epsilon_0 r} \exp^{-(\frac{r}{L_D})} \tag{1.4}$$

For the plasma to be quasi-neutral the physical dimension of the system must be much greater than the Debye Length (L_D). This is the first plasma criterion. The charge shielding effect is the result of collective charges in a sphere (the Debye Sphere). As such a sufficient number of particles must be present. The number of particles (N_D) in the

Debye sphere (plasma parameter) is:

$$N_D = \frac{4\pi}{3} n_e \lambda_D^3 \tag{1.5}$$

where n_e is the number density of electrons. This is referred to as the second plasma criterion. A third criterion relates to the frequency of short-range collisions between particles. Some plasmas such as the Earth's ionosphere, are not completely ionised and contain a significant neutral population. Too many collisions between the electrons and neutrals would result in the medium becoming unplasma-like. To avoid this, the average time between electon-neutral collisions needs to be much larger than the inverse of the plasma frequency (typical oscillation frequency in a fully ionised plasma).

$$\omega_{pe} \tau n >> 1 \tag{1.6}$$

where ω_{pe} is the plasma frequency and τn average time between electron-neutral collisions. If equation 1.6 is on the order of the ion collisional frequency then the electrons can be considered as free but the ions are coupled to the neutrals. In the high-latitude ionosphere at approximately 100 km, large scale electric fields imposed from the magnetosphere drive currents that arise from the inhibited motion of the ion population.

1.2 Particle motion in electric and magnetic fields

One approach to understanding the behaviour of plasmas is to consider the individual motions of the charged particles. This approach is known as single particle motion. In the simplistic case of a uniform magnetic field, $\vec{B}$, a charged particle of mass, m, and

charge, q, will alter its trajectory to a circular orbit at velocity $\vec{v}_\perp$about some guiding centre. Figure 1.1 a) shows this schematically. The ions and electrons orbit with a frequency ω_g and radius r_g that is dependent on their mass and velocity as defined below:

$$\omega_g = \frac{qB}{m} \tag{1.7}$$

$$r_g = \frac{mv_\perp}{|q|\,B} \tag{1.8}$$

This shows that if an ion and electron have the same velocity then the ion gyro-radius would be much larger than that of the electron. If the charged particles have a component of the velocity parallel to a magnetic field line then the actual trajectory of the particle becomes helical. Plasmas in space are rarely this simplified case and the presence of additional electric fields is common. If an electric field is added in the direction perpendicular to the magnetic field then as the charged particle begins to gyrate around the magnetic field the electric field will cause the particle to accelerate for half of its orbit and decelerate the remaining half. Figure 1.1 b) shows this schematically for the case where the charged particle has no initial velocity. The ions and electrons thus travel in a distorted circle with a net displacement in the direction perpendicular to $\vec{E}$. This motion is independent of charge and the velocity of the drift motion is given by:

$$\vec{v_E} = \frac{\vec{E} \times \vec{B}}{B^2} \tag{1.9}$$

This $\vec{E} \times \vec{B}$ velocity, also referred to as the convection velocity.

Another type of motion that is important in the context of space plasmas is the motion of charged particles in a converging magnetic field. This situation is sketched in figure

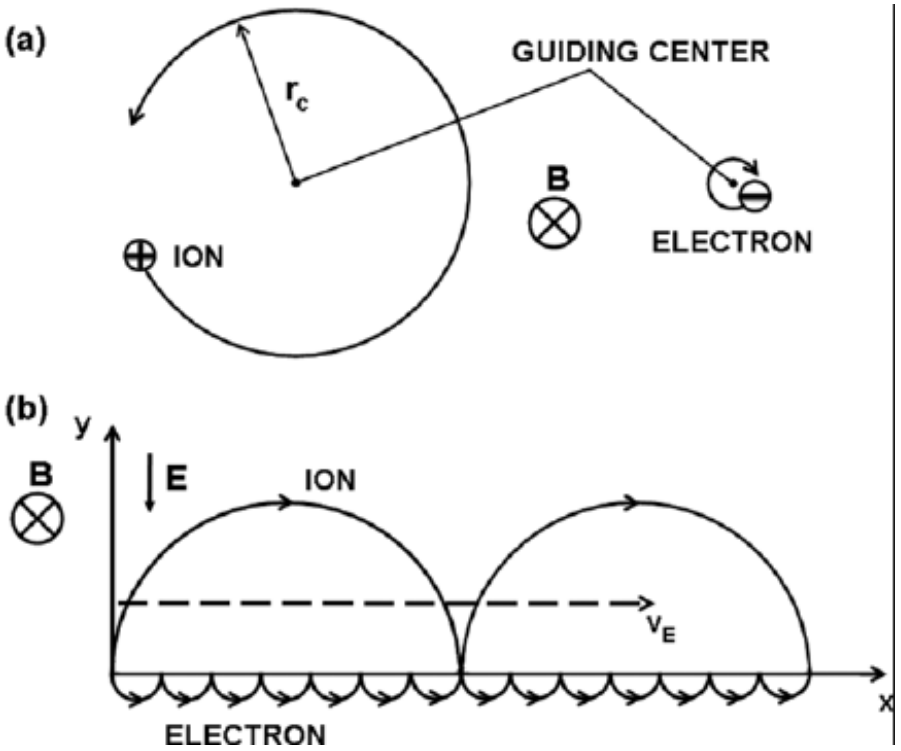

FIGURE 1.1: A sketch of the types of motion of charged particles in a) a constant uniform magnetic field and b) a constant uniform magnetic field with the addition of a perpendicular electric field.

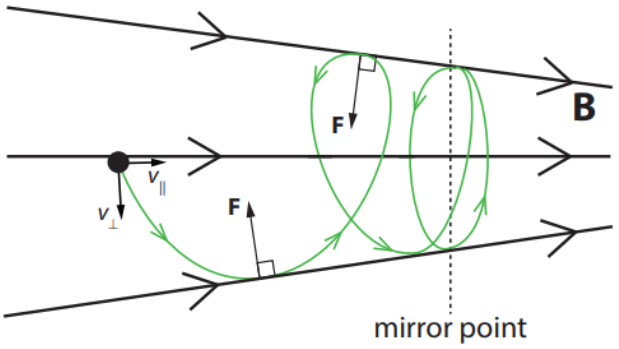

FIGURE 1.2: A sketch showing the motion of a charged particle in a converging magnetic field.

1.2. In this situation we need to consider the concept of adiabatic invariants. These refer to relationships that hold under the condition that the fields vary on time-scales much larger than the typical periodicities of particle motions. The first adiabatic invariant relates to the motion of a charged particle on magnetic field lines and states that in this case the magnetic moment of the particle is conserved i.e:

$$\frac{v_{\perp}^2}{B} = const \tag{1.10}$$

This implies that as the charged particle moves along a field line into a region of higher magnetic field, such as the one sketched in 1.2, $v_{\perp}$ must increase to conserve the first adiabatic invariant. Under the assumption that there are no parallel electric fields such that the particle's energy is constant, as the $v_{\perp}$ contribution to the particle's velocity increases, the contribution from the parallel velocity $v_{\parallel}$ must decrease. In fact at some point the parallel velocity can become zero causing the particle to reverse and *mirror* back in the opposite direction. The location of where this happens is also known as the mirror point. This type of motion is common on closed field lines which have their footprints at high latitudes, where the magnetic field gradient is significant to a particle closing in on the high-latitude ionosphere. Figure 1.3 is a sketch summarising the three common types of particulate motion associated with space plasmas. The gyro motion schematic shows the helical motion of a charged particle along a magnetic field line, orbiting with a gyro-frequency and gyro-radius (equations 1.7 & 1.8), with velocity (V_g). The bounce motion schematic demonstrates the scenario where a gyrating charged particle experiences a gradient in the magnetic field as it moves along a field line. This topology is common for closed magnetic field lines with a footprint at high latitudes and leads to magnetic mirroring. In the situation where a particles mirror point is at a high

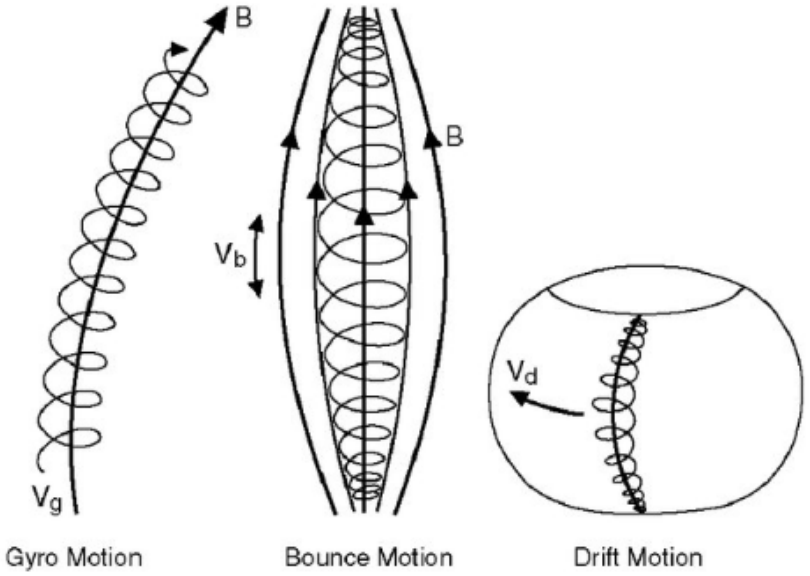

FIGURE 1.3: Schematic taken from *Kivelson and Russell* (1995) showing three types of particle motion in a magnetic field.

enough altitude such that it is not lost through collisions in the upper atmosphere, the particle will bounce back and forth between its two mirror points. Finally, the third schematic refers to a third type of motion that has not previously been introduced, the drift motion. This *curvature* drift refers to the motion of charged particles around the Earth due to curvature of the magnetic field lines. This situation causes the particles to experience a centrifugal force directed away from the centre of field line curvature. As the particles move away from the curvature of the field its gyro-radius increases and ultimately leads to a drift in the direction perpendicular to the magnetic field and radius of curvature.

1.3 Magnetohydrodynamics

Section 1.2 discussed the motion of individual particles in the presence of electric and magnetic fields. An alternative approach is to treat the plasma as a single hydrodynamic fluid acted on by electric and magnetic forces. This is known as the magnetohydrodynamic (MHD) model.

1.3.1 MHD Equations

The section will introduce relevant equations that connect the plasma mass density, velocity, thermodynamic pressure and the magnetic field in single-fluid MHD. A full description can be found in chapter 8 of *Goldston and Rutherford* (1995). The following equations are stated assuming a hydrogen plasma consisting of electrons and ions with charge $\pm e$ and the following properties:

$$n_i \approx n_e \approx n \tag{1.11}$$

$$\rho = n_i M + n_e m \approx n(M + m) \approx nM \tag{1.12}$$

$$\vec{V} = \frac{n_i M \vec{V_i} + n_e m \vec{V_e}}{\rho} \approx \vec{V_i} \tag{1.13}$$

where n_i and n_e are the number of ions and electrons respectively, ρ is the mass density and $\vec{V}$ the velocity density. The ion mass is treated as much larger than the mass of the electrons and as such the mass velocity of the plasma can be approximated to the ion velocity.

The first equation is the mass continuity equation which describes the conservation of mass in a classic, non-relativistic plasma, namely that plasma cannot be created or destroyed:

$$\frac{\delta\rho}{\delta t} + \vec{\nabla} \cdot (\rho\vec{V}) = 0 \tag{1.14}$$

The second equation utilises the single-fluid electron and ion momentum balance equations and combines them to give the 'single-fluid equation of motion':

$$\rho\frac{d\vec{V}}{dt} = \sigma\vec{E} + \vec{j} \times \vec{B} - \vec{\nabla}p \tag{1.15}$$

where $p = p_e + p_i$ is the total pressure, σ is the charge density and $\vec{j}$ is the current density.

The third equation is the generalised Ohms law which is given by:

$$\vec{E} + \vec{V} \times \vec{B} = \eta\vec{j} + \frac{\vec{j} \times \vec{B} - \vec{\nabla}p_e}{ne} \tag{1.16}$$

where η is the resistivity. This equation is valid assuming that the collisional transfer of ions to electrons ($\vec{R_{ei}}$) is equal to $\eta ne\vec{j}$ and that the electron inertia can be neglected. This assumes the case where phemonema occur slowly enough that the electrons can reach dynamical equilibrium with respect to their motion along the magnetic field.

To complete this section, Maxwells equations are presented. These four laws describe how electric and magnetic fields can be generated by charges, currents and changing fields.

$$\vec{\nabla} \times \vec{B} = \mu_0 \vec{j} + \mu_0 \epsilon_0 \frac{\delta \vec{E}}{\delta t} \tag{1.17}$$

$$\vec{\nabla} \times \vec{E} = -\frac{\delta \vec{B}}{\delta t} \tag{1.18}$$

$$\vec{\nabla} \cdot \vec{B} = 0 \tag{1.19}$$

$$\vec{\nabla} \cdot \vec{E} = \frac{\rho}{\epsilon_0} \tag{1.20}$$

The equations presented in this section describe a plasma that is treated as an electrically conducting field. In certain situations these equations can be simplified further and the next few sections outline approximations that are often used, especially when talking about space plasmas.

1.3.2 Quasi-neutrality

The principle of quasi-neutrality and some of the basic properties of plasmas has been introduced in section 1.1. It is common to assume that quasi-neutrality holds when using the MHD equations. Under this assumption the electric force ($\sigma \vec{E}$) and displacement current may be omitted and the single-fluid equation of motion and the Ampere-Maxwell law can be written as:

$$\rho\frac{d\vec{V}}{dt} = \vec{j} \times \vec{B} - \vec{\nabla}p \tag{1.21}$$

$$\vec{\nabla} \times \vec{B} = \mu_0\vec{j} \tag{1.22}$$

1.3.3 Small ion gyroradius

The right hand side of the generalised Ohms law equations (Equation 1.15) contains three terms, the resistive term ($\eta\vec{j}$), the hall term ($\frac{\vec{j}\times\vec{B}}{ne}$) and the electron anisotropy term ($\frac{\vec{\nabla}p_e}{ne}$). In the case that the ion gyroradius is very small compared to the length of fluid motion then Ohms law can be simplified to:

$$\vec{E} + \vec{V} \times \vec{B} = \eta\vec{j} \tag{1.23}$$

1.3.4 Infinite conductivity (Ideal MHD)

High temperature plasmas (such as space plasmas) have negligible resistivity and so can be described in the limit of infinite conductivity also known as ideal MHD. Another important MHD equation, the induction equation, relates the velocity and magnetic field of an electrically conducting plasma. The induction equation is derived by taking the curl of the simplified Ohms law, utilising Faradays law (equations 1.23 and 1.18) and one of the vector identities to give:

$$\frac{\delta\vec{B}}{\delta t} = \vec{\nabla} \times (\vec{V} \times \vec{B}) - \vec{\nabla}^2\vec{B} \tag{1.24}$$

The first term of the equation describes the convection of the plasma with magnetic field. This is a feature of space plasmas that is of fundamental importance to understanding the behaviour of the solar wind, magnetosphere, ionosphere systems. The second term is the diffusive term and describes the diffusion of the magnetic field across the plasma. For an ideal MHD, i.e. infinite conductivity the diffusive term becomes negligible and the first term *frozen-in flow* (*Alfvén*, 1942) dominates. This is interpreted as: if the field changes then the magnetic field lines will also move. There are certain times when this condition no longer holds and the diffusive term of the induction equation dominates which ultimately allows coupling of the solar wind into the terrestrial system via a process called *Magnetic Reconnection*. The next section will discuss this in more detail.

1.4 Magnetic Reconnection

The process of magnetic reconnection can be thought of as magnetic field lines being cut and forming a new geometry with other field lines. This is particularly relevant at boundary locations between two oppositely directed magnetic field lines that are separated by a thin current sheet. Such locations exist throughout the magnetosphere and are vital for energy and momentum exchange between the solar and terrestrial environments. Figure 1.4 shows a sketch of the reconnection configuration. The process is driven by plasma inflow shown by U_i in the figure. The grey shaded region represents the diffusion region, where the frozen in condition breaks down and the diffusive term in the induction equation dominates. In this 'x-type' configuration the field is zero at the centre of the X and is also deemed the *neutral point*. Here, magnetic field lines diffuse across the plasma leading to an x-type configuration as field lines connect through the

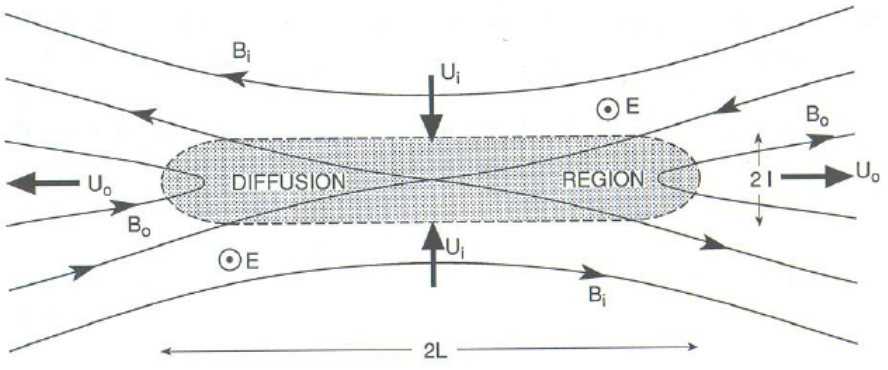

FIGURE 1.4: A schematic to show the effects of reconnection between two oppositely directed field lines (solid black arrowed lines). The grey area shows the diffusion region and 'x-line' geometry and the thick direction arrows represent the direction of plasma flow before and after the reconnection process. (*Kivelson and Russell*, 1995)

current sheet and joining the separate plasma regimes. The newly reconnected field lines experience high magnetic tension as they are severely kinked which leads to an outflow of plasma from the diffusion region, shown as U_o in the figure. For continuous reconnection plasma must continuously flow into the diffusion region. This process allows the exchange of plasmas from two separate regimes and for them to mix over a large portion of the field line.

1.5 The solar wind

The solar wind originates from the solar corona and extends throughout the heliosphere as a continuously blowing high-speed particle stream. Close to the Earth's orbit the solar wind is usually between 300-1400 km/s with 500 km/s as the most likely value (*Meyer-Vernet*, 2007). At 500 km/s the solar wind takes approximately 4 days to reach the Earth. At over 600 km/s velocity the solar wind is deemed high speed solar wind. The beginning of the solar atmosphere, the Chromosphere, has temperatures on the

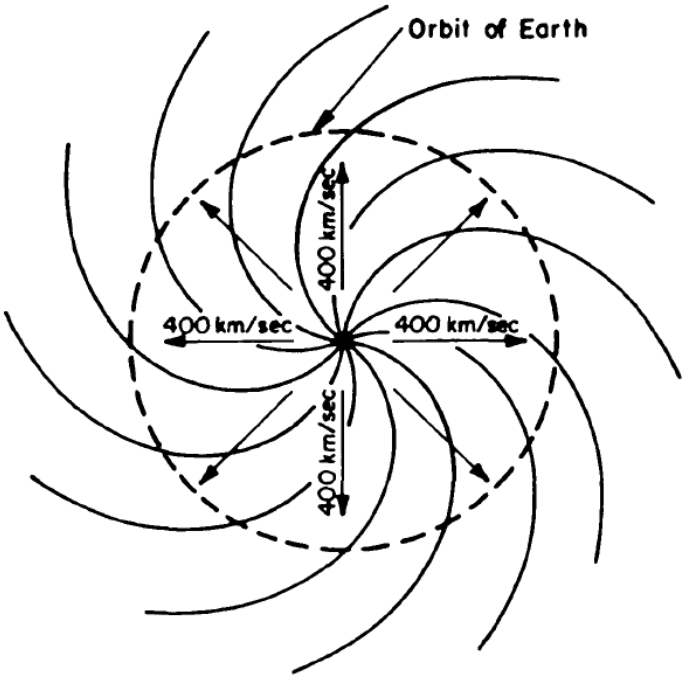

FIGURE 1.5: Spiral IMF field lines frozen in to a radial solar wind expansion at $400km/s^{-1}$ (*Kivelson and Russell*, 1995)

order of 6000K. For the solar wind to exist particles must be accelerated in the Corona and in fact most of the dynamics of the solar wind are created in this region. The solar magnetic field broadly speaking contains two different regions, one where the field is closed and the ionised solar atmosphere is trapped. Where the field extends far into the interplanetary medium in a stretched configuration they are considered as open. These open field lines are also called 'coronal holes' and normally located at high latitudes, although at solar maximum they can extend farther towards the equatorial plane and these are the source of the solar wind outflow. As the solar wind propagates radially at constant velocity into the interplanetary medium, the rotation of the sun and frozen-in flow condition cause the interplanetary magnetic field (IMF) to bend into a spiral shape. This is shown schematically in Figure 1.5.

Thus, the IMF at Earth, whilst displaying a variety of orientations, typically contains a component in the sunward/antisunward directions, and a component in (or opposite to) the direction of Earth's orbit. This has implications for the solar wind - magnetosphere coupling as described below.

1.6 The Magnetosphere

The solar wind expands at supersonic speed into the interplanetary medium and when it eventually reaches Earth's magnetic field a shock wave (*Bow Shock*) is formed upstream. At the bow shock the solar wind is slowed and heated creating a region of plasma called the *Magnetosheath*. The plasma in this region is hotter and denser than the solar wind plasma. This leads to highly variable solar wind magnetic field and plasma parameters. To a first approximation the magnetosheath plasma and the terrestrial magnetic field are unable to interact as a consequence of the frozen-in condition. Figure 1.6 shows a schematic of the magnetosphere with major features and plasma populations labelled. The magnetopause is the boundary that separates the two different plasma regimes and the formation of this layer is discussed in more detail below. The location of this boundary can be determined by the balance of pressure between the magnetosphere and magnetosheath. The dominant pressure in the magnetosphere is the magnetic pressure compared to the combination of thermal and dynamic pressures in the magnetosheath. As the dayside portion of the magnetosphere becomes compressed due to the incoming solar wind the nightside magnetic field region is stretched out into an elongated tail for hundreds of Earth radii.

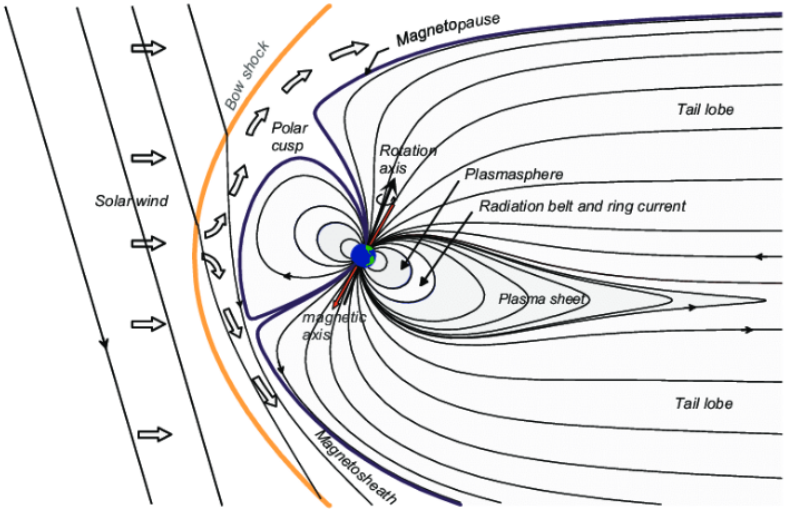

FIGURE 1.6: Cross section of the magnetosphere. The arrowed outlines show the direction of the incoming IMF and subsequent flow around the magnetopause. The solid black lines represent the magnetic field, the yellow line the bow shock and the blue outline the magnetopause. Several plasma populations are also labelled inside the magnetosphere, adapted from NASA's Cosmos.

The main sources of the plasma that populate the magnetosphere are the solar wind and Earth's ionosphere contributing the electrons and protons. In fact the plasma inside the magnetosphere is not evenly distributed but grouped according to those aforementioned regions each with its own distinct characteristics. Looking at Figure 1.6 there are four separate plasma regions labelled on the nightside of the magnetosphere (Tail Lobe, Plasmasheet, Ring Current and Plasmasphere). The plasma sheet can additionally be separated into the central plasma sheet and the plasma sheet boundary layer (PSBL). Of particular relevance to this thesis are the plasma sheet and PSBL, these two regions contain the majority of the magnetospheric plasma with associated field lines that reach into the auroral ionosphere.

In a 'closed' magnetosphere, the solar wind plasma and the terrestrial field are unable to

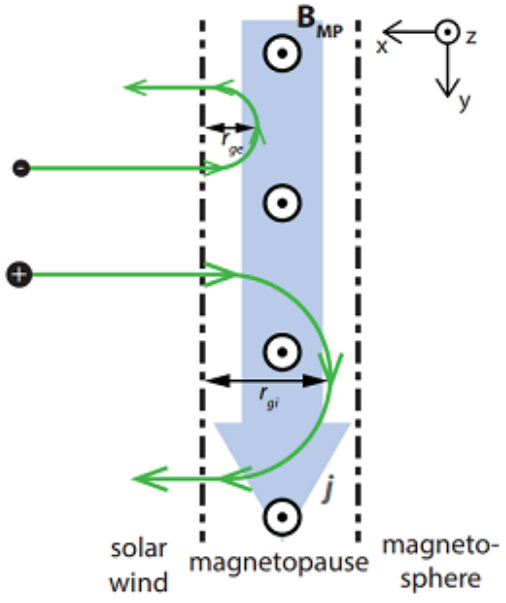

FIGURE 1.7: A simple representation of a magnetopause boundary separating an unmagnetized solar wind (left) from a magnetosphere containing no plasma (right). Adapted from *Kivelson and Russell* (1995)

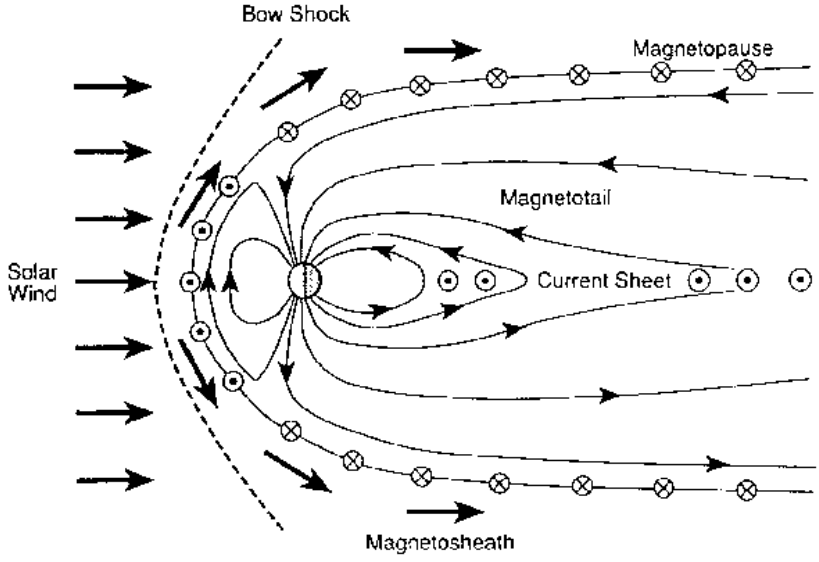

FIGURE 1.8: Cross section of the magnetosphere taken from *Kivelson and Russell* (1995). The solid arrowed lines show the magnetic field lines and direction. The current directions in the magnetopause and tail are shown. Currents directed into the plane of the diagram are circled crosses and out of the plane are circled dots.

interact due to the frozen-in approximation and the magnetopause represents the interface between the two regimes. This boundary is also often called the Chapman Ferraro current layer after *Chapman and Ferraro*, (1931) conceived the idea of a magnetospheric cavity based on the theory of the frozen-in approximation. As an unmagnetized electron and proton begin to penetrate the magnetic field, they become subjected to the Lorentz force and begin to gyrate. Figure 1.7 shows this process schematically. The electrons and protons exit after half an orbit with the electron moving much less distance due to the much smaller mass and gyroradius. The motion of the electrons and ions is in opposite directions giving rise to a current sheet across the magnetopause. A similar such current sheet is found in the magnetotail between the northern and southern tail lobes. Figure 1.8 shows the magnetopause and tail currents and their directionality.
A key assumption of Chapman and Ferraro's idea of the 'closed' magnetosphere was that the entire system obeyed the frozen-in approximation. In actuality there are key regions where this assumption breaks down, for example in areas of high current densities i.e. the magnetopause and magnetotail. *Dungey* (1961) used the idea that sheared magnetic field lines could separate the current sheet to come up with the idea of the 'open' magnetosphere in which energy and momentum from the solar wind can be input into the terrestrial system.

Figure 1.9 shows the cyclic process *Dungey Cycle* of the 'open' magnetosphere schematically. When the IMF has a southward directed component magnetic reconnection can happen at the magnetopause. At line 1 a closed magnetic field line with both of its footprints connected to the Earth undergoes magnetic reconnection and merges with a southward directed IMF field line. After the merging there are now two 'open' field lines

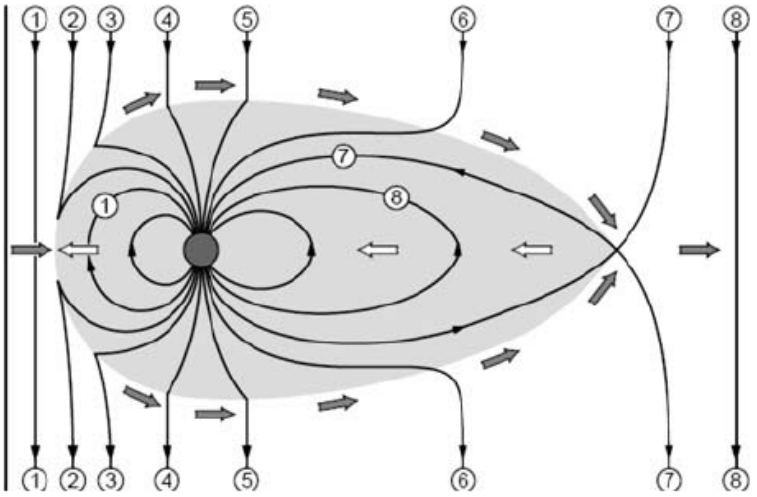

FIGURE 1.9: Cross section of the 'open' magnetosphere adapted from *Baumjohann and Treumann* (1996). The solid black lines represent the magnetic field, the shaded grey region the 'closed' magnetospheric region and the numbers show the succession of field line configurations after reconnection at the magnetopause takes place.

(2) so-called as they have one footprint connected to Earth and the other extending into the solar wind. As seen in the schematic, at this point these newly connected field lines are subjected to high magnetic tension such that the magnetospheric part (shaded region) will move towards the nightside. Field lines 3 to 6 move with the solar wind down-tail until open field lines from each pole meet (7). At this point the two oppositely directed field lines come close enough to initiate magnetic reconnection to create once again a closed terrestrial magnetic field line and a solar wind IMF field line (8). Just after the tailward reconnection the closed earth field line is subject to high magnetic tension, this causes the field line to relax and move Earthward taking with it plasma that is frozen-in to the field line. These field lines will gradually convect to the day-side magnetosphere to replace those removed. This general convective circulation will maintain the magnetosphere; without the replacement of dayside flux the magnetosphere

would eventually be completely eroded. In reality the IMF is rarely due southward and the geometry of the location of magnetic reconnection on the magnetopause is also dependant on the level of east/west component to the IMF. If this is strong asymmetries can be introduced into the magnetosphere between the northern and southern poles. A more detailed discussion of this will occur in Chapter 2.

1.7 The Ionosphere

The ionosphere constitutes the Earth's upper atmosphere and is so-called due to the partial ionisation of the neutral atmosphere caused predominantly by solar ultra-violet light. The level of ionisation is a function of geographical latitude and local time. Above approximately 80km in altitude ion-neutral collisions occur too infrequently to rapidly recombine which enables a permanent ionised population.

The ionosphere roughly consists of three regions of varying thickness and electon/ion densities. The lowest region, the D-region is below altitudes of about 90 km and is dominated by electron-neutral collision frequencies. As such it is only weakly ionised and cannot be considered a plasma as defined in Section 1.1. Above 90km can be referred to as the upper atmosphere and can be split further into two distinct 'E' and 'F' regions. The E region is the middle layer of the ionosphere and extends from 90km altitude to $\sim$ 150km, the F region is the top layer of the ionosphere and extends from 150km to $\sim$ 1000km. Figure 1.10 highlights the two regions and their peak plasma densities. The E region peaks at about 110 km and the F region at about 300 km. In the day the F region splits into two separate regions, the 'F1' (200km) and 'F2' (300km). During the

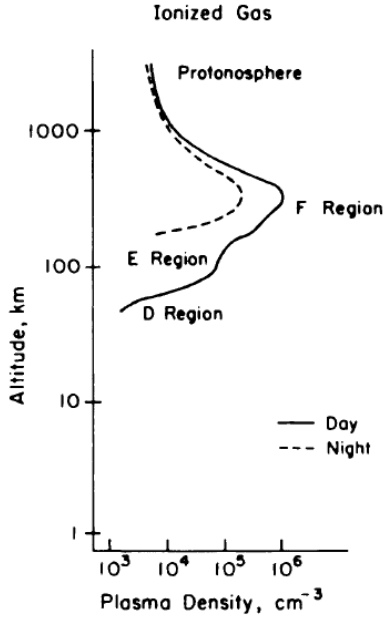

FIGURE 1.10: The typical day/night ionospheric plasma density (from Kelly, 1989)

daytime the gap between the E and F region becomes less distinct as the enhanced UV creates additional ionisation.

Both the ions and electrons have mobility of varying amounts in the E and F regions which gives rise to currents. Since the electron gyrofrequency is much larger than its collisional frequency the electrons drift at the $\vec{E}X\vec{B}$ velocity throughout both the E and F region. The larger size of the ions causes them to interact more readily with the neutral population. At the bottom of the E region their collision frequency is high with respect to the ion gyrofrequency. As such the ions are effectively stationary with respect to the neutral atmosphere. This leads to a current in the $-\vec{E}X\vec{B}$ direction that is perpendicular to both the magnetic and electric fields, this is known as the *Hall Current*. As we increase in altitude from 90 km the neutral density drops off and with it the ion

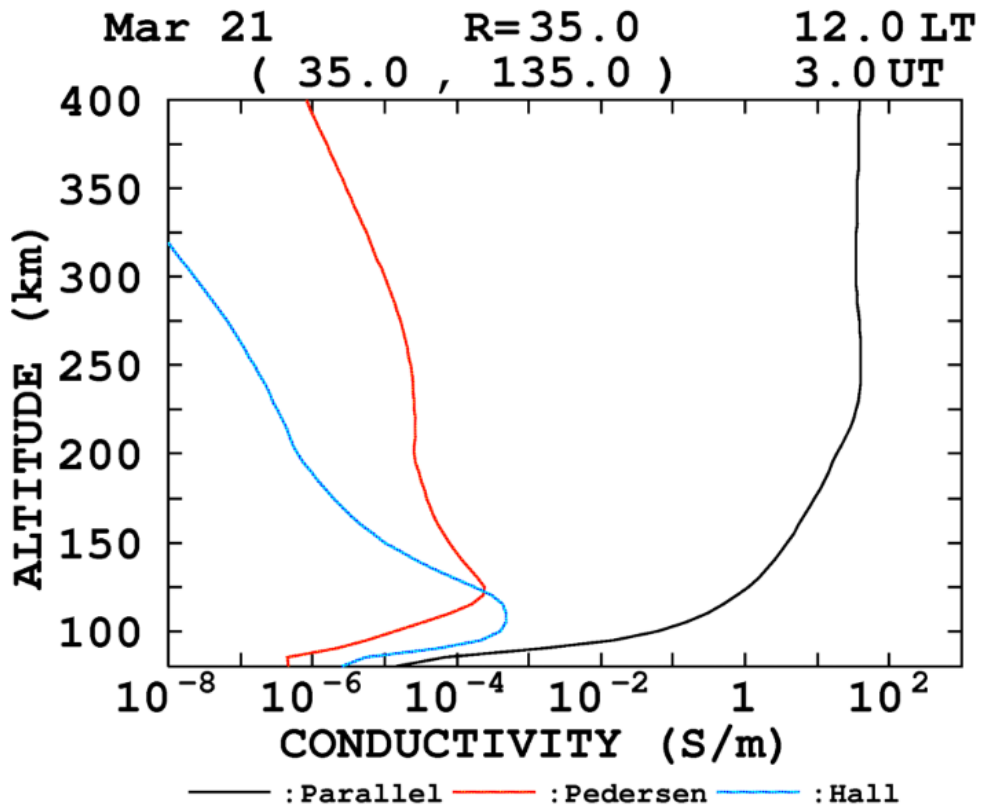

FIGURE 1.11: An example of the daytime height profile of the parallel, Pedersen and Hall conductivities, respectively. The conductivity depends on various parameters such as location, time, season and solar activity. Image credit: WDC for Geomagnetism KYOTO

collision frequency to allow the ions to move more freely in the direction of the electric field. This gives rise to a current that is parallel to the electric field and perpendicular to the magnetic field, this is known as the *Pederson Current*.

Figure 1.11 shows the Hall (Blue) and Pederson (Red) conductivities as a function of altitude. The Hall conductivity peaks at approximately 110km, with the Pederson conductivity a little higher (125 km). At 125km the magnitudes of the Hall and Pederson conductivities are similar, this is because the ions have as much mobility in the parallel and perpendicular directions. Above 125 km the Pederson conductivity dominates as the ions are able to move more freely. The E region is the source of the currents that enable

coupling between the atmosphere and the magnetosphere. At F region altitudes the collisional frequency for the ions is so low that the ions drift in the $\vec{E} \times \vec{B}$ direction with the electrons to obey the frozen in approximation. The magnitude of the $\vec{E} \times \vec{B}$ velocity is determined by magnetospheric convection introduced previously, the next section will discuss the associated ionospheric convective flows further.

At the high latitudes an important consideration about the conductances is that the horizontal electric field becomes essentially independent of height. Therefore here, the height integrated Hall Σ_H and Pederson Σ_P current conductivities are of particular relevance. These conductances and the height-integrated horizontal current density are related via the height-integrated Ohms law to give:

$$\vec{J_\perp} = \Sigma_P \vec{E_\perp} - \frac{\Sigma_H (\vec{E_\perp} \times \vec{B})}{B} \tag{1.25}$$

This is important as the magnetosphere is physically linked to the ionosphere through large-scale current systems that flow down magnetic field lines and close in the ionosphere, this is discussed in more detail below.

1.8 Magnetosphere-Ionosphere Coupling

Magnetospheric convection has been introduced in section 1.5. This process is also imposed on the high-latitude ionosphere due to large-scale current systems connecting these two regions. This is due to the convection electric field $\vec{E_c}$. In the frame of reference of the field lines moving at velocity $\vec{v_c}$ the infinite conductivity of the field lines means the

electric field reduces to zero. For a stationary observer in the Earth's frame of reference an electric field is measured as a result of the Lorentz transformation.

$$\vec{E_c} = -\vec{v_c} \times \vec{B} \tag{1.26}$$

where $\vec{v_c}$ is the convection velocity and $\vec{B}$ is the magnetic field. The strength of the convection field is related to the efficiency of the rate of magnetic reconnection at the dayside magnetopause. Since electric fields can be described as the gradient of the electrostatic potential an alternative way of describing this is via a potential difference that is applied across the magnetosphere. Typical values of the dawn/dusk electric field are 0.2-0.5 mV/m or 50-100 kV potential difference across the magnetopause. This transpolar voltage is thus often used as quantitive way of measuring the strength of the convection pattern.

As the open field lines convect towards the tail and back round to the dayside their counterpart ionospheric footprint and plasma also moves. Figure 1.12 a) shows the motion of the field lines over time according to the numbered boxes. 1 and 6 represent the point of reconnection opening and closing magnetic flux. Points 2-6 show the motion of the plasma over the polar cap with the open field lines. Between point 8 and 9 is the earthward return of the closed field lines to replenish the flux lost due to dayside reconnection. This part of the figure also highlights the different associated plasma regimes as the latitude decreases from the polar cap. It is clear from the figure that this process results in a two cell convection pattern of the ionospheric flow (the solid black arrowed lines showing example streamlines). The boundary between anti-sunward

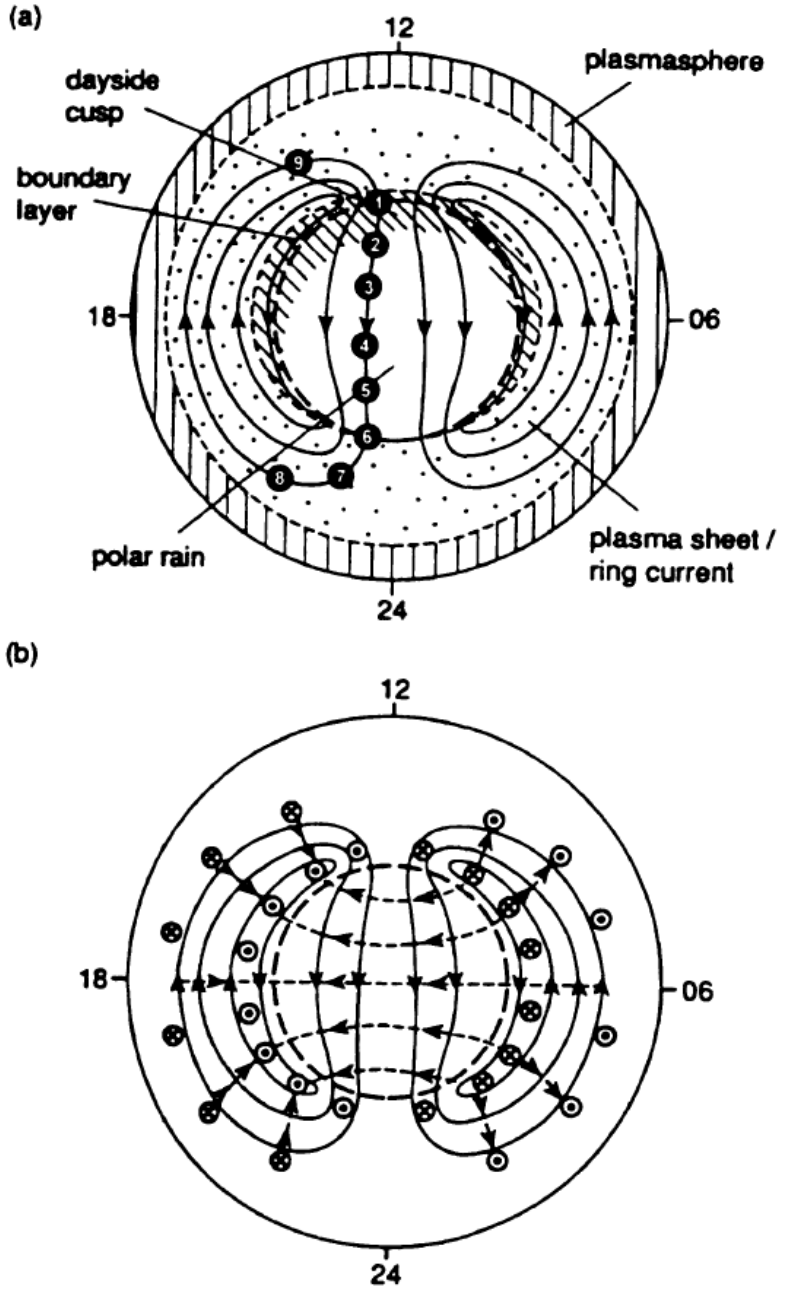

FIGURE 1.12: A sketch looking down on the northern hemisphere high latitude ionosphere. a) shows the convection streamlines of the $\vec{E} \times \vec{B}$ velocity numbered to highlight the time evolution. This also labels the associated magnetospheric plasma precipitation zones. b) shows the main large -scale current systems. Pederson currents are shown as the short dashed arrowed lines and the FAC's as the dot and cross circles directed in and out of the plane of the figure. (after *Cowley* (1993))

motion over the polar cap and the lower latitude sunward return flow separates the open and closed field line regions. This boundary between the two is often referred to as the open-closed field line boundary (OCB). This boundary is of significant importance to this thesis and will be discussed further in Chapter 2.

It can be deduced that the convection streamlines can also equivalently be thought of as equipotential contours with a resulting electric field from dawn to dusk in the open portion of the northern hemisphere by considering the following equations:

$$\vec{v_E} = \frac{\vec{E} \times \vec{B}}{B^2} \tag{1.27}$$

$$\vec{E} = -\nabla\phi \tag{1.28}$$

In the closed field line portion the electric field is directed towards the pole at dusk local times and directed southwards at dawn. Field Aligned Currents (FACs) also known as Birkeland currents are driven by convection and flow along the magnetic field lines connecting the magnetosphere to the ionosphere. Figure 1.12 b) shows the large-scale ionospheric currents that flow in the ionosphere. At the poleward edge of the open field line region (the long circular dashed line) current flows into the ionosphere at dawn local times (circle with cross) and out of the ionosphere in the dusk sector (circle with inside dot). This is the Region-1 current system which extends up to the magnetopause. At the equatorward edge of the auroral oval (and equivalently the lowest latitude sunward convection regions) the region-2 FAC system occurs. Figure 1.12 b) shows the current flowing into the ionosphere in the dusk cell, and out of the ionosphere in the dawn

cell. This region-2 current system closes in the westward ring current in the near-earth equatorial plane. The Pederson currents (as mentioned in section 1.6) flow parallel to the electric field and are shown as the short dashed lines. The Pederson current flows from dawn to dusk over the open ionospheric region and from the region 1 to region 2 FACs. The Hall current flows perpendicular to the electric and magnetic field in the direction opposing the $\vec{E} \times \vec{B}$ velocity (which is shown in the figure as the solid arrowed lines).

It was mentioned in section 1.5 that the orientation of the IMF will affect the magnetopause reconnection location and introduce dawn-dusk asymmetries. If the condition for magnetic reconnection to occur is oppositely directed field lines (section 1.3) then the introduction of an east-west component to the IMF will cause the magnetopause reconnection location to tend away from the sub-solar point and introduce a dawn-dusk asymmetry. This asymmetry is also imparted into the ionosphere and can affect the resulting patterns. Figure 1.13a and 1.13b shows a schematic taken from *Cowley et al.* (1991) to highlight the additional FACs generated from a strong IMF B_y component, for $B_y > 0$ and $B_y < 0$ respectively. It shows a similar format to that of figure 1.12 showing the convection streamlines (solid black arrowed lines), downward directed FACs (crossed circles), upward directed FACs (dotted circles) and the OCB (dashed line).

It is immediately obvious that the presence of a strong IMF B_y alters the ionospheric topology. Looking across the noon sector two current sheets are elongated longitudinally than when compared to the 'ideal' picture in figure 1.12. The equatorward current at noon, directed into the ionosphere for $B_y > 0$ and out for $B_y < 0$ is associated with the midday region 1 current. The term region 0 is used to refer to FACs present poleward of

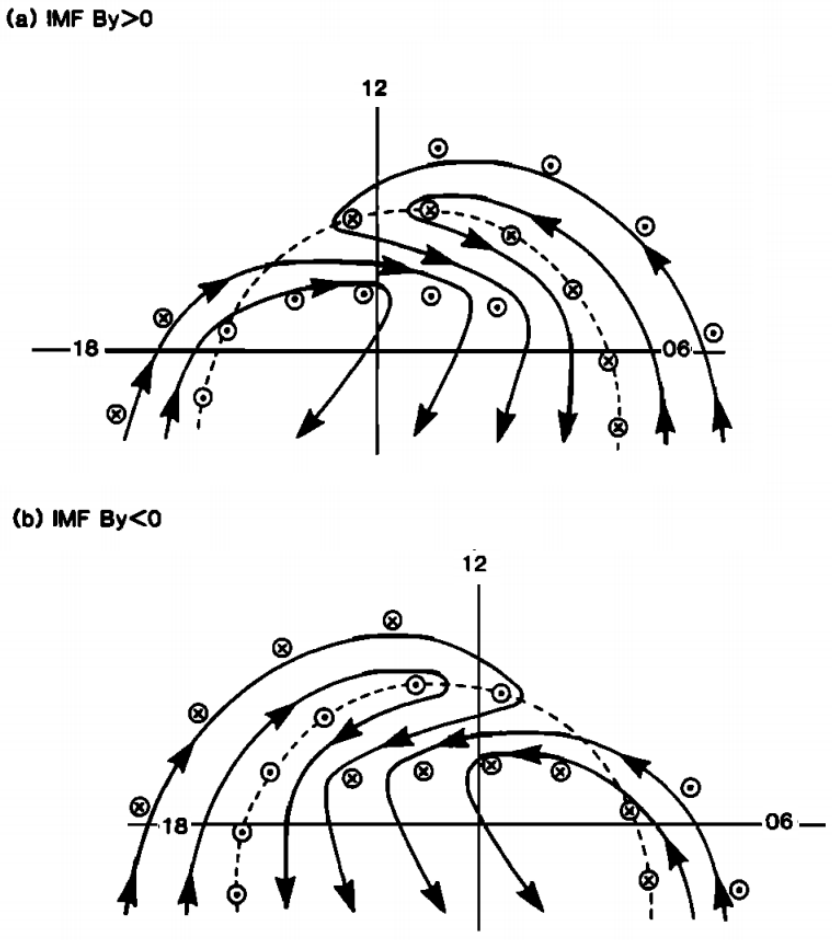

FIGURE 1.13: A sketch taken adapted from *Cowley et al.* (1991) to show how the IMF B_y introduces asymmetries on the dayside convection pattern in the northern hemisphere. The solid arrowed curves represent the flow streamlines, the dashed line represents the open closed field line boundary and the circled dots and crosses represent the upward and downward FAC currents respectively. Noon is orientated to the top of the figure and dusk to the left. a) shows the result for IMF B_y+ and b) for B_y-

region 1 (this does not have to be confined to the noon sector). For $B_y > 0$ ($B_y < 0$) the region 0 current flows out (in) of the ionosphere. The pair of FACs in the noon sector drive the direction of flow westward (eastward) for $B_y > 0$ ($B_y < 0$) before turning across the polar cap. This can also be thought of as newly open field lines reacting to east-west directed stresses resulting from the asymmetric IMF imparting itself on the magnetopause. In addition it can be seen that the OCB is shifted towards dawn for $B_y > 0$ and the centre of flow between the dawn and dusk cells, aligned with the OCB (convection throat) is shifted in local time about noon. For the positive B_y case this location occurs at earlier local times than for $B_y < 0$.

The effect of different IMF orientations on the size and shape of the ionospheric convection will be discussed in more detail in Chapter 2. Another consideration is the time-dependence of the system introduced in this section. So far only the steady-state picture has been described i.e. where the rates of magnetic reconnection are balanced in the dayside and nightside regions. The effects of non-steady reconnection rates are also discussed in the next chapter.

Chapter 2

Dependencies of the Ionospheric convection pattern

Chapter 1 has provided a broad overview to the solar-terrestrial environment and solar wind-magnetosphere-ionosphere coupling. This chapter provides more specific background on the factors that control the ionospheric convection pattern, in particular its morphology and time-dependence. These factors will naturally also influence the magnetospheric boundaries that are being studied by proxy with the Super Dual Auroral Radar Network (SuperDARN) ionospheric convection maps, and thus is of particular relevance to the work described in this thesis.

2.1 IMF dependancies on the ionospheric convection

2.1.1 Reconnection Geometry

There is clear evidence for magnetic reconnection being the dominant process for transporting plasma, energy and momentum into the magnetosphere. For example, *Gosling et al.* (1990) observed enhanced plasma flows along the magnetopause. *Elphic et al.*

(1990) saw a magnetic field component normal to the magnetopause that was indicative of recently reconnected field lines. Magnetosheath plasma has been observed on open field lines by *Fuselier et al.* (1997) and *Phan et al.* (2003) who saw proton emissions in the dayside ionosphere associated with the footprint of a newly reconnected field line.

The simplified case involving completely anti-parallel field lines was presented in chapter 1. The incoming solar wind is, in reality, highly variable and rarely allows for such geometry. In terms of solar-wind-magnetosphere coupling the most relevant orientations of the IMF occur in the north-south (Z_{GSM}) and east-west (Y_{GSM}) directions. The clock angle is commonly used as a measure of the orientation in the Y_{GSM}/Z_{GSM} plane. At 0° the field is in a purely northward direction ($+Z_{GSM}$). Rotating to 90° gives a transverse solar wind ($+Y_{GSM}$). 180° to 270° thus represent the $-Z_{GSM}/-Y_{GSM}$ directions. Of particular relevance to this thesis is resulting convection when the IMF has a clock angle between 90° and 270° i.e. a southward B_z component. Thus the discussion in this chapter will mostly focus on this case.

The brief introduction to the reconnection process in chapter 1 implies the IMF is purely anti-parallel to the Earth's magnetic field ($-Z_{GSM}$). Considering this IMF orientation the resulting reconnection would theoretically take place on a line perpendicular to the Earth's magnetic field along the sub-solar point. If the IMF changes its orientation so the Y_{GSM} component is non-zero then this will affect the location of the reconnection on the magnetopause. There are currently two theories on how exactly the reconnection location alters. The first is anti-parallel reconnection (*Crooker* 1979, *Luhmann et al.,* 1984) which occurs as a result of magnetic shear imposed by the Y_{GSM} component of the IMF. This can be seen in Figure 2.1 a). The reconnection region becomes discontinuous

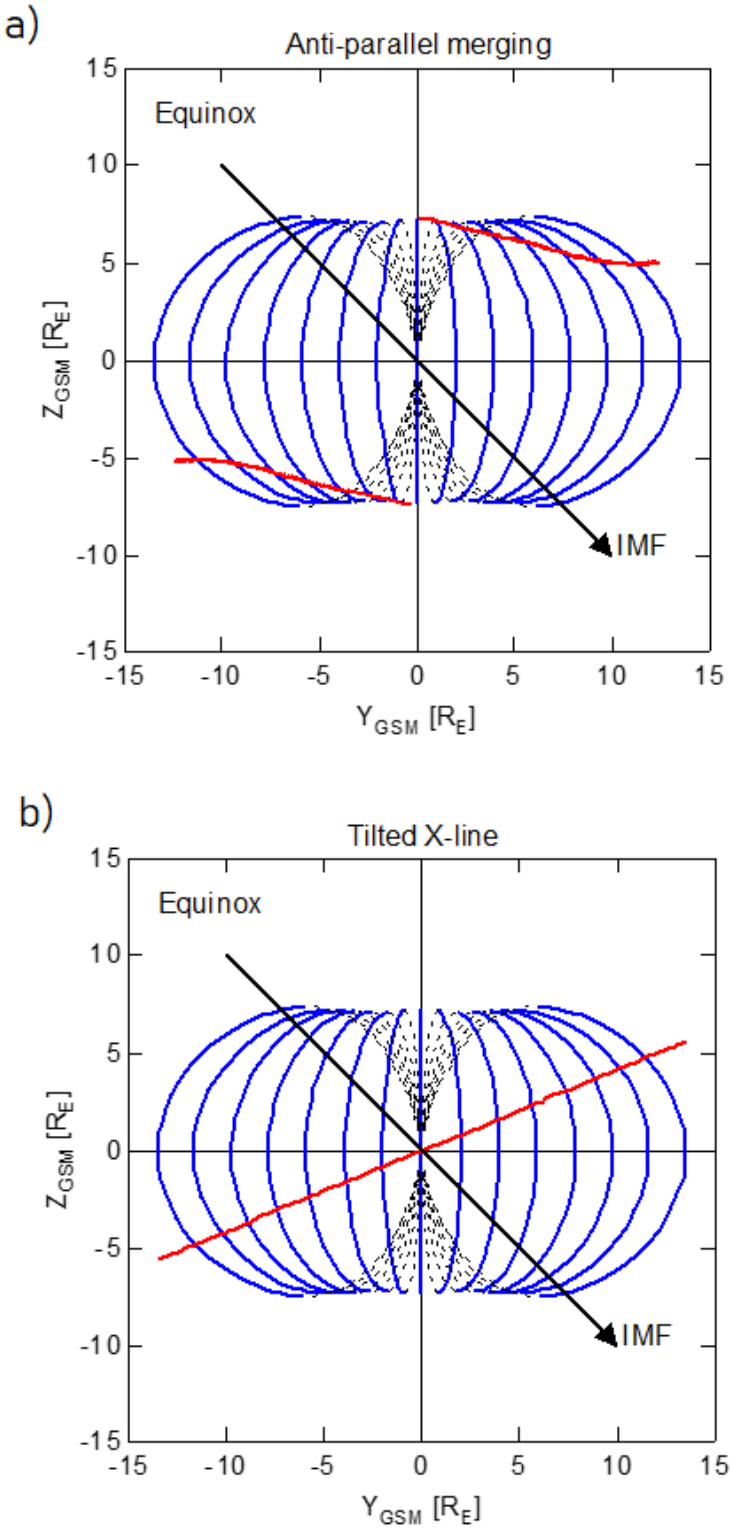

FIGURE 2.1: A sketch to show the difference in reconnection locations (red lines) for a) anti-parallel and b) component reconnection. The view is towards the earth looking at the sub-solar point. Magnetospheric closed field lines are shown as the blue curves. [Adapted from pet (2004)]

and shifts poleward (overlayed red lines). This leads to an offset dusk in the northern hemisphere for $+Y_{GSM}$ and dawn in the southern hemisphere. The second type of reconnection is component reconnection which is sketched in Figure 2.1 b) (*Sonnerup*, 1974, 1984) . Here reconnection occurs along a line which extends in both directions from the sub-solar point. It is likely that both types of reconnection occur. *Hesse et al.* (2004) suggest that the anti-parallel type occurs at a 30% higher rate.

2.1.2 Effect on large-scale convection

Chapter 1 introduced mangetosphere-ionosphere coupling and the magnetospheric convection driven by reconnection that also imposes itself onto the ionosphere. The IMF orientation significantly affects the reconnection geometry inducing asymmetries that can also be imparted into the ionosphere. There are different ways to deduce the average statistical large-scale convection according to IMF orientation. One technique which is relevant to this thesis is ground based radar observations e.g. (*Ruohoniemi and Greenwald*, 1996, 2005; *Pettigrew et al.*, 2010; *Thomas and Shepherd*, 2018). Spacecraft observations of the polar cap electric fields can also be used to derive empirical models of the convection e.g.(*Weimer*, 1999).

Figure 2.2 shows average global convection patterns derived from a network of high latitude high frequency (HF) radars (SuperDARN) with over 6 years of data from 2010-2016. The figure is arranged in a clock angle format and the differences in shape of the convection cells is apparent with the different IMF orientations. With a $+Y_{GSM}$ component the dusk cell is more rounded and the dawn cell a thinner crescent shape (*Reiff and Burch*, 1985). The opposite is true for $-Y_{GSM}$. There are also differences in

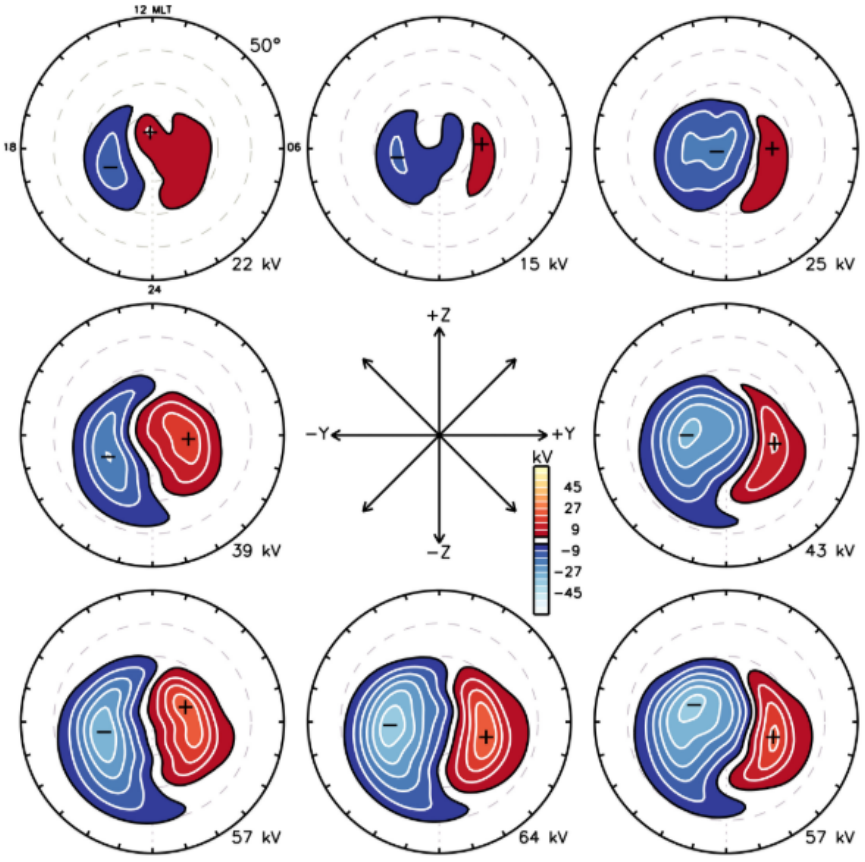

FIGURE 2.2: Statistical convection patterns sorted by interplanetary magnetic field clock angle taken from *Thomas and Shepherd* (2018). Electrostatic potential is indicated by colour according to the scale near the centre of the figure. The patterns are rotated so that noon (12 MLT) is at the top and dusk (18 MLT) on the left. All plots have a low latitude boundary of 50° magnetic latitude. The locations of the potential maxima (plus signs) and minima (minus signs) are marked.

the dayside 'cusp' region between the dawn and the dusk cell. For $+Y_{GSM}$ it is moved to later local times. This is consistent with asymmetries introduced into the convection geometry discussed in the previous section. The newly connected field lines under asymmetric reconnection are pulled to dawn and dusk due to the field tension effect (*Jørgensen et al.*, 1972; *Svalgaard*, 1973; *Cowley et al.*, 1991). B_y asymmetries in the nightside region for southward IMF are not so easy to observe. In the case for Figure 2.2 there is a low latitude portion of the dusk cell which extends across midnight in all cases. The nightside region is associated with tail reconnection thus the closure of open flux and its return to the dayside (*Dungey*, 1961). Therefore it is this reconnection and associated internal magnetospheric process that will dictate the convective flow. Tail region geophysical phenomena are observed to heavily influence the nightside flows, for example, magnetospheric substorms which are covered in greater detail in section 2.3 (*Provan et al.*, 2004; *Grocott et al.*, 2010). During substorm times and strong IMF B_y asymmetries the nightside convection pattern is governed by the substorm tail dynamics and not IMF B_y. One such asymmetry is the Harang discontinuity (*Maynard*, 2008) which can be seen in figure 2.2 as an extension of the dusk cell across the midnight sector. Another example is that of Subauroral Polarization Streams (SAPS) which can drive intense westward plasma flows further enhancing the extended dusk cell nightside configuration (*Foster and Vo*, 2002; *Zou et al.*, 2009)

2.2 Time Dependent Convection

Dayside reconnection converts closed flux to open flux as terrestrial closed field lines are 'opened' to the IMF, as such the dayside reconnection rate quantifies the addition

of open flux added to the magnetospheric system in a given time. This rate depends on the incoming solar wind IMF and plasma parameters. The nightside reconnection rate depends on conditions in the magnetotail and quantifies the closure of open flux from the system. These two rates do not have to be equal (*Coroniti and Kennel*, 1973; *Siscoe and Huang*, 1985; *Freeman and Southwood*, 1988; *Cowley and Lockwood*, 1992; *Milan et al.*, 2009a). The changes in amount of open flux lead to an expansion and contraction of the polar cap, for example *Russell* (1972) first suggested a relationship of the polar cap area to the amount of open flux contained within the magnetosphere. *Siscoe and Huang* (1985) attributed changes in the polar cap area to differing dayside and nightside reconnection rates and that differing IMF conditions create preferences for which one dominates. *Cowley and Lockwood* (1992) introduced the idea of the expanding-contracting polar cap (ECPC) paradigm which describes the rate of change of flux in the polar cap area (PCA):

$$\frac{dF_{PC}}{dt} = \Phi_D - \Phi_N = \frac{d}{dt}\int \vec{B}.ds \tag{2.1}$$

where F_{PC} is the polar cap flux, Φ_D and Φ_N are the dayside and nightside reconnection rates and where $\frac{d}{dt}\int \vec{B}.ds$ is the integral of the magnetic field $\vec{B}$ over the surface S of polar cap.

Enhanced dayside reconnection and thus Φ_D is driven by efficient solar-wind magnetosphere coupling at the magnetopause. This is well associated with intervals where the solar wind IMF contains a negative B_z component (*Siscoe and Huang*, 1985; *Craven and Frank*, 1987; *Milan et al.*, 2003, 2007, 2008). Figure 2.3 (a) shows a sketch of the ionospheric convection pattern associated with enhanced dayside reconnection. The solid

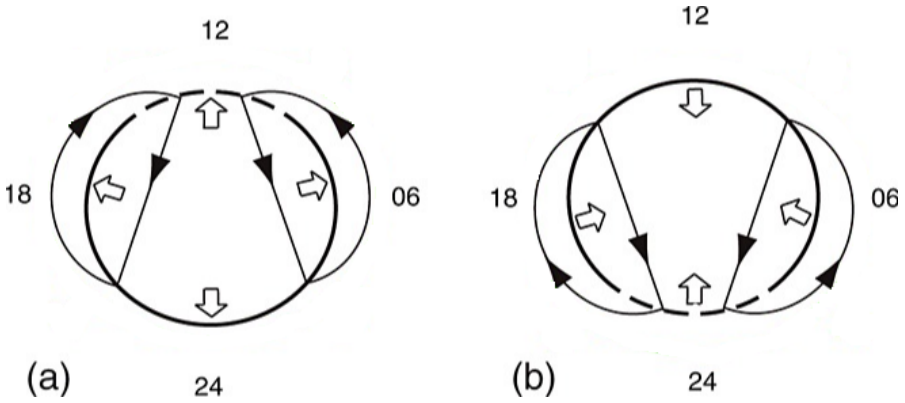

FIGURE 2.3: Ionospheric convection driven by a) dayside magnetic reconnection and b) nightside magnetic reconnection. The plots are oriented so that noon (12 MLT) is to the top and dusk (18 MLT) is to the left. The solid black lines mark the OCB with the dotted portion the ionospheric projection of the reconnection line. The curved arrowed lines represent convection streamlines and the white arrows the expansion (contraction) of the polar cap for dayside (nightside) driving. [Adapted from *Imber et al.* (2013)]

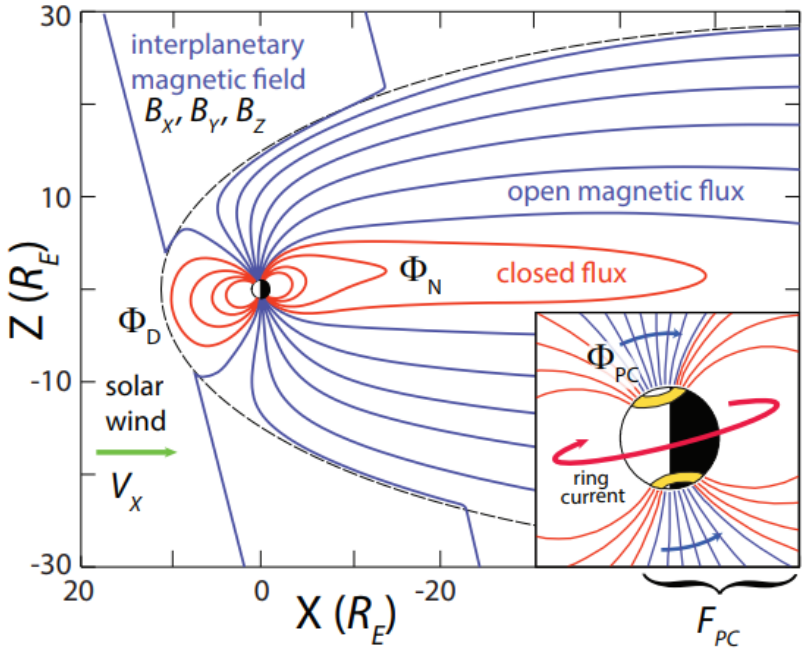

FIGURE 2.4: A schematic, side-on view of the magnetosphere to show the open (blue lines) and closed magnetic flux (red lines) in the magnetosphere.Φ_D (Φ_N) is the dayside (nightside) reconnection rate. The inset panel shows the relationship between the open flux, polar cap area and the auroral oval (yellow). [Adapted from *Milan et al.* (2012)]

circular line represents the OCB with the dashed portion the region over which magnetic reconnection takes place. The curved arrowed lines represent the ionospheric flow streamlines driven as a result of the reconnection. Here the arrows pointing outwards show the polar cap expanding. A similar sketch is shown in Figure 2.3 (b). In this case the increase of magnetic flux into the magnetosphere has caused the current sheet to thin (*Hones and Alamos*, 1979) and break up leading to nightside reconnection. This figure shows the subsequent decrease of polar cap area as open flux is closed and returned to the dayside. At any given time the polar cap area is a function of the nightside and dayside reconnection rates. Figure 2.4 shows a schematic of the open and closed flux in the magnetospheric system. The footprints of the open flux are shown in blue and closed flux in red. The poleward edge of the auroral oval is denoted in yellow and lays analogous to the open closed field line boundary.

The changing polar cap area and its relationship to solar wind-magnetosphere-ionosphere coupling makes it an important feature of the high latitude region. The open flux can be estimated with accurate mapping of the (OCB) which in turn can quantify the dynamic movement of the polar cap area. Many proxy boundaries for the OCB have been presented utilising different features of the magnetosphere-ionosphere and both ground and space based instruments. This thesis presents a new technique which uses ground based radar observations (see chapter 4) and investigates its applicability as a proxy for the OCB (see chapter 6). Further consideration of the recent literature discussing OCB proxies and their determination using a variety of techniques and datasets is presented in chapter 6.

2.3 Magnetospheric Substorms

2.3.1 Phases of the substorm cycle

The previous section outlined that the dayside and nighside reconnection rates can act independently and that the amount of open flux in the polar cap at a given time is a function of both of these rates. This imbalance in the dayside and nightside reconnection can give rise to many geophysical phenomena, notably the magnetospheric substorm. The substorm is first initiated by enhanced dayside reconnection and undergoes three distinctive phases which will be outlined below. The entire substorm cycle lasts on timescales of a few hours.

The first part of the cycle is referred to as the growth phase. The growth phase is typically triggered by a southward turning of the IMF causing enhanced dayside reconnection and open flux to be loaded into the magnetotail. The substorm process is shown schematically in Figure 2.5 with the top panel showing the key features of the growth phase. The *Distant Neutral Line* (DNL) is a distant tail reconnection site where open flux is steadily closed and returned to the dayside. The addition of magnetic flux to the tail lobes is accompanied by the thinning of the plasma sheet and a more stretched tail configuration (see Figure 2.5). The loading of the magnetotail lasts, on average, one hour before it becomes unstable and the next phase (*the expansion phase*) is triggered.

The expansion phase is accompanied by a significant reconfiguration of the magnetosphere lasting on the order of 30-40 minutes. The stretched configuration now becomes more dipolar as is sketched in the middle panel of Figure 2.5 and accelerates plasma towards the Earth. As the magnetotail dipolarises part of the neutral sheet current is

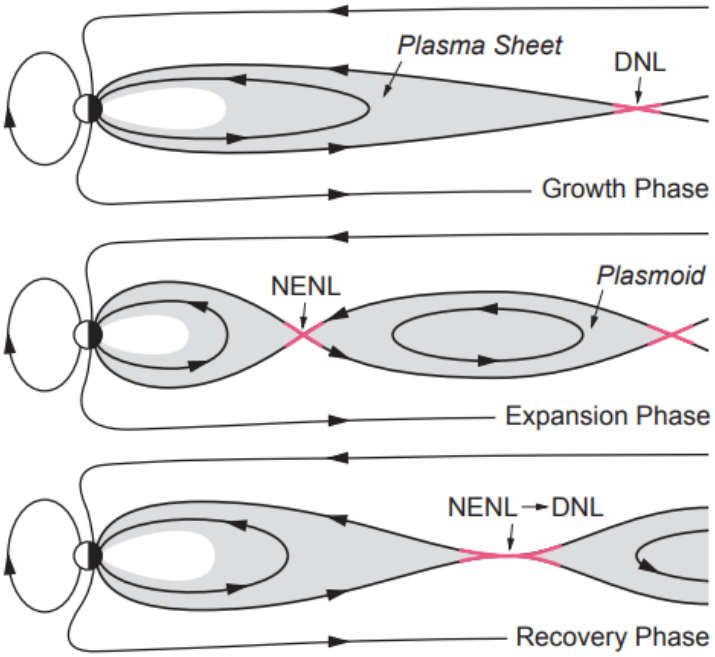

FIGURE 2.5: The three panels show the growth, expansion and recovery phases of the substorm respectively. The pink regions show the locations where magnetic reconnection takes place (*Baumjohann and Treumann*, 1996)

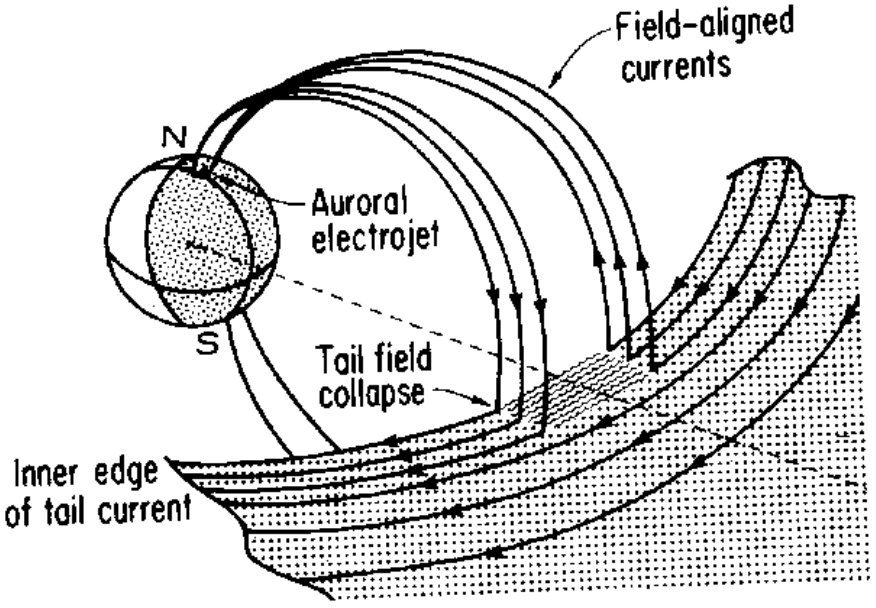

FIGURE 2.6: A schematic illustration of the substorm current wedge (*Kivelson and Russell*, 1995) which shows the mechanism of how the neutral sheet current diverts into the ionosphere.

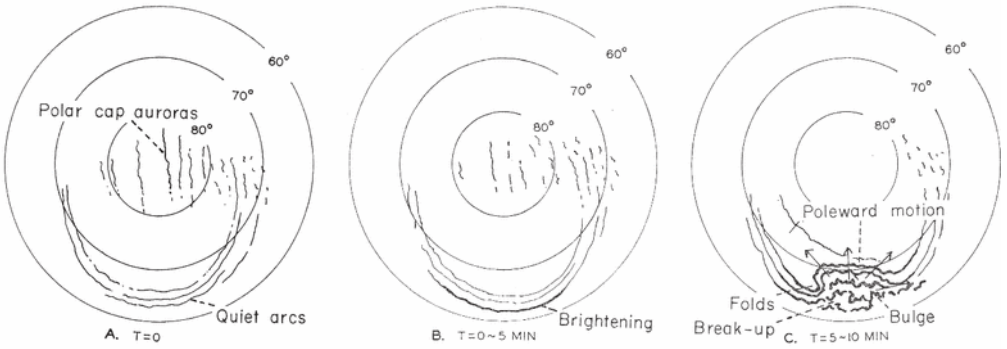

FIGURE 2.7: Schematic representation of the auroral development for the substorm growth (left) and expansion phase onset (middle and right) [Adapted from *Akasofu* (1964)
]

diverted into the ionosphere via the substorm current wedge, sketched in Figure 2.6. The closure of this current in the ionosphere results in intense magnetic disturbances in the polar region. There are a number of competing theories as to the exact mechanism that triggers the expansion phase. Some observations suggest that the expansion phase is initiated by an instability in the near-Earth current sheet that is followed by tailward-propagating plasma e.g. (*Lui*, 1991, 1996). Others suggest that it is reconnection in the near-Earth plasma sheet (*Near Earth Neutral Line* (NENL)) and tailward-propagating plasma that occurs first. A comprehensive review of the NENL model can be found in *Baker et al.* (1996). The NENL phemonology is the one sketched in Figure 2.5 and as the NENL initiates on closed field lines this reconnection process results in the formation of a plasmoid. The plasmoid is unusual as the NENL reconnection process initiates on closed field lines which creates a loop of closed field lines that are not connected to anything.

The final phase, the recovery phase occurs about 45 minutes after the expansion phase onset. At this time the dipolar configuration of the magnetotail begins to return back into a relaxed state and the NENL moves tailward as seen in the bottom sketch of Figure

2.5. The plasmoid is also pushed tailward until it is ejected from the magetotail. At some point the NENL will move far enough tailward and become the DNL.

One of the most recognised signatures of the start of the substorm expansion phase is auroral brightenings in the ionosphere as a result of particles being accelerated into the ionosphere from the magnetotail. The aurora actually exhibits a characteristic morphology throughout all three substorm phases (*Akasofu*, 1964) and figure 2.7 shows a sketch highlighting some of the key features. The first plot shows, as the growth phase is initiated auroral arcs move equatorward. The auroral 'onset' is signalled by a brightening of the most equatorward arc in the pre-midnight region which subsequently expands rapidly poleward and westward and forms a bright bulge (auroral break up) as shown in the final plot. The substorm expansion phase is so-called due to the observed expansion of the auroral disturbance. During the recovery phase of the substorm the auroral features begin to dim and once again become quiet arcs.

2.3.2 Substorm effect on convection

Although substorms are initiated by enhanced dayside driving, the expansion phase and associated effects occur in the magnetotail and are imposed on the nightside ionosphere. The enhancement of the ionospheric currents and particle precipitation can affect the nightside convection. For example, *Weimer* (2001, 1999, 2005) derived ionospheric electric potential maps using Dynamic Explorer 2 spacecraft observations of the ionospheric electric field. The study separated observations into substorm and non-substorm times, and it was found that the Harang discontinuity (*Maynard*, 2008) became much more

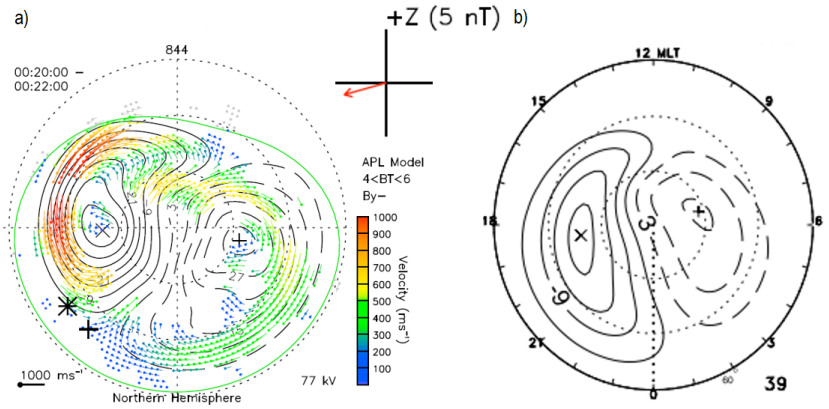

FIGURE 2.8: Statistical Ionospheric convection maps for a) substorm times where the onset MLT was between 20-22 MLT taken from *Grocott et al.* (2010) and b) a climatological model derived from IMF B_y- dominant observations taken from *Ruohoniemi and Greenwald* (2005). Noon is orientated to the top of the figure and dusk to the left. The curved solid and dashed lines show the equipotential lines.

pronounced during the substorm intervals. Dawn-dusk asymmetries have also been observed in the nightside region as the ionospheric flow diverts around the substorm onset location as a result of the high conductivities associated with the expansion phase e.g. (*Yeoman et al.*, 2000; *Grocott et al.*, 2009, 2010, 2017).

Figure 2.8a shows a SuperDARN convection map taken from *Grocott et al.* (2010) showing an average convection pattern 20 minutes after the substorm expansion phase and where the substorm onset location was between 20 and 22 MLT i.e. 'early' onset substorms that occur at earlier local times than the average of 23 MLT (*Frey*). Figure 2.8b shows a corresponding climatological convection pattern from *Ruohoniemi and Greenwald* (2005) that shows the expected pattern for the given IMF B_y orientation. In Figure 2.8a the dayside region follows the expected asymmetry for the IMF By condition but the nightside shows an opposite relation. The dawn cell is extended into the pre-midnight sector and aligns more closely with the substorm onset location (20-22 MLT) suggesting

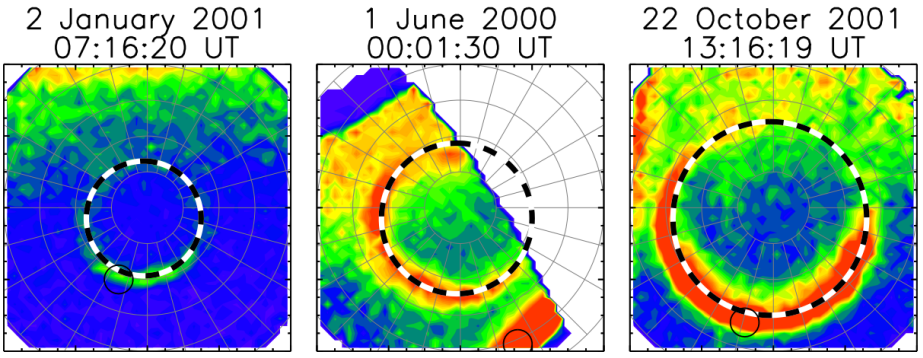

FIGURE 2.9: Auroral observations with fitted circles overlayed to show the size of the poleward auroral boundary for three different examples (*Milan et al.*, 2009a)

that the nightside flows are modified substantially by substorm onset location.

2.4 Dependencies on the auroral oval radius

In sections 2.2 and 2.3 the concept of time-dependant reconnection and how magnetospheric substorms arise as a consequence of this are considered. The poleward auroral boundary is intrinsically linked to these features as it aligns with the polar cap boundary and can be thought of as a proxy for the OCB.

Figure 2.9 (*Milan et al.*, 2009a) shows examples of three different sizes of the auroral radius, here circles are fitted to the auroral data and demonstrate the possible latitudinal extent of the polar cap area. In this example, from the first panel to the last panel, the auroral radius has increased by 15° MLAT.

During the substorm cycle the radius of the auroral oval becomes more variable as it responds to the dynamic changes in the dayside and nightside reconnection rates. The radius of the auroral oval has been well correlated to the IMF B_z component and increases under the influence of more negative IMF B_z as is typical of the substorm growth phase

(*Holzworth and Meng*, 1975; *Nakai et al.*, 1986). The ECPC can explain this relationship of polar cap growth during the growth phase, attributing it to the prevailant solar wind conditions. However, it is not able to reveal information on what level of open flux is sufficient to trigger a substorm expansion phase. *Milan et al.* (2007, 2008) and *Boakes et al.* (2009) observed that following the substorm growth phase, the expansion phase occurred for different levels of open flux in the magnetosphere. This suggests that there are other significant contributing factors in addition to the solar wind conditions that influence the size of the polar cap during substorm intervals. *Nakai and Kamide* (2002) suggested that an enhancement of the ring current could be responsible and so ultimately, the preconditioned state of the magnetosphere has an impact on the amount of open flux that can be added to the polar cap.

The location of the poleward auroral boundary well captures the size of the polar cap and its dynamic changes resulting from solar-wind - magnetosphere coupling.The main focus of this thesis is to derive a new boundary identification technique using ionospheric convection data and to compare it to other datasets. Chapter 6 utilises the poleward auroral boundary in order to study and validate this boundary.

Chapter 3

Instrumentation and data methods

This chapter presents the instrumentation and datasets used for the work of this thesis. Global high latitude convection estimates measured by the Super Dual Auroral Radar Network (SuperDARN) form the primary dataset. The general principles of coherent scatter radars and the SuperDARN network are presented before a more detailed outline of the fitting algorithm used to generate large-scale convection patterns. This work uses a standardised set of SuperDARN generated ionospheric convection maps that have been made available for public use (ECLAT dataset) which also is introduced here. Finally, the Imager for Magnetopause-to-Aurora Global Exploration (IMAGE) spacecraft is briefly described as auroral images taken from IMAGE are utilised as a supplementary dataset to compare to SuperDARN observations.

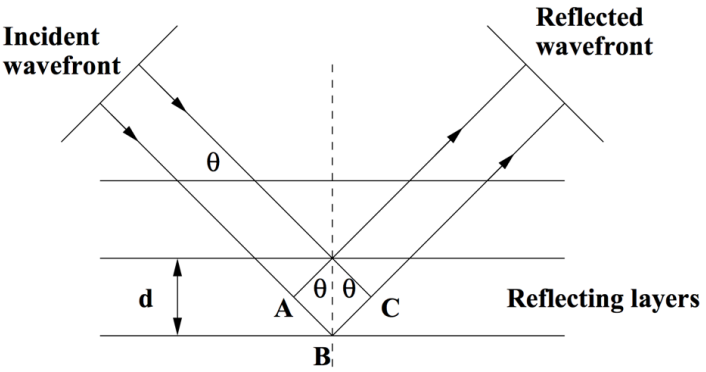

FIGURE 3.1: A schematic to show the basic principle of Bragg Scattering. The incident wavelength shows the path of two waves. The solid horizontal lines represent the planes within a material, d is the separation width and the dashed line represents the normal. One wave travels an additional AB-BC distance in its path and interferes constructively with the other reflected wave. An incident wavelength of d/2 will give the condition for maximum constructive interference.

3.1 SuperDARN

3.1.1 Coherent Scatter Radars

High Frequency (HF) Coherent scatter radars exploit the spatial coherence of small-scale electron density irregularities in the ionosphere that are sensitive to Bragg scattering. Before the use of HF coherent scatter radars there were geometrical constraints on the ability to sense certain ionospheric regions. Historically, coherent scatter radar measurements were usually made with VHF and UHF frequencies. At high latitudes when the magnetic field is almost vertical it is impossible for coherent VHF and UHF to probe above E region altitudes.

Figure 3.1 shows a simple schematic highlighting the principle of Bragg scattering with the three horizontal lines representing three structured planes within a given material. The incident wave front highlights two possible ray paths, each reflecting from a different plane. The ray reflecting at point B travels an additional distance (AB - BC) and thus

for the ray to interfere constructively with the rays travelling on other ray paths this distance must equate to the incident wavelength λ_t (this will give maximum constructive interference, at other fractions of λ_t the intensity of the reflected wavefront will reduce). The following formula describes the relationship between the plane separation (d), the incident wavelength λ_t and the incident angle (θ).

$$d = \frac{\lambda_t}{2sin(\theta)} \tag{3.1}$$

The necessary conditions for Bragg scattering are:

- The angle of incidence must equal the angle of reflection
- Reflections from several planes must add constructively.

In the Ionosphere, F region field aligned electron density irregularities are produced by a number of processes - some of which are mentioned in the review by *Fejer and Kelley* (1980). For the high latitude F region the most common plasma instability is the gradient drift instability (*Tsunoda*, 1988). The gradient drift instability occurs in the presence of electron density gradients and can be formed in two ways. 1) In the auroral zone via structured soft precipitation. 2) Structured convection in the presence of solar EUV ionization gradients. The irregularities last on the order of a few hours (*Kelley et al.*, 1982) and drift at the $\vec{E} \times \vec{B}$ velocity following the typical ionospheric convection pattern.

F region field aligned irregularities have a wave-vector number that is close to orthogonal to the magnetic field. When the wave-vector K satisfies the condition $K = +/ - 2K_r$

where K_r is the radar radio wave vector, the wavelength of the ionospheric irregularity K is half the transmitted radio wave K_r such that the reflected waves will constructively interfere and produce a signal that is strong enough to be detected. As has been discussed there are two conditions required for Bragg scattering, the first being that the reflected waves from several planes add constructively (mentioned above) and that the angle of incidence is equal to the angle of reflection. In order to achieve a return signal detected by the radar the incident radar wave must reach the ionospheric irregularity at 90 degrees. The HF radar frequency range means that it is able to refract in the ionosphere in such a way to achieve the orthogonality condition.

The variation in electron density at ionospheric altitudes influences radio wave propagation and causes the radio waves to refract. In a simple approximation the ionosphere can be thought of as a stack of thin slabs with refractive indices, n_1, n_2, n_3 etc. Snells law describes the relationship between the angles of incidence and refraction as the electromagnetic wave encounters a boundary between two different mediums (i.e. the thin ionospheric slabs) and is stated as:

$$\frac{\sin\theta 2}{\sin\theta 1} = \frac{n_2}{n_1} \tag{3.2}$$

where $\sin\theta 1$ is the angle of incidence, n_1 is the refractive index of the incident medium, $\sin\theta 2$ and n_2 refer to the refracted angle and refractive index of the second medium. The refractive index decreases when moving from a medium of lower to higher electron density. As the plasma frequency increases with height (up to F-region altitudes) as

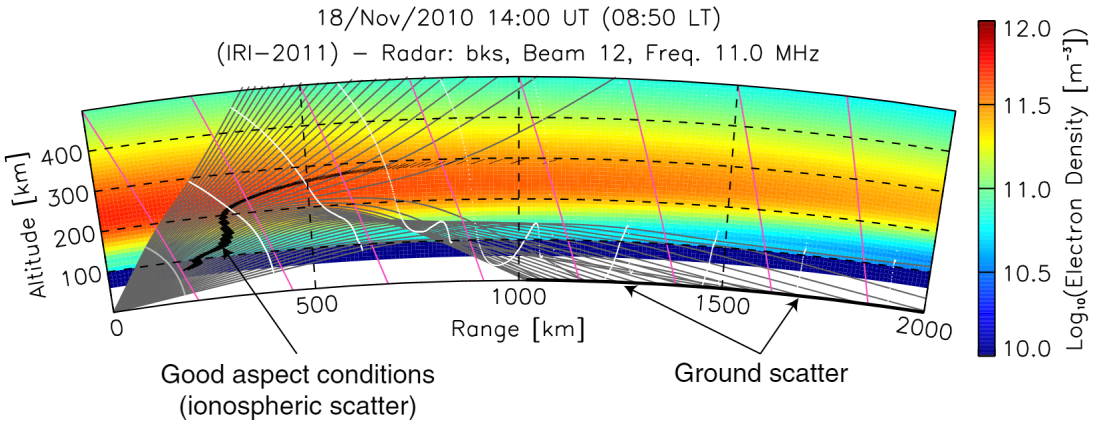

FIGURE 3.2: Ray tracing results to illustrate the HF radio wave propagation into the mid-latitude ionosphere for varying elevation angles (Figure 3 of *de Larquier et al.* (2013)). The electron density is colour-coded from blue to red, pink lines represent the background geomagnetic field lines, rays are shown as gray and the black segments mark the regions where the orthogonality condition can be met.

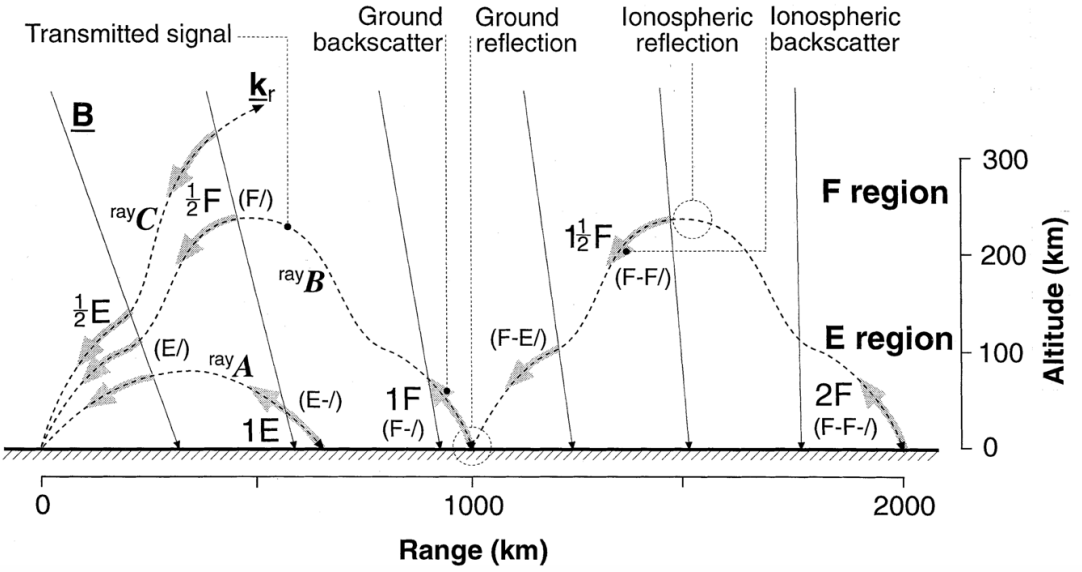

FIGURE 3.3: A schematic taken from Figure 1 of *Milan et al.* (1997) to show possible propagation modes and regions in which backscatter can occur. Three possible ray paths are shown, A, B and C. Ray A a possible E region mode with the possibility of multiple hops. Ray B a higher elevation angles showing a possible F-region mode that produces both near and far backscatter. Ray C shows a ray that penetrates the ionosphere.

seen in Figure 1.10 the refractive index decreases and causes the ray to gradually bend towards the horizontal.

Figure 3.2 illustrates the effect of the angle of incidence (elevation angle) of a radio wave propagating into the mid-latitude ionosphere. The electron density is shown colour-coded from blue (low) to red (high) with a peak at approximately 250km, the background geomagnetic field is shown by the pink lines, each ray is plotted in gray and black segments mark the regions where the orthogonality condition is met. As the elevation angle increases, the path of the radio wave reaches higher altitudes and experiences less refraction until it is able to penetrate through the ionosphere. At lower elevation angles they are refracted to such an extent that they turn back towards the earth's surface and hit the ground. It is also possible for the signal to hit the ground and 'hop' forward to produce multi-hop waves.

Figure 3.3 shows schematically some possible propagation modes of the transmitted radar wave (taken from *Milan et al.* (1997)). The figure highlights three possible radio wave vectors (K_r) emanating from the radar. The magnetic field direction is shown as the straight arrowed lines directed into the ground. Ray A is transmitted at the lowest elevation angle and is refracted and reflected in the ionosphere at E region altitudes. Ray B has the next highest elevation angle and shows an F region mode. This ray path shows multiple hops and returned backscattered signals from a near and far range. Ray C has the highest elevation angle and is not refracted sufficiently to meet the orthogonality condition and the signal is lost as it penetrates the ionosphere. Signals refracting from E or F region altitudes and returning to ground will produce backscattered signal (ground-scatter). In Figure 3.3 this can be seen at the 1E, 1F and 2F locations, i.e. integer hops.

Signals returned from the receiver from ground typically have different characteristics than those returned from the ionosphere, namely much smaller velocities and spectral widths, meaning they can be easily identified.

3.1.2 The SuperDARN Network

SuperDARN stands for the Super Dual Auroral Radar Network (*Greenwald et al.*, 1995). The first SuperDARN radar was built and commenced operation in Goose Bay in 1983 (*Greenwald et al.*, 1985). This radar was an electronically steerable, narrow beam phased-array HF radar and its design essentially became the blueprint for other SuperDARN radars to come. The design consists of 16 log-periodic antennae operating in the HF range between (8-20) MHZ, each of its 16 beams are separated in azimuth by 3.2° giving a radar field of view of 52°. The range resolution of the radar is determined by the transmitted pulse length (300μs) which translates to approximately 45km per range gate. There are 75 range gates meaning the range covers 200-3000km. Each scan across all 16 beams takes between 1 and 2 minutes to complete. Since 1983 the network has continued to grow and at present day oparates over 30 radars in both hemispheres, with 22 of those in the northern hemisphere.

Figure 3.4 shows the location and field of view (F.O.V) of all operational radars in the northern hemisphere for the time periods a) 2000-2002 and b) 2010-2012. The earlier time period coincides with the IMAGE auroral observations which is why it is included here. The later time period covers the last two years of the ECLAT SuperDARN dataset and is used in a comparative analysis in Chapter 5. The colours indicate the latitudinal extent of the radar F.O.V. These include the original high latitude SuperDARN radars

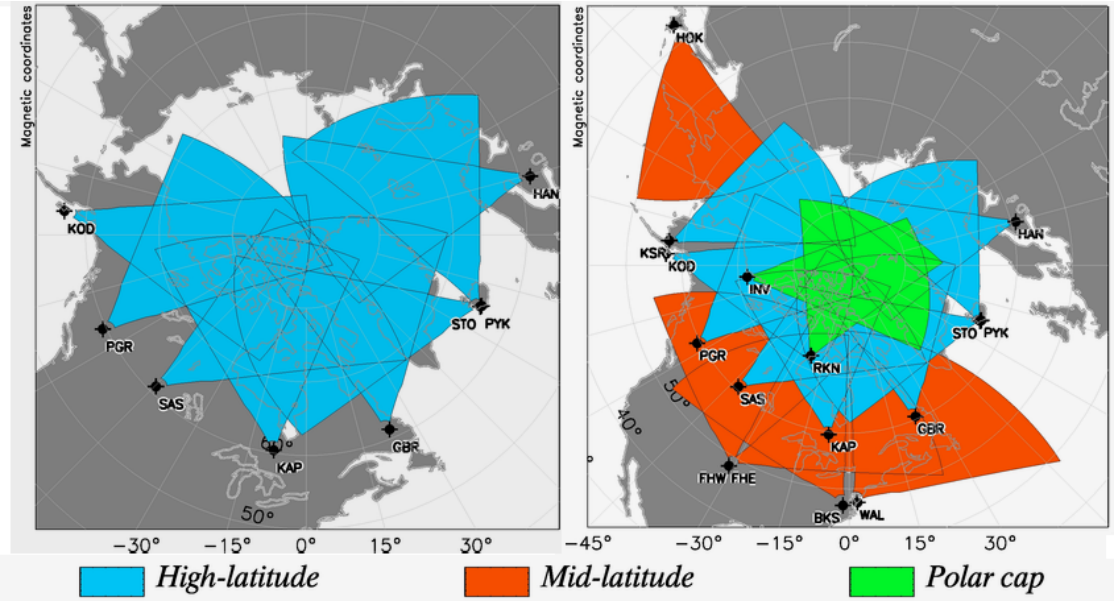

FIGURE 3.4: The locations and fields of view of all operational SuperDARN radars in the Northern hemisphere for a) 2000-2002 and b) 2010-2012. [image credit: vt.superdarn.org]

(blue) and the later additions of the mid-latitude 'StormDARN' (red) and polar cap 'PolarDARN' (green) radars. The additions of the polar cap and mid-latitude radars were to enrich coverage over the highest latitude region and have the capability to map the convection during disturbed periods when the latitudinal extent of the convection expands equatorward. Although the radars in the SuperDARN network follow the design of the initial Goose Bay radar some slight differences between them do exist, but all radars process the backscattered signal on-site to produce estimates of the backscattered power, line-of-sight Doppler velocity and spectral width.

3.1.3 The 'Map potential' convection fitting algorithm

As discussed SuperDARN offers a unique view of the high-latitude convection by combining line of sight velocity measurements from many radar sites. Many radars operate in pairs offering two look angles for returned backscatter signals to fully resolve the

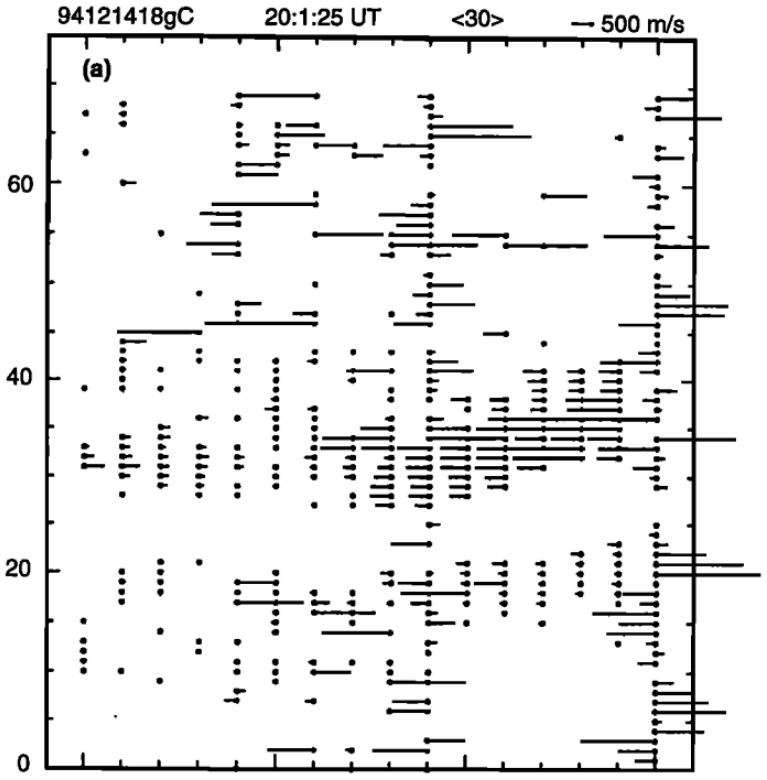

FIGURE 3.5: line-of-sight velocity data collected at 14 December 1994 20:01 UT plotted against beam number and range gate (0-74), taken from figure 1 of *Ruohoniemi and Baker* (1998).

two-dimensional $\vec{E} \times \vec{B}$ velocity. To use only line of sight measurements captured by at least two radar F.O.Vs leads to a large quantity of data that must be disregarded. This can have a big impact on the ability of SuperDARN to estimate the global high latitude convection effectively. *Ruohoniemi and Baker* (1998) outline a different method which utilizes all available line of sight data to estimate the global convection pattern. The details are summarized here:

Figure 3.5 shows an example of line of sight data returned from the Goose Bay radar on December 14 1994 20:01 UT. The first step of the preprocessing involves filtering the velocity measurements from an individual radar both spatially and temporally to remove variability due to interference and small-scale plasma transport effects.

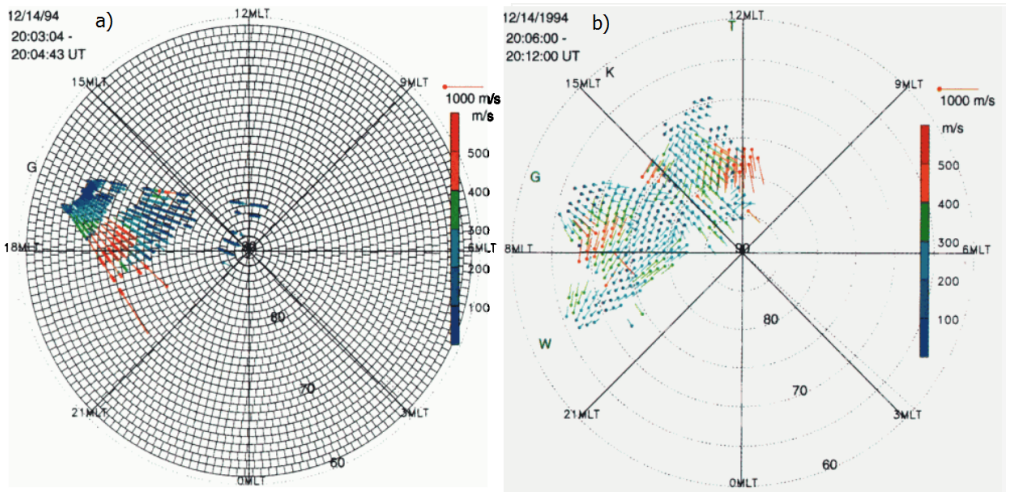

FIGURE 3.6: Two plots taken from Plate 2 and 3 *Ruohoniemi and Baker* (1998). a) A sample of the velocity data for the Goose Bay radar on 14 December 1994 20:03-20:04 UTC overlaid on a plot showing the spatial averaging used for the filtered velocity data from all available radars. The equal area grid spans 1 degree in latitude by 111km in longitude.12:00 MLT is shown to the top of the plot and line of sight velocities are colour-coded from 100-1000m/s and scaled to the length of the reference arrow shown. b) Plot of the line-of-sight velocities for four operational radars on 14 December 1994, 20:06-20:12 in the coordinate system outlined in a).

A boxcar filter is used on a 3x3 range gate/beam centred on a cell of interest at time t_k, t_{k+1} and t_{k-1}. For a cell of interest the line of sight velocity is collected from three scan times over a larger spatial area with a higher weight given to the centred cell at time t_k. The sample is then median filtered to give a best-estimate of the line of sight velocity in the centred cell. For a cell to be allocated a filtered velocity measurement it must hit a threshold of number of samples. A standard deviation is first calculated from all velocity samples although any measurements lying two standard deviations from the mean are removed and the uncertainty value assigned is calculated using the updated velocity samples. To remove erroneous data, measurements greater than 2000 m s^{-1} are removed along with measurements flagged as ground scatter which is identified based on a low velocity magnitude and narrow spectral width.

From here the data is transformed into an equal area grid centred on the magnetic pole. This is done for a few key reasons:

1) To avoid oversampling at the near-gate ranges, this would tend to skew a global solution if individual measurements were counted.

2) To allow easy comparison to alternative datasets

The equal area grid spans 1 degree in latitude (approximately 111km on the surface of Earth) by 111km in longitude. The number of grid cells varies by latitude according to:

$$n(\theta) = \mathrm{NINT}[360 \sin(\theta)] \tag{3.3}$$

Where θ is colatitude and NINT is a nearest integer function. The result of the gridding can be seen in figure 3.6a. Figure 3.6b shows the result of the averaged line of sight velocities from four operational radars on the 14 December 1994, 20:06 - 20:12 UT transformed in the equal area grid previously outlined.

The map potential technique, outlined below, utilizes all available line of sight velocity data to constrain 'best guess' large-scale convection patterns dictated by a spherical harmonic fit. The ionospheric electrostatic potential (Φ) is expanded in terms of spherical harmonic functions $Y_{l,m}$:

$$\Phi(\theta, \phi) = \sum_{l=0}^{L} \sum_{m=-M}^{M} A_{lm} Y_{lm}(\theta, \phi) \tag{3.4}$$

For real Φ:

$$\Phi(\theta,\phi) = \sum_{l=0}^{L} A_{lm} P_l^0 \cos(\theta) + \sum_{m=1}^{l} (A_{lm} \cos m\phi + B_{lm} \sin m\phi) P_l^m(\cos\theta) \tag{3.5}$$

where A_{lm} and B_{lm} are real valued coefficients (for Equation 3.4), L and M are the order and degree of the expansion where M $\leq$ L, P_l^m are the associated Legendre functions, θ the colatitude and ϕ the longitude.

The colatitude is replaced by a variable transformation $\theta^{'}$ that assumes the potential drops to zero at some low latitude limit (*Shepherd and Ruohoniemi*, 2000). This lower latitude limit is known as the Heppner-Maynard Boundary (HMB) and has a shape determined empirically by *Heppner and Maynard* (1987) using Dynamics Explorer 2 satellite data. Due to the non-uniform shape of the HMB, its size is described by the latitude at which it crosses the midnight meridian, termed Λ_{HM}. The effective co-latitude (to be used in equation 3.4) is thus given by:

$$\theta^{'} = \frac{\pi}{\frac{\pi}{2} - \Lambda_{HM}} \theta \tag{3.6}$$

The order of the spherical harmonic expansion (L) depends on individual requirements. The large-scale convection pattern can be resolved by expansions of a relatively small order i.e. L=4. To resolve small-scale features this can be increased to L=6 to L=8. The choice of the order of fit is a balance between a higher spatial resolution and increased dependence on the location and amount of radar data present.

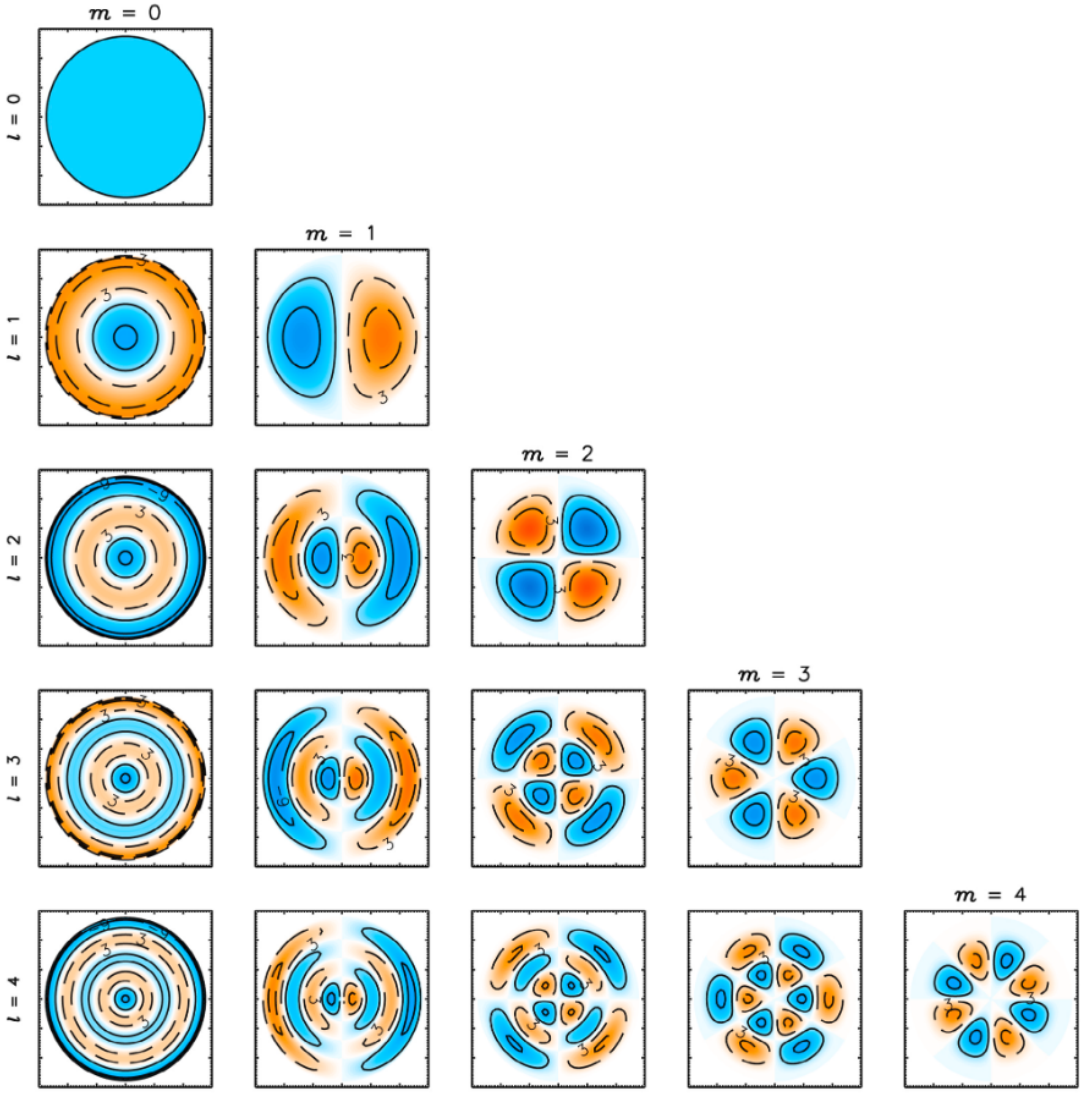

FIGURE 3.7: A plot taken from Figure 2 (*Grocott et al.*, 2012) which shows a set of polar projected electric potential patterns for the first four order basis functions associated with each of the coefficients A_{lm}. A_{lm} has been set artificially for each to clearly show the resultant pattern. The phase and rotation (in MLT) for each case has also been artificially set to 0.Increasing order l is seen down the page with increasing degree, m across the page.

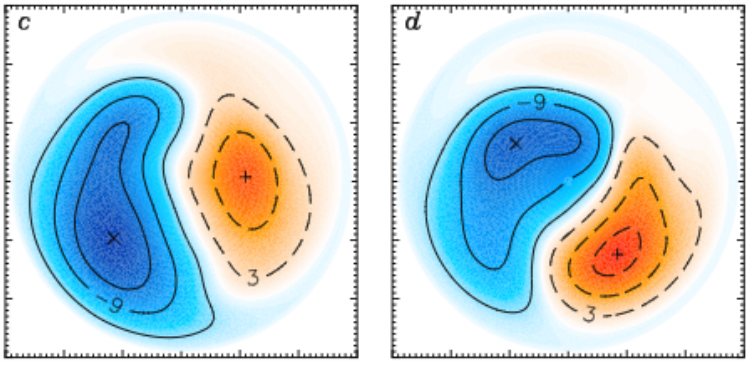

FIGURE 3.8: A plot taken from Figure 3 (*Grocott et al.*, 2012) highlighting two example resultant patterns from the fitting which are typically associated with B_y dominant IMF conditions, B_y+ and B_y- respectively (northern hemisphere)

Figure 3.7 gives an illustration of the first 4 degrees of the spherical harmonic expansion projected into polar coordinates at arbitrary latitude (*Grocott et al.*, 2012). In these images the amplitude A_{lm} has been artificially set to enhance each potential and the argument A_{lm} (i.e. the phase or rotation in magnetic local time) has been set to 0 for illustrative purposes. In reality the coefficients indicate the contribution of each basis function to the overall pattern including both the magnitude and rotation contributions. Figure 3.8 (*Grocott et al.*, 2012) shows two example resultant patterns from the fitting which are typically associated with B_y dominant IMF conditions, B_y+ and B_y- respectively (northern hemisphere). A high contribution from the m=1, l=1 basis function can be observed with rotation anticlockwise and clockwise respectively.

The ionospheric electrostatic potential is converted to velocity vectors allowing equivalence with the filtered line of sight radar data, represented by N velocities on the gridded map with associated uncertainty. The potential Φ is related to the electric field $\vec{E}$ and thus the velocity $\vec{V}$ by the following:

$$\vec{E} = -\nabla\Phi \tag{3.7}$$

$$\vec{V} = \frac{\vec{E}X\vec{B}}{B^2} \tag{3.8}$$

where $\vec{B}$ is the magnetic field vector.The best-fit convection pattern is dictated by the minimization of the following equation:

$$\chi^2 = \sum_{i=1}^{N} \frac{1}{\sigma^2}[\vec{V}[i].\hat{K}[i] - W_i]^2 \tag{3.9}$$

where $\vec{V}[i]$ is the fitted velocity vector at the i^{th} grid cell position. W_i and σ^2 represent the observed velocities and their respective uncertainties. The dot product projects the fitted velocity vector into the line of sight direction $\hat{K}[i]$. It is easy to see that the lower the value of χ^2 the better the global fit aligns with the observed data and so an appropriate representation of the convection can be determined.

Since the year of publication of the map potential method, the amount of SuperDARN radars in the northern hemisphere has largely increased but even so, there is never global coverage of line-of-sight velocities. If coverage is minimal or constrained to a small MLT/latitude area, then instabilities in the resultant model can arise as the solution becomes unphysical in regions far from the observed data. This is combated by the introduction of additional velocity data inputted on a global spatial scale that depends on the order of the fit. The additional velocity data comes from a statistical model published by *Ruohoniemi and Greenwald* (1996) which took data over approximately 5.5

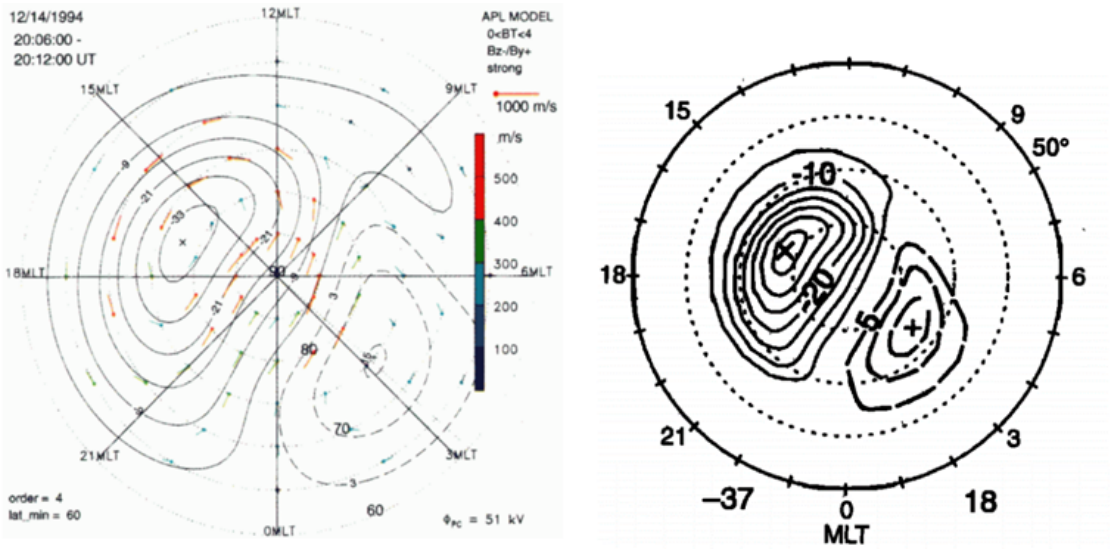

FIGURE 3.9: a)Taken from Plate 7 of *Ruohoniemi and Baker* (1998) showing the spatial resolution of the fitted vectors which come from the statistical model (RG96) sampling for an example case of 14 December 1994 20:06-20:12 for an order 4 spherical harmonic fit. b) Taken from Figure 7 (*Ruohoniemi and Greenwald*, 1996) to show the statistical average of the convection pattern for the IMF magnitude and direction, $0 \leq B_t \leq 4$ nT and B_y+ / B_y-.

years from the Goose Bay radar and determined the climatological patterns characterized by IMF magnitude and direction hereafter referred to as the RG96 model.

Figure 3.9a shows the statistical sampling of velocity data for 14 December 1994 20:06 - 20:12 UT and 3.9b shows the derived climatological pattern from the RG96 model for the IMF direction and magnitude for that time period. Note, the latitude scales are slightly different but serves as an illustration of the spatial resolution of the statistical sampling for a fit with order 4 and the climatological model from which it is derived.

The resultant pattern for the example of 14 December 1994 20:06-20:12 that combines the line-of-sight velocity data shown in figure 3.6b with the statistical sampling shown in figure 3.9 can be seen in figure 3.10. Following this map potential method all available line of sight radar velocity measurements can be used to estimate the global large scale convection pattern at two minute cadence.

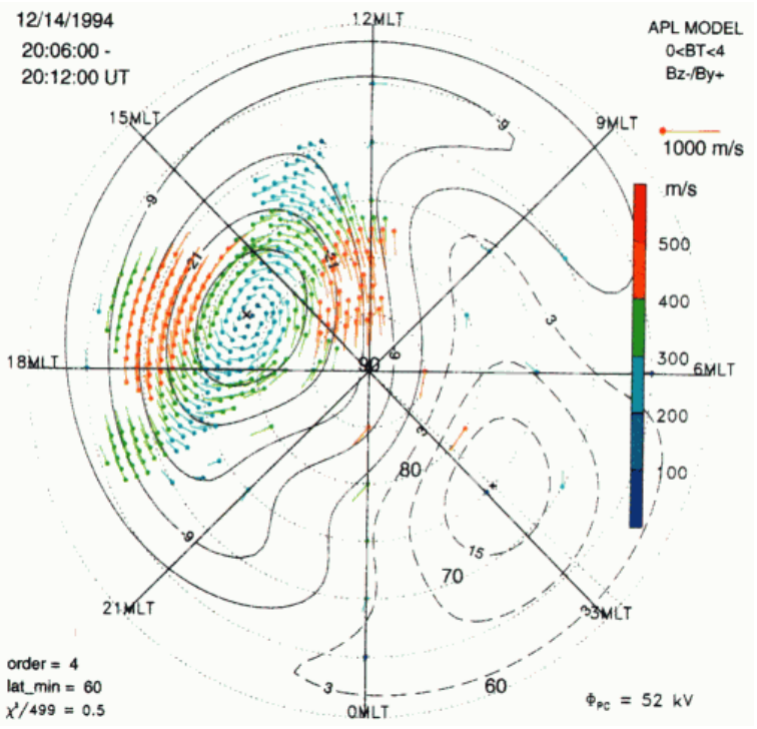

FIGURE 3.10: a)Taken from Plate 5 of *Ruohoniemi and Baker* (1998) showing solution of the global convection pattern by fitting the line-of-sight velocity data shown in figure 3.6b to order 4 of the electrostatic potential and including the statistical sampling shown in figure 3.9.

3.1.4 ECLAT

The European Cluster Assimilation Technology (ECLAT) project was set up to provide additional datasets for the Cluster Active Archive (*Laakso et al., 2009*). For example, this includes auroral observation and magnetometer data as well as spacecraft field line mapping into the ionosphere. The idea was to create a common repository containing a wide range of space-based and ground-based observations that is easily accessible and to make comparative analysis as straightforward as possible. The University of Leicester provided the addition of SuperDARN ionospheric global convection maps to the ECLAT project. A complete summary is given by (*Milan et al.*) although some relevent details are shared below.

The SuperDARN data created for ECLAT contains only the fully processed data. There are no raw line of sight measurements but only global convection map estimates where any raw data has been assimilated by the previously described map potential technique. All maps are generated with an L=6 order of expansion as is commonly used. The location of the Heppner-Maynard boundary (HMB) is determined in the standard way given by the map potential procedure. This means that the boundary is placed at the lowest latitude where there are three radar observations of at least 100 ms^{-1}. ECLAT SuperDARN data is available for twelve years spanning 2000-2012. The ECLAT dataset is used in this thesis such that the results presented are directly applicable to this widely used and publicly available dataset.

3.2 IMAGE FUV

Global auroral imagery allows indirect observation of the ionospheric response to solar-wind magnetospheric processes that govern the high-latitude polar regions. The Imager for Magnetopause-to-Aurora Global Exploration (IMAGE) spacecraft was launched on 25 March 2000 to investigate the response of the magnetosphere to the time-variable solar wind. One of its main objectives was to provide images of the polar regions with a full view of the auroral oval throughout its orbit. *Mende et al.* (2000b,a) provides a comprehensive view of all objectives and instruments that make up the IMAGE satellite.

Figure 3.11 shows a diagram of the IMAGE orbit progression for the first two years. The satellite had a 90° inclination with 7 R_E altitude at apogee and 1000km at perigee with a 13.5 hour orbital period. (*Mende et al.*, 2000b; *Burch*, 2000). IMAGE data is available from May 2000 until August 2005 although this thesis only utilises data from May 2000

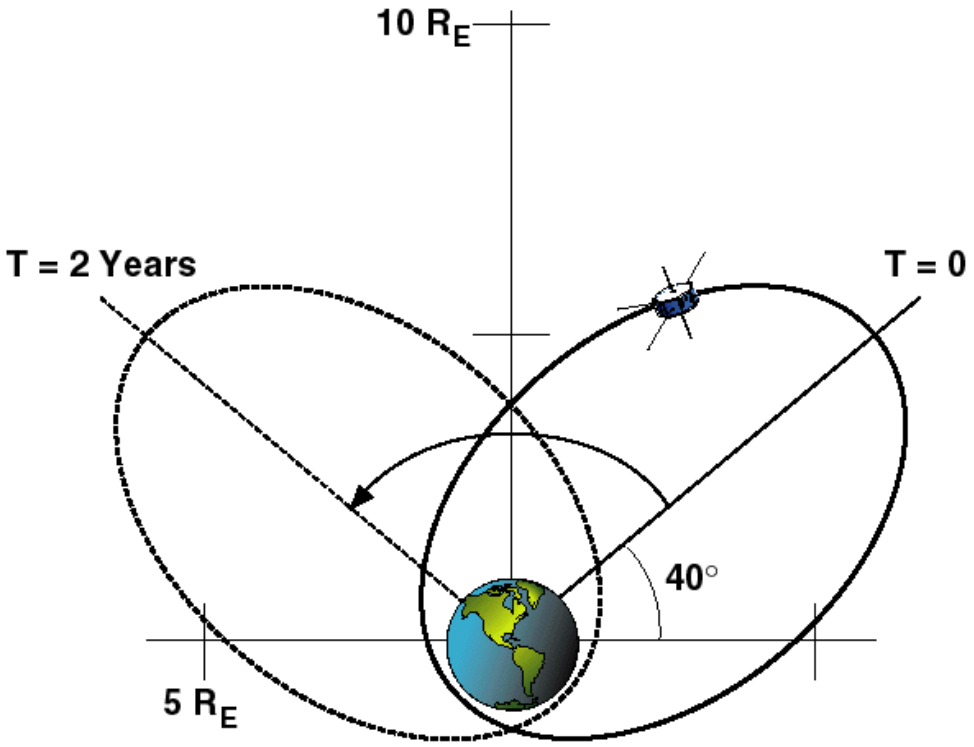

FIGURE 3.11: A schematic to show the precession of the IMAGE orbit for the first two years of its operation. The orbit has 90° inclination with 7 RE distances at apogee and 1000 km at perigee. Each orbit lasts 13.5 hours. (*Mende et al.*, 2000b; *Burch*, 2000)

to August 2002 - a period where the orbital apogee covers the northern pole.

The IMAGE Far-UltraViolet (FUV) Imager provided the data used here, and is composed of three separate instruments (*Mende et al.*, 2000a) but only two are relevant to this thesis:

- Wideband Imaging Camera (WIC)
- Spectrographic Imager (SI)

The Wideband Imaging Camera (WIC) and the Spectrographic Imager (SI) have 17° x 17° and 15° x 15° fields of view, covering an area of 13,300 x 13,300 and 11,700 x 11,700 km respectively at 7 R_E distance (*Mende et al.*, 2000b). WIC is used to

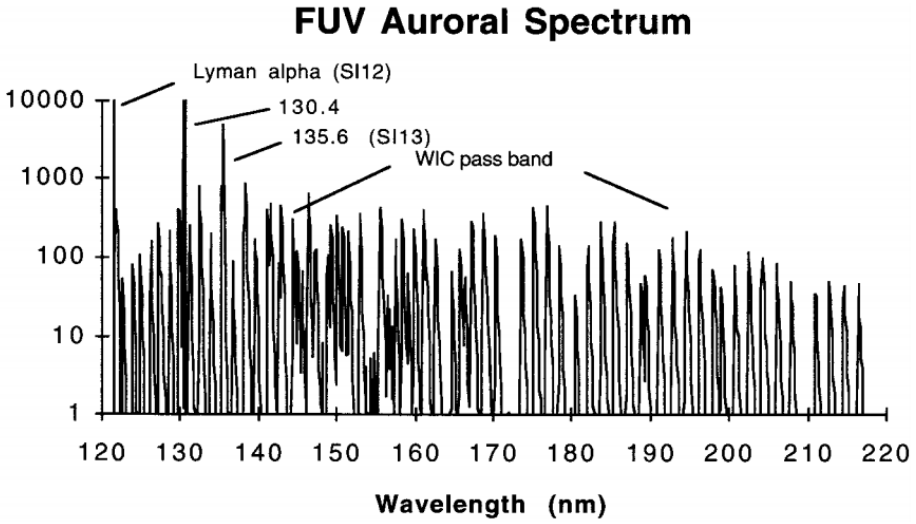

FIGURE 3.12: Taken from Figure 1 of *Mende et al.* (2000b) The spectral modelling of the ultraviolet auroral emissions and the geocorona. The model is typical nightside aurora with 10 kR intensity of OI 130.4 nm.

provide broadband UV images to give the maximum spatial and temporal resolution at each local time (*Mende et al.*, 2000a). The Spectrographic Imager is actually composed of two cameras (SI12 and SI13) and provides images of the aurora in two different wavelength bands. Figure 3.12 shows a typical modelled auroral spectrum for average nightside aurora (*Mende et al.*, 2000b) in the ultraviolet. As labelled the WIC and SI12 wavelengths are seen as 140-190 nm and 121.6 nm.

The Lyman Alpha line that SI12-+ images is produced by two different physical processes. The one observed by SI12 is the Doppler-shifted auroral hydrogen emission produced by energetic protons that precipitate into the atmosphere. As protons enter the atmosphere they are able to pick up an electron from the resident N_2, O_2 and O populations via the charge exchange process. This propels the protons into the excited Lyman-Alpha transition which spontaneously decays and the resultant radiation is observed by SI12. A good reason to include the SI12 proton aurora into analysis is due to it being less susceptible to contamination from dayglow. The dayglow emission is due to

incident solar radiation hitting the atmosphere producing an intense emission that can obscure the images taken by WIC and SI13. As the incident radiation is dependent on solar zenith angle, the subsolar point is the most affected and is particularly a problem during summer months.

Data from IMAGE are used in this thesis to provide a dataset of auroral boundaries extracted using the method described by *Longden et al.* (2010). Chapter 6 utilises this dataset to statistically compare their location to the derived SuperDARN ionospheric convection boundaries.

Chapter 4

Derivation of a new boundary determination technique (CCB) using SuperDARN global convection maps

This chapter describes a new technique to extract a boundary from SuperDARN global convection maps. The Convection Curvature Boundary (CCB) is a new technique that follows the location of maximum curvature across successive convection streamlines to determine locations that observe a significant change in their flow direction. This chapter will compare the CCB to the Convection Reversal Boundary (CRB) which is the boundary between sunward plasma flow over the pole and anti-sunward flow at auroral oval latitudes (*Ridley and Clauer*, 1996). As has been previously discussed this boundary is closely related to the OCB (*Sotirelis et al.*, 2005) and as such numerous studies have been conducted with a multitude of instruments to assess its behaviour and applicability as a proxy boundary e.g. (*Sotirelis et al.*, 2005, 2017; *Chen et al.*, 2015; *Koustov and Fiori*, 2016; *Bristow and Spaleta*, 2013). *Sotirelis et al.* (2005), *Bristow and Spaleta* (2013) and *Koustov and Fiori* (2016) in particular conducted statistical studies using SuperDARN data to extract a CRB. The easily observable sunward/anti-sunward

(eastward/westward) flow direction in the MLT-MLAT plane means it can be readily utilised using SuperDARN data for statistical studies where large quantities of data are required. The studies have shown that the CRB is easy to identify at dawn and dusk as flow predominantly traverses perpendicular to the magnetic longitude and so flow shear is significant. It is noted that the CRB can be difficult to discern near the noon/midnight sectors as flow travels more parallel to the magnetic longitude and so the change in flow direction is defined over a much larger latitude. *Koustov and Fiori* (2016) found that this can lead to discontinuities across the noon/midnight cell boundaries where the boundary jumps by several degrees latitude as shown in Figure 4.1. Part a) shows a monthly averaged SuperDARN map and b) the CRB found in hourly MLT bins for the dawn (red) and dusk (blue) cells. *Chen et al.* (2015) have also previously reported this effect as 'The Gap' and its prominence in the dayside is exacerbated by strong IMF B_y driving. The midnight region exhibits a similar discontinuity problem although its cause is attributed to the Harang Discontinuity (*Hubert et al.*, 2010).

The discontinuities or unreliable boundaries in the noon/midnight region from the CRB are significant as these regions are linked to magnetospheric processes such as magnetic reconnection or substorms i.e. key areas of interest. A new boundary technique that can be readily utilised and is more well defined in the noon/midnight regions could help to 'close the gap' and provide a more accurate representation of the polar cap area, particularly in statistical studies. The new boundary extraction technique is based on observing a significant relative change in velocity direction. If the more traditional CRB is determined by an exact definition of 'reversal' then there may be times when this does not give the most appropriate solution. Use of a softer threshold whereby we identify

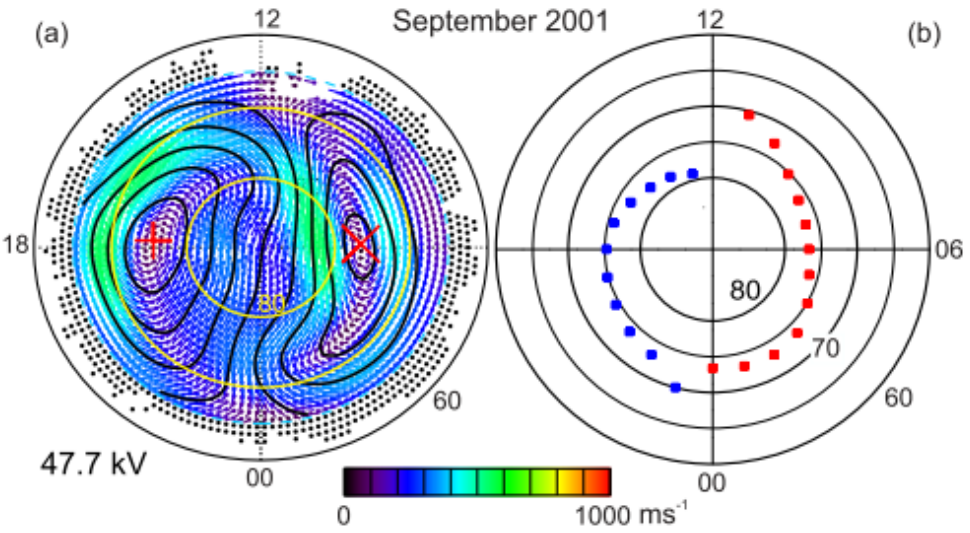

FIGURE 4.1: Taken from Figure 2 *Koustov and Fiori* (2016) Convection pattern in the MLT-MLAT coordinates inferred from the September 2001 SuperDARN grid velocity data set. Every dot represents the origin of a plasma velocity vector with the length coded by colour. Overlaid are contours of the equal electric potential (that are 6 kV apart). Potential difference between the foci of the large-scale convection cells is 47.7 kV. (b) The convection reversal boundary location inferred from the data presented in panel (a) for dusk (blue dots) and dawn (red dots).

the most significant velocity direction change from one region to another, but with no requirement that the direction 'reverses' may help to draw out boundaries that do not qualify as a CRB. A justification for using a significant velocity direction change from one convection region to another (determined by appropriate threshold considerations) is that these changes indicate that a force has been exerted on the plasma and hence the frozen-in magnetic flux. This, in turn, implies the presense of field aligned currents (FACs) which couple to the magnetosphere and are therefore likely to be associated with magnetospheric processes. For example, magnetic reconnection will result in tension forces that act on newly opened field lines and cause noticeable directional changes in $\vec{E} \times \vec{B}$ velocity. (*Dungey*, 1961)

This thesis uses data from the SuperDARN ECLAT dataset (*Milan et al.*) detailed in Chapter 3. Utilising the SuperDARN ECLAT dataset limits the variability in the

convection maps due to fitting constraints and gives a standard set of maps that can be easily accessed by others. The following sections quantify how a SuperDARN boundary can be extracted using an alternate velocity direction change threshold. To clarify the strengths and weaknesses of the new SuperDARN boundary method it must be compared to other standard techniques, in future chapters these will be global auroral images and the CRB; an alternative boundary extracted using SuperDARN. These datasets are both averaged in latitudinal profiles of 1 hour MLT and 1° magnetic latitude and so this same averaging will be used for the CCB technique to ensure consistency and easy comparison between all datasets.

4.1 Convection curvature boundary (CCB) - A test case

The clearest way to outline this method will be to use an example; Figure 4.2 shows a SuperDARN convection map for 22 December 2000, 07:14 UT. This date is chosen somewhat arbitrarily although it was ensured that the time period exhibits a relatively high amount of radar backscatter and there exists corresponding IMAGE data so direct comparisons with global auroral data are possible. In addition, a period was chosen during which the IMF conditions were predominantly southward. Extraction of the CCB using this technique is only valid for negative IMF B_z conditions producing generally clear two-cell convection patterns. This technique has been developed as a proxy for the polar cap area, but it is not applicable in the presence of additional cells as are often generated with a positive B_z IMF component (*Reiff and Burch*, 1985).

The map in figure 4.2 shows a clear dawn and dusk cell which are outlined by dashed and solid black equipotential lines starting at -3/+3 kV respectively and incrementing every

6 kV until a minimum/maximum is reached. These lines can be viewed as 'contours' and in the first instance Cartesian location information is gathered for a single contour line.

4.1.1 Regridding the map potential data

The standard presentation of the map potential data in a SuperDARN map is shown in figure 4.3a-b. The data is gridded in bins of 2° magnetic longitude and 1° magnetic latitude as shown by figure 4.3a, note the gridding stops at the minimum latitude of the Heppner-Maynard boundary, 61°. The electric potential as found by the map potential method outlined in Section 3 is resolved to this resolution and shown in figure 4.3b for the test period 22 December 2000 07:14 - 07:16 UT. The SuperDARN global convection map

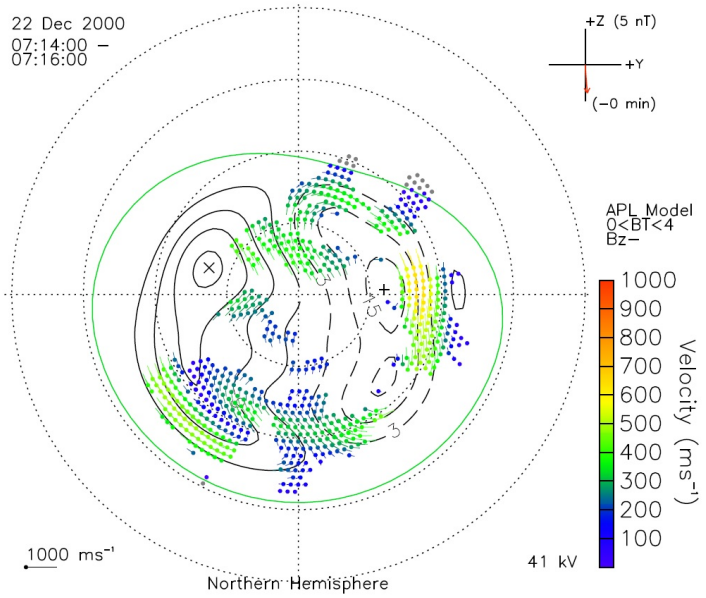

FIGURE 4.2: A two minute SuperDARN global convection map is shown for 22/10/2000, 07:14 - 07:16 UT. Velocity vectors and flow streamlines derived from the 'map potential' technique (Chapter 3) are shown on a geomagnetic grid representing the northern hemisphere. The Heppner-Maynard boundary is shown by the green distorted circle, with the polar cap potential V_{PC} in the bottom right hand corner and the IMF clock angle direction on a Y/Z plane grid in the top right hand corner.

overlays the lines, or contours, of constant electric potential (equipotentials) at regular 6 kV intervals as shown in figure 4.2. These contours are calculated from the electric potential data stored in the 2° magnetic longitude and 1° magnetic latitude bins and define the characteristic shapes of the dawn and dusk cells giving a visual representation of the convection velocity streamlines.

The first step is to generate a set of coordinates that define the equipotential lines. Ultimately the goal will be to isolate the locations on each individual contour where there is significant curvature. As the electric potential data for each map is already stored in a rectangular array of magnetic longitude and latitude a first idea was to use this polar coordinate system and make use of the IDL **CONTOUR** function to generate the set of coordinates at integer kV contours.

Figure 4.4 shows the resultant equipotentials for ± 3/4/5/6 kV in polar coordinates. This highlights the problem with using this system, in that there will always be a boundary at 0° magnetic longitude. This boundary introduces discontinuities, for example in this figure the positive equipotentials (red lines) are split to either side of the grid. The IDL contour function nicely provides the set of coordinates that defines all 'closed', circular, and 'open' equipotentials but this discontinuity can make it difficult to define the full 'closed' equipotential especially when there are multiple cells present. In addition as the magnetic latitude tends towards 90° the gridded 2° magnetic longitude and 1° magnetic latitude bins become smaller in area, leading to a distorted projection. As a result further discontinuities can be introduced, close to 90°, as can be seen on the blue negative equipotentials (blue lines) in figure 4.4.

To combat the problems introduced by working in a polar coordinate system, cartersian

FIGURE 4.3: Three polar plots for the test period 22/12/2000 07:14 with the magnetic pole located at the centre, noon to the top and dusk local times to the left. The circular dots outline 10° latitude from the magnetic pole. a) the standard SuperDARN map potential gridding resolution in 2° magnetic longitude and 1° magnetic latitude. The gridding stops at the minimum latitude of the Heppner-Maynard boundary. b) The potential magnitudes in each standard bin size on a scale from -24kV to 19kV. Blue representing negative potential and red positive potential. c) The re-gridded potential magnitudes where the new bin size is [0.1,0.1] in Cartesian coordinates.

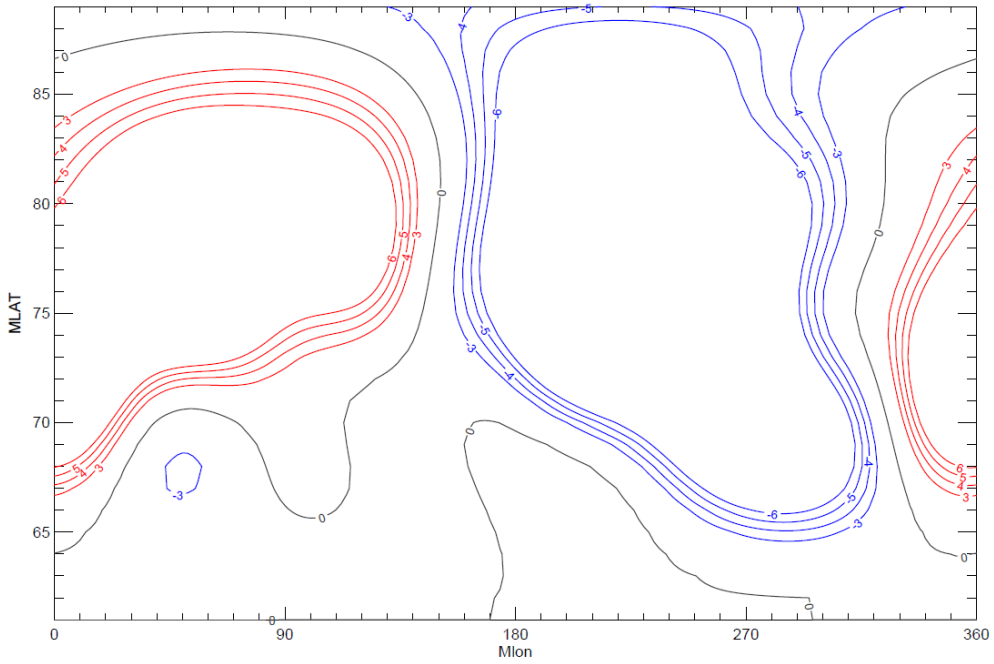

FIGURE 4.4: ± 3/4/5/6 kV equipotentials plotted within a rectangular array of magnetic longitude and latitude. The red lines represent positive electric potential (dawn cell) and the blue lines the negative electric potential (dusk cell).

coordinates are used instead. To do this the SuperDARN map and electric potential data is transformed into cartesian by utilising the IDL **POLAR_SURFACE** function and is linearly interpolated to give a map [X,Y] resolution of [0.1,0.1]. The choice of [0.1,0.1] was made somewhat arbitrarily although as stated a finer resolution was desirable. Figure 4.3c shows the result of interpolation and finer resolution plotted in geomagnetic coordinates for comparison to (b) and (c). It is analogous to (b) but shows smoothed out potential magnitudes as would be expected from the interpolation.

Figure 4.5 shows the result if the ± 3/4/5/6 equipotentials are plotted in the Cartesian coordinate system, after the regridding and interpolation of the electric potential has been applied. The dawn and dusk cells are now more clearly defined and show as 'closed' equipotentials meaning the set of coordinates defining each contour location can be easily extracted. The next section will cover this in more detail.

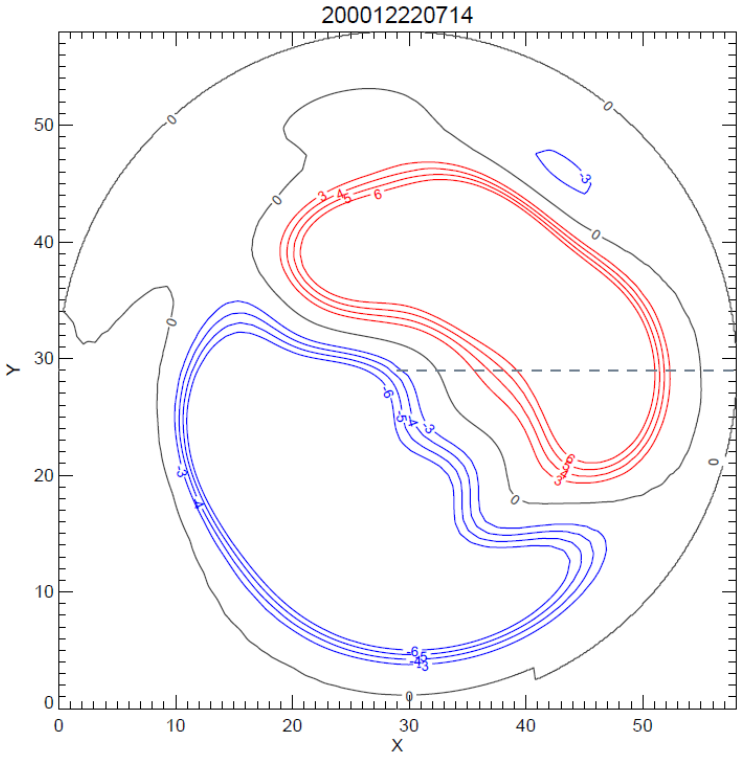

FIGURE 4.5: ± 3/4/5/6 kV equipotentials plotted in a Cartesian coordinate system. The red lines represent positive electric potential (dawn cell) and the blue lines the negative electric potential (dusk cell). The grey dashed line shows the location of the 0° magnetic longitude.

4.1.2 Equipotential contour [x,y] path extraction

The set of cartesian points for each equipotential contour, beginning at -3kV to the minimum potential and +3 kV to the maximum potential in increments of 1 kV, is found. During the development of the CCB it was observed that below |3| kV the contours were much more likely to follow unphysical shapes and create large kinks as a result of the map potential fitting routine. Potential magnitudes above |3| kV were more stable and so this was used as a minimum threshold to extract the CCB. The resulting contour [x,y] path information is a series of irregularly spaced points, the spacing of which is a direct function of the [0.1,0.1] grid resolution. The **CONTOUR** function is able to provide

the coordinates of any equipotential magnitude, however this can sometimes mean there are multiple options to choose from. In order to define the set of equipotentials for a given map (providing the B_z condition is satisfied) an automated procedure was used and the following criteria were applied:

- Only one equipotential contour for any given magnitude is used in analysis. In the case that there are multiple cells present, the largest contour in length will be selected.

Additional cells, particularly on the order of a few kilovolts, are a common feature of many SuperDARN maps. As this analysis is valid for southward IMF driven convection, potential values close to zero should be associated with the largest contours on the map, outlining both the dawn and dusk 'Dungey-type' cells. This is the main justification to neglect any additional smaller contours at a given potential magnitude.

- A given equipotential contour must contain at least 10 [x,y] points to constrain its location.

Eventually the set of points that define the equipotential contour will be processed in order to quantify the degree of curvature between points. Therefore it is necessary to only use contours that contain enough [x,y] points to successfully compute the curvature (this is covered in more detail in section 4.14). Observations throughout the testing phase showed that 10 points was sufficient enough to extract a meaningful curvature boundary.

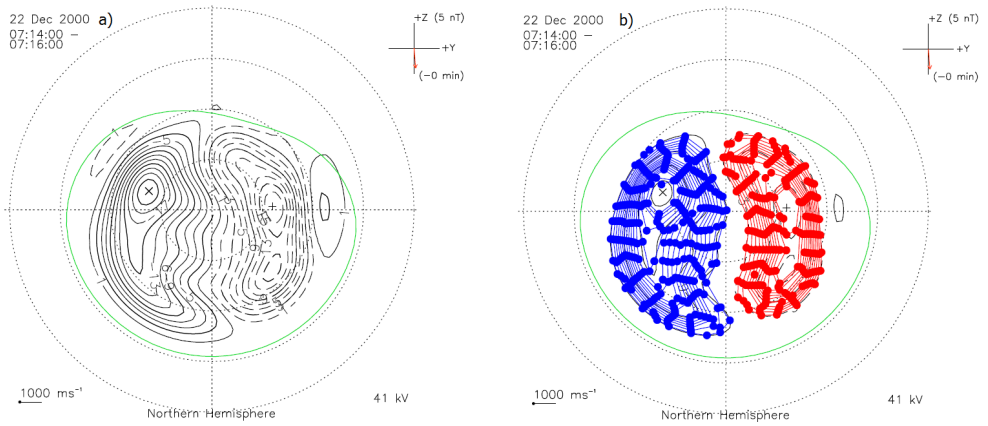

FIGURE 4.6: Two polar plots to show a) the 2-minute SuperDARN map with equipotential contours plotted every 2kV to the minimum/maximum. b) The result of the regridding/extraction and averaging (in 5° [x,y] latitude bins) for each applicable equipotential contour for the test-period. The red dots represent points on the dawn cell (positive potential) and blue on the dusk cell (negative potential).

- The minimum (maximum) equipotential contour extracted from the map is always 4 kV in magnitude higher (lower) than map potential minimum (maximum).

It is also common for SuperDARN maps to present additional cells around the foci of the maximum and minimum potentials. At these values it is not always clear which to select as they are typically on the same order of contour length. The automated routine does not have the scope to include two contours of the same magnitude and so to avoid any confusion these potential magnitudes are avoided.

Figure 4.6a shows the test example SuperDARN map with equipotential contours every 2kVs shown. This plot is shown as a reference to 4.6b where the extracted equipotental contour locations are overplotted. Note the figure has contours plotted only every 2kV for clarity, but the routine will extract a Cartesian location every 1kV.

4.1.3 Latitudinal averaging resolution of a countour

The set of [x,y] coordinates that define the equipotential contour location are provided by the IDL **CONTOUR** function and the number of coordinates provided is related to the resolution of the initial [0.1,0.1] gridding. This fine resolution can cause some problems as occasionally the distances between consecutive points approach zero. Distances that converge to zero will lead to infinitely large derivatives which is problematic as the curvature boundary technique is based on curvature per unit distance. These will create artificially large curvature values that have no physical meaning. The initial choice of gridding to [0.1,0.1] was somewhat arbitrary. It was not known a-priori what the best resolution would be and so a decision was made to create a fine grid that could be later averaged into a desired resolution which could then be tested to find the most appropriate. This section describes how the set of [x,y] coordinates defining each contour is averaged into a chosen resolution.

An illustration of how the latitudinal averaging takes place is shown in figure 4.7. The cartesian system used to hold the SuperDARN electric potential data for a given map can be seen in figure 4.5. From this figure it can be seen that an increment in the X or Y direction is equivalent to latitude. When this section refers to latitudinal averaging it can be equivalently thought of as averaging in a grid of specified size in X or Y. The square grid cells in this illustration represent 'latitude' bins of an arbitrary size. The series of blue dots represent the unprocessed [x,y] coordinates of an equipotential contour. It appears as a solid blue line as the spacing between points is too small to be seen. The averaging takes place in each square grid cell, where the mean XY position of all [x,y] contour points is computed, this is shown overlaid as the red dot. It can be seen that

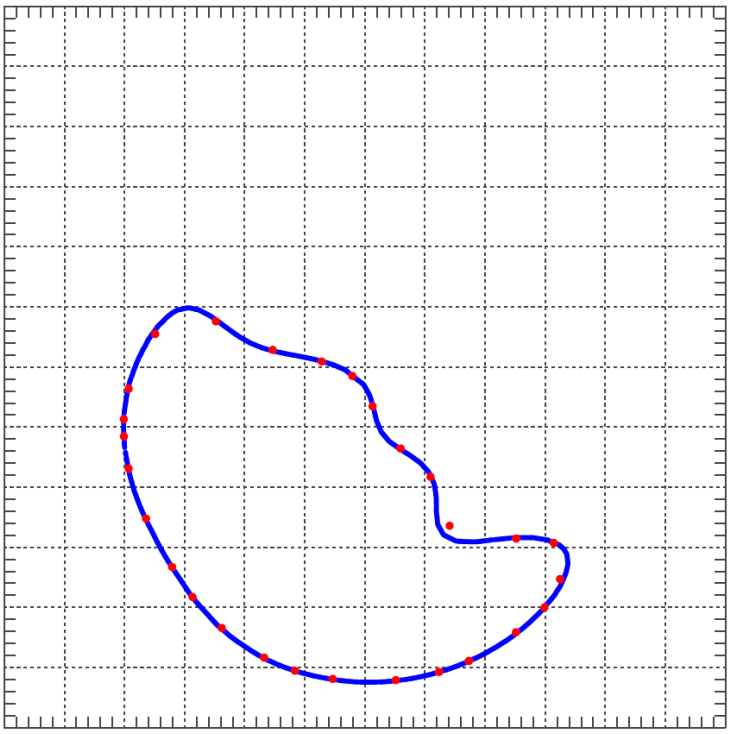

FIGURE 4.7: An illustration of the 'latitudinal' averaging for an arbitrary grid size. The blue dots represent the unprocessed [x,y] coordinates of an equipotential contour and the red dot the average of each of these points in each square cell.

it is possible for this average position to lie away from the set of original [x,y] points. This is common where there is a strong degree of curvature in a given grid cell, this averaging will therefore act to decrease curvature if too large a bin size is used. It should be noted that this averaging method does not lead to equally spaced [x,y] points along the contour but it does have the effect of smoothing them to a resolution that prevents spacing between points from converging to zero.

4.1.4 Quantifying the curvature of the countour

The final processing step is to calculate the degree of curvature at each [x,y] coordinate of equipotential contour line. How 'curved' a given coordinate is will depend on the vectors

between consecutive points and the following method aims to quantify how much a vector direction changes between them.

Figure 4.8 is an illustrative example of how the curvature at each point is extracted. Vectors $\vec{V_n}$ are drawn between points on the contours, and the angle between vectors, θ_n, calculated from the dot product:

$$\theta_n = acos \frac{\vec{V_n} \cdot \vec{V_{n+1}}}{(|\vec{V_n}||\vec{V_{n+1}}|)} \tag{4.1}$$

(a) illustrates a case where the lengths of adjacent vectors are equal. Here it is clear that the curvature is greater where the angle is greater.

(b) illustrates a case where the angles between vectors are equal. Here it is clear that the curvature is greater where the vector lengths are shorter.

We therefore define the 'convection curvature' (CC) as:

$$CC = \frac{\theta_n}{|\vec{V_n}|} \tag{4.2}$$

Two methods for extracting a peak curvature were tested. The CC calculates the change in direction per unit length, thus giving to significance to direction changes that occur over shorter distances.

A second method was also tested, whereby the CC as defined by equation 4.2 was computed and then the difference in curvature (CC^*) between $\theta_n/|\vec{V_n}|$ and $\theta_{n+1}/|\vec{V_{n+1}}|$ was determined. The idea behind this method was that it could identify areas where the curvature deviates significantly from the previous value. For example, if we have n vectors that follow the trajectory of a circle, the CC value computed at each point

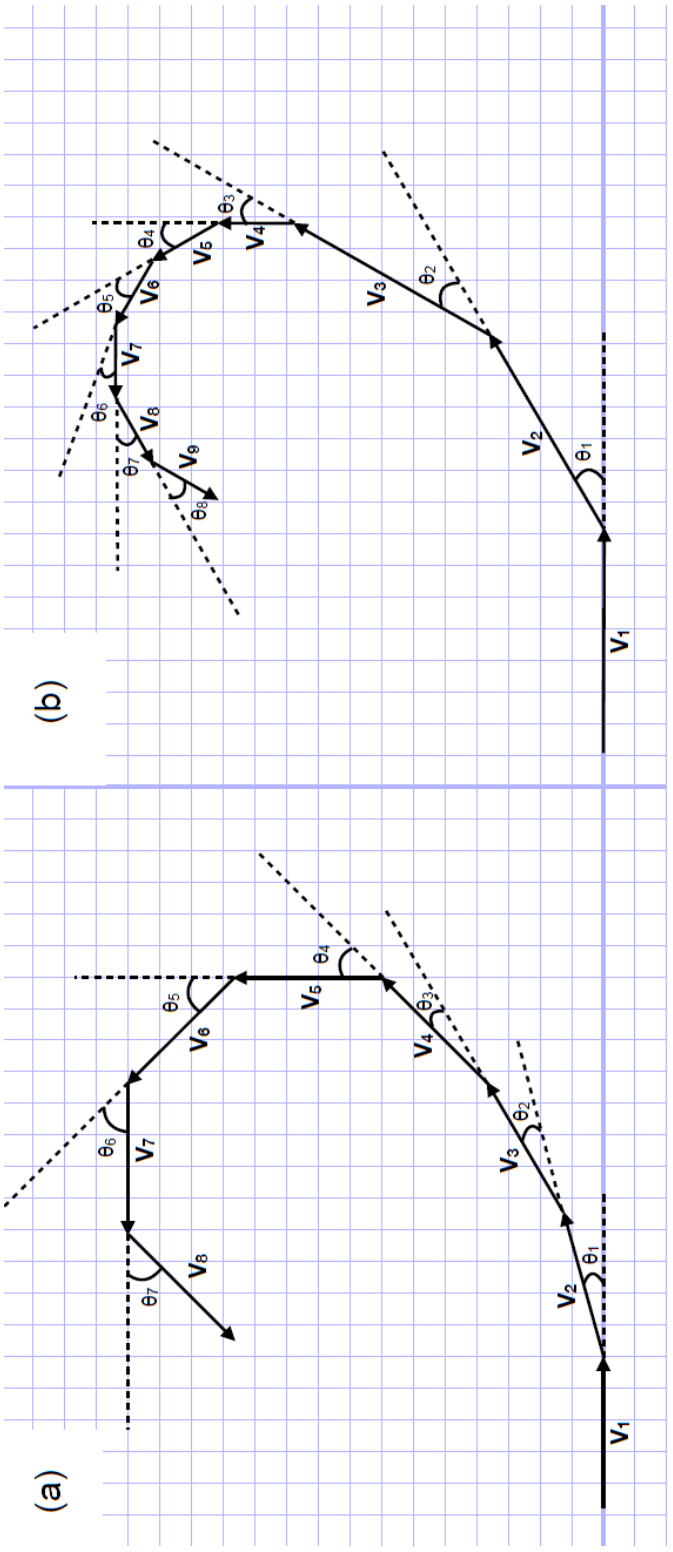

FIGURE 4.8: An illustration to show vectors $\vec{V}_n$ drawn between points on the contours, and the angle between vectors, θ_n.

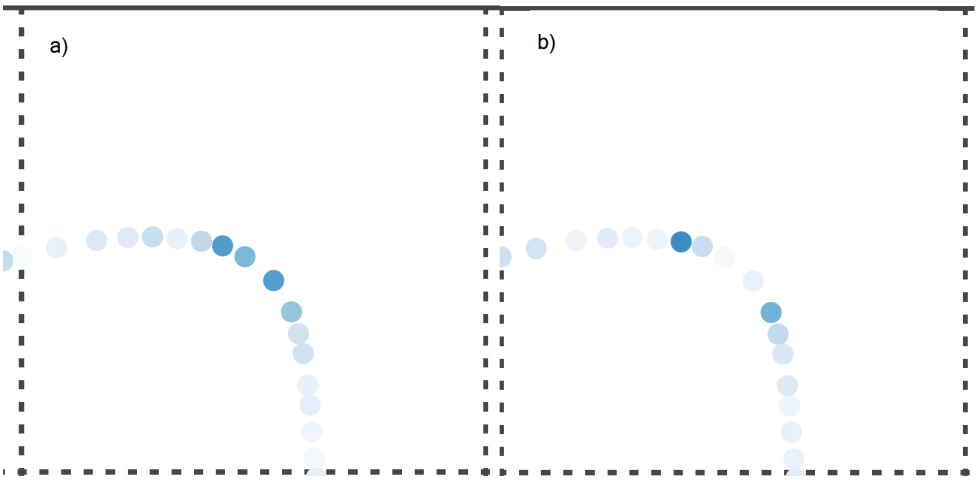

FIGURE 4.9: The locations of a selection of points extracted from the -3kV contour line for the test case period. The colours of the dots range from white to dark blue. The darker colour corresponds to higher values of a) the CC value computed with $\theta_n/|\vec{V_n}|$ and b) the CC^* computed with $\theta_{n+1}/|\vec{V_{n+1}}|$

.

would theoretically be the same as the angle does not change. The difference in CC values across this hypothetical circle would give a value of 0. Now, if the circle becomes deformed in some way the regions where the deformation starts to happen would be identified by the quantity CC^*. When applied to the typical ionospheric convection pattern it had been hoped that this quantity would better capture the location where a force is applied to the plasma (e.g. from magnetic reconnection).

Figure 4.9 shows the difference between the two techniques by showing the location of a subset of points that were extracted from the -3kV contour line for the test case period. The colours of the dots range from white to dark blue. The darker colour corresponds to higher values of a) the computed CC b) the computed CC^*. For Figure 4.9a the darker colours are clearly constrained to the region where there is the highest bend along a trace of the points. However, in Figure 4.9b there are now two distinct regions of darker blue that occur on either side of the 'bend'. This was a common feature of using the CC^*

and was problematic as now each curve in the data had two associated locations. It was decided that because the resolution was so small the latitudinal difference between each technique was negligible, it made more sense to use the CC value centred on the highest region of curvature.

4.2 Determining the latitudinal averaging resolution of a contour

Ultimately the resolution needed for analysis must be able to capture subtle curvature. Figure 4.10 shows the results of applying different latitudinal averaging resolutions of 0.25°, 0.5°, 0.75° and 1° as described in section 4.1.3. The dusk cell uses a blue colour scale and the dawn cell a red colour scale. Each individual equipotential line used in the analysis uses its own scaling from white to either dark blue or red. White is the minimum curvature value along that contour and the darkest colour the largest. This relative scale draws the eye to regions on each individual contour line where the regions of highest curvature occur. If a scale relative to the entire map was used, the rarer high curvature values shift the colour scaling such that areas with smaller curvature are unable to be distinguished. As an initial check the relative contour colour scale grading offers a way to visualise how the algorithm responded to changes in grid size and different regions of flow shear.

In all four plots regions with clear flow shear observe a high curvature as shown by the darker colouration. It is most obvious in the nightside dusk region where the dusk cell extends past midnight. More subtle areas of flow shear occur in the dusk cell as the

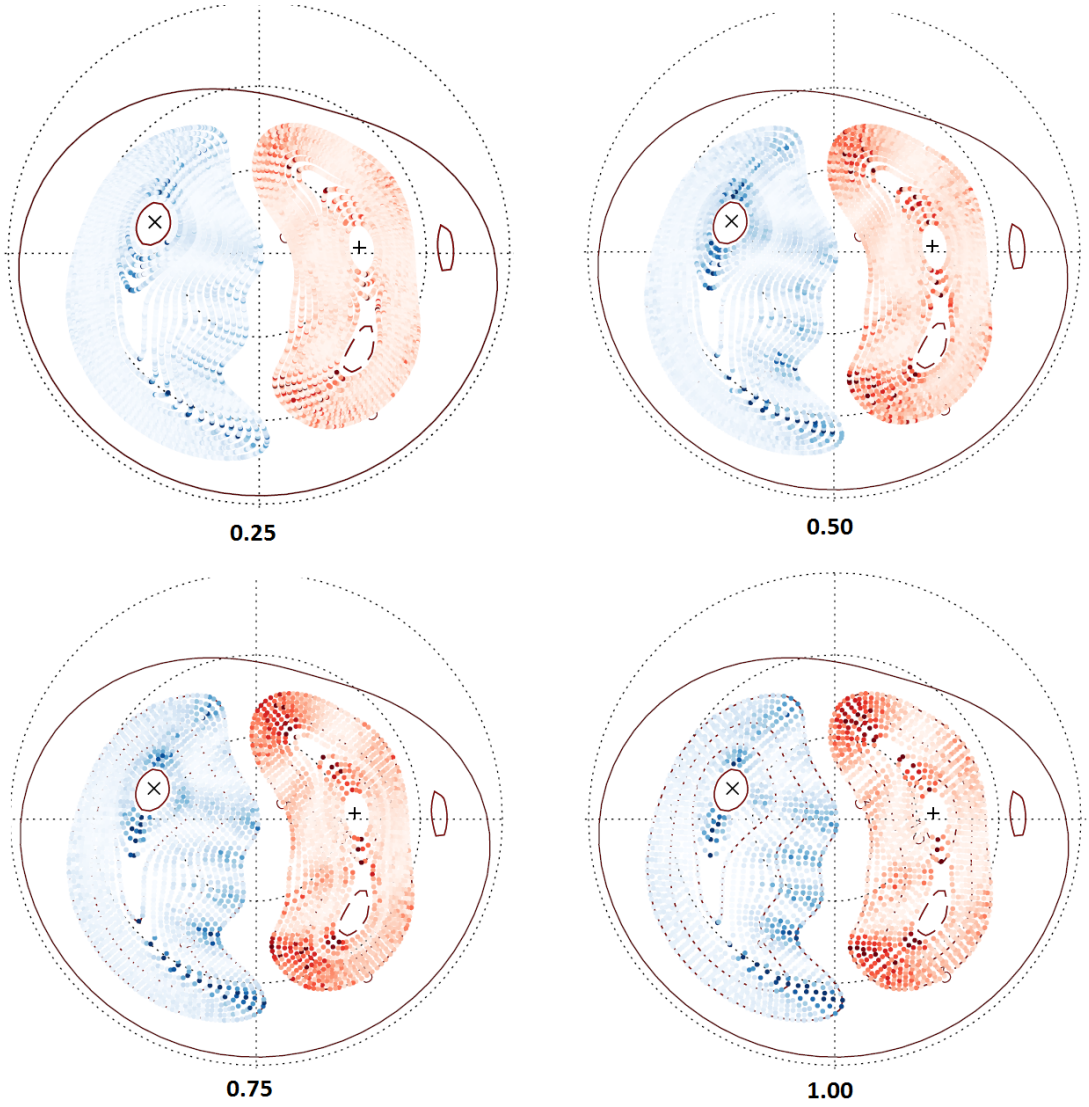

FIGURE 4.10: Four plots in geomagnetic coordinates where the magnetic pole is located in the centre, noon MLT is to the top and dusk to the left. The circular dots represent the 10° latitude bands from the pole and the solid black line shows the Heppner-Maynard boundary for 22/12/2000 07:14/ [x,y] points extracted for each equipotential contour are plotted in four different bin sizes [0.25, 0.50, 0.75, 1.00]. The colour scale in each cell is graded to each individual equipotential contour line, with white being the lowest curvature value and dark blue/ dark red the highest on that line.

convective flow traverses the polar cap as a series of 'wavy' like flows. Other regions such as the dayside dawn and dusk cells, and the nightside dawn cell also show flow shear as identified by higher CC values indicated by darker colouration, although in these regions this is spread over a wider latitudinal area.

The 0.25° gridding resolution shows the most muted colouration of all the four plots with large regions of light blue and red shown across the map. This indicates that the highest values of curvature are much greater than the map average. Even so regions of flow shear as identified in alternate map resolutions in Figure 4.10 are evident with some level of colouration. It is also noted that there are dark spots observed in suspect regions, for example on the lower latitude dawn cell at approximately 3MLT. There are two darker red spots visible with no corresponding curvature, upon closer inspection it was found that in these areas the distance between consecutive vertices approached zero causing artificially large values of curvature. The 0.5° resolution map shows a deeper level of colour as a whole and areas of flow shear are more clearly identified. However, at this resolution there is still evidence of artificially large curvature values in similar regions to the 0.25° case. The 0.75° and 1° gridding resolutions continue to observe darker colouration in regions of flow shear effectively marking these areas of significant curvature in the flow and gaps between consecutive points become increasing more visible.

The 0.75° latitude bin was selected for analysis as it offered a spatial resolution that gave the best compromise between constraining the latitude of the flow shear region as needed for a boundary and avoiding suspect values of curvature as evidenced at the smaller gridding resolution.

4.3 CCB Boundary threshold values

Visual inspection of Figure 4.10 reveals a boundary shape is evident from the Super-DARN map but other areas of flow shear are also visible, for example, in the flow over

the polar cap. One intended use of this technique is to provide a proxy for the open-closed field line boundary and as such some justification is necessary to determine values of the curvature associated with 'significant' regions of flow shear. Analogous proxy OCB boundary techniques (*Longden et al.*, 2010; *Bristow and Spaleta*, 2013) utilise one hour of MLT/1° latitude averaging bins and this will also form the basis of a boundary extraction using this method.

After the processing steps outlined in section 4.1 are followed to extract CC values for each SuperDARN map they are averaged in 1 hour MLT/1° MLAT bins. Due to the large time-spans involved in the study an automated routine is written to extract a meaningful automated boundary from the latitudinal profiles. As this technique involves determining what is meant by a 'significant' change in direction along an equipotential line some justification must be given for threshold values used.

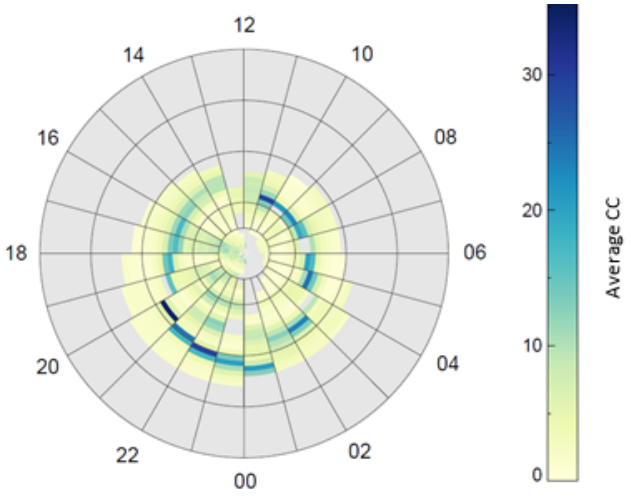

FIGURE 4.11: A grid shown in geomagnetic coordinates with the magnetic pole in the centre and magnetic local times labelled with 12 MLT at the top. The grid is split into 1 hour MLT, 1° magnetic latitude bins. All curvature values for 22/12/2000 07:14 are extracted using the described method (see Figure 4.10 C). These values are averaged in 1 hour MLT/1° MLAT and the resulting magnitudes are plotted onto the grid. The colour scale reads from yellow to dark blue representing the maximum averaged curvature value for the whole map

Figure 4.11 shows the result of processing the SuperDARN test case map to find the CC values and averaging in 1 hour MLT and 1° MLAT bins. The colour scales from light yellow to dark blue with the dark blue corresponding to areas of high curvature and thus flow shear. A roughly oval boundary structure is evident globally and there appears to be latitudinally confined regions of high curvature for each MLT bin.

To identify a boundary in the CC data at each MLT, we consider the latitude profiles of the averaged curvature. A set of examples are shown in Figure 4.12 for four different magnetic local times (1-2,7-8,12-13,22-23 MLT). The red stars on certain points reference local maxima and the blue local minima. As a first attempt to elucidate appropriate threshold information all latitudes along an MLT line corresponding to local maxima were recorded and their distributions plotted for the three-month period. This revealed large occurrences of local maxima over all magnetic latitudes but particularly over 80°. As such it was not possible to determine appropriate threshold values as there was no discernible pattern to the distribution. *Pettigrew et al.* (2010) derived climatological patterns for the high latitude convection given a range of IMF conditions. Climatologically in all instances with a negative IMF B_z component, the size of convection is such that flow at 80° MLAT and above could be attributed to polar cap flows. This suggests that by using all local peaks contamination from cross polar cap flow is affecting the ability to extract meaningful threshold information. It should be noted that at this stage no threshold conditions were applied, and even very small maxima peaks are included.

Figure 4.13 shows the distribution of the absolute value of the CC from all local maxima across all hours of MLT. The 0.1, 0.25, 0.5, 0.75 and 0.9 percentiles are shown as grey dashed lines. Figure 4.14 shows the same distributions but split up into two latitude

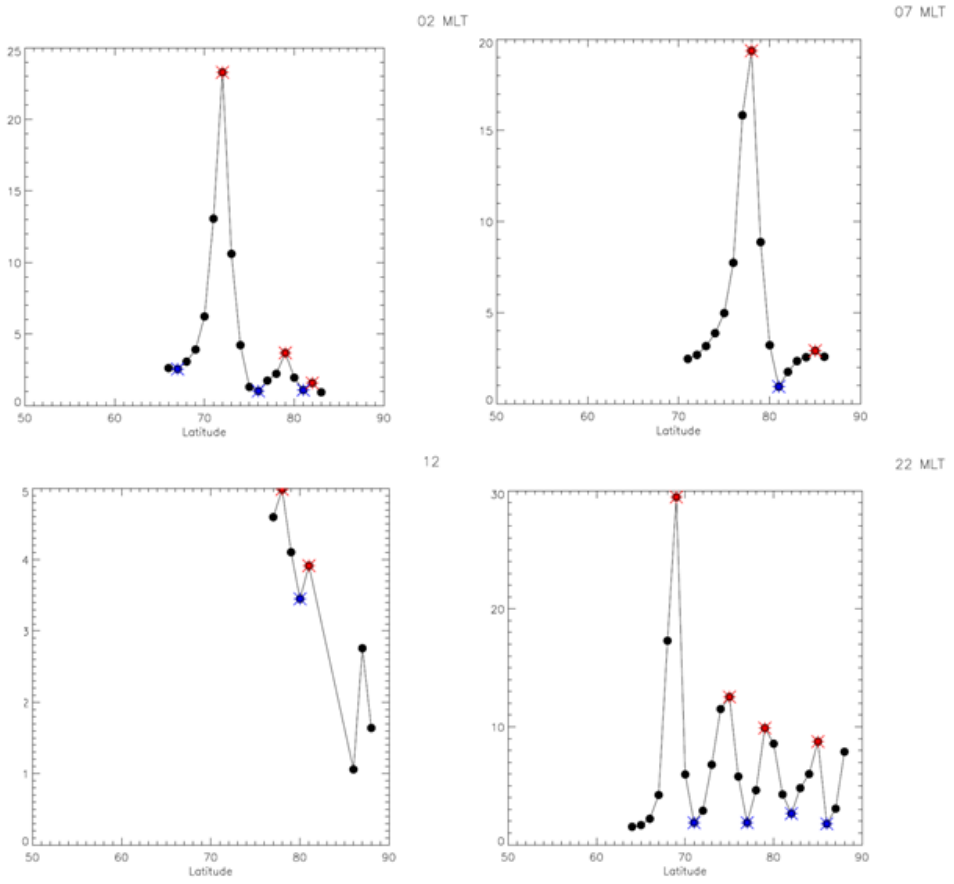

FIGURE 4.12: The averaged curvature values for four MLT segments [01-02, 07-08, 12-13, 22-23 MLT] from Figure 4.11 plotted against latitude. The red star highlights local maxima and a blue star local minima.

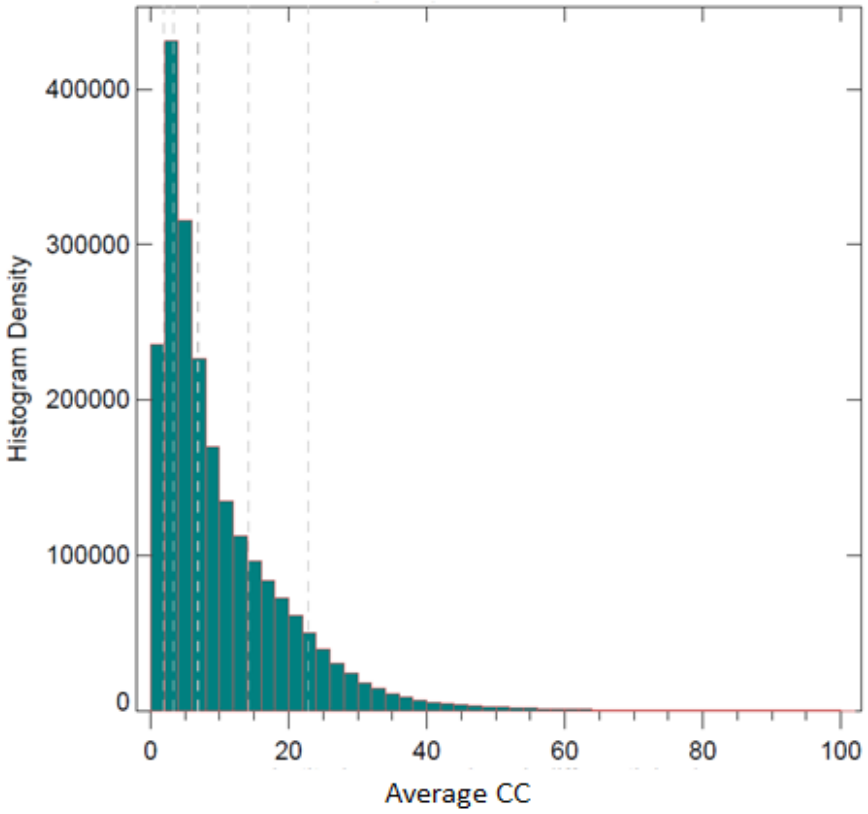

FIGURE 4.13: The distribution of all curvature values for each SuperDARN map in the time period December 2000- February 2001. The dashed grey lines represent the 0.1, 0.25, 0.5, 0.75 and 0.9 percentiles and corresponding distribution information is located in table 4.1

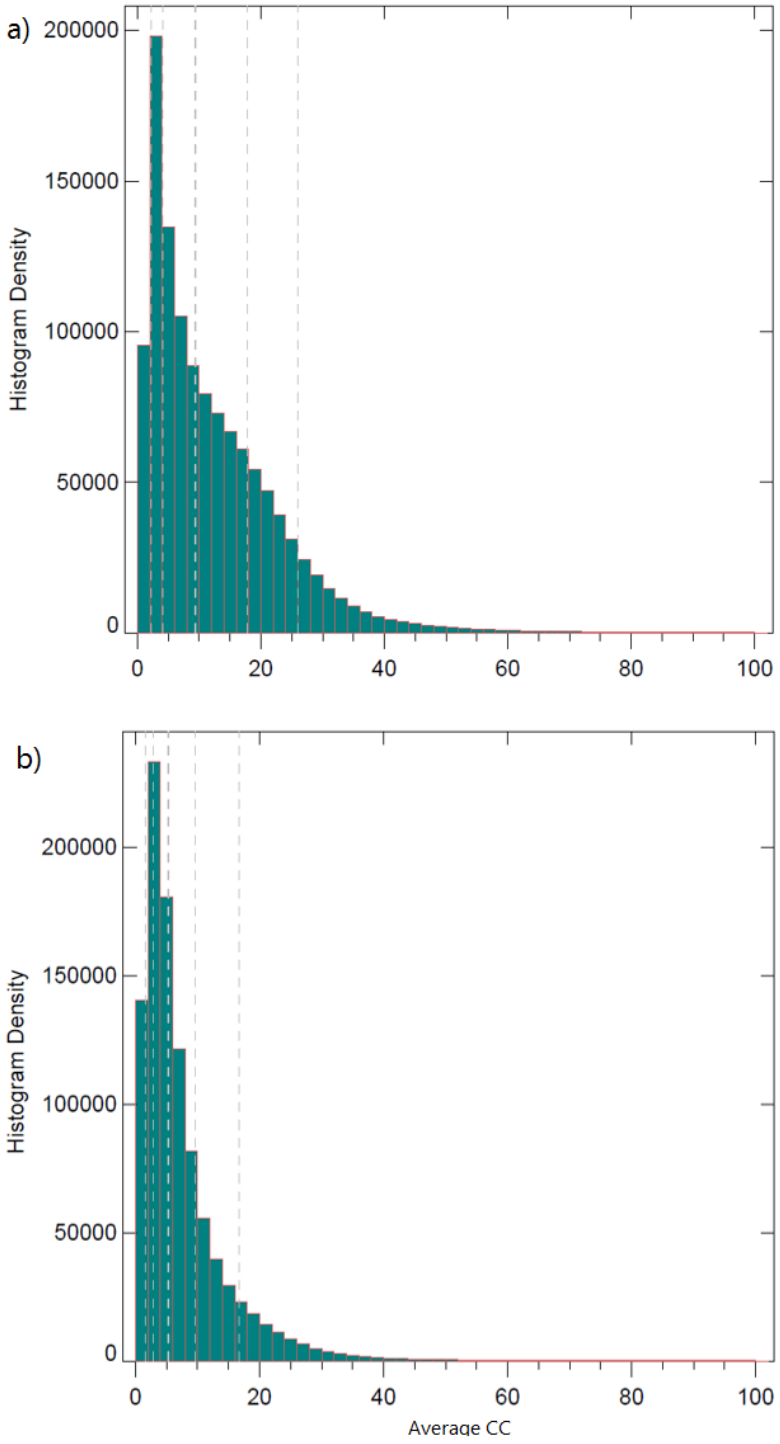

FIGURE 4.14: The distribution of all curvature values for each SuperDARN map in the time period December 2000- February 2001 for A) all latitudes below 80° MLAT and B) all latitudes 80° MLAT and above. The dashed grey lines represent the 0.1, 0.25, 0.5, 0.75 and 0.9 percentiles and corresponding distribution information is located in table 4.1

bands, one over 80° and one under 80°. Table 4.1 shows some common statistical parameters to describe the distributions presented in Figures 4.13 and 4.14. 45% of the average CC values come from over 80° MLAT, in this region the mean is lower (8.59) than for the under 80° region. In addition its skew is significantly higher which, when looking at Figure 4.14b shows that the values are concentrated on lower CC values. The Interquartile Range (IQR) shows a large difference between the two latitude populations 6.68 ($< 80°$ MLAT) compared to the much broader 13.68 for the $\geq 80°$ MLAT case.

TABLE 4.1: Common statistical parameters that describe the distributions presented in Figures 4.13 and 4.14. The data comprises of the total number of average CC values, their mean, standard deviation and skew. The [0.1,0.25,0.5,0.75,0.95] percentiles are shown in rows 5-9. Column 1 is the corresponding data to Figure 4.13 and columns 2 and 3 correspond to Figures 4.14a and 4.14b respectively.

-	ALL	$< 80°$ MLAT	$\geq 80°$ MLAT
Total N	2,183,296	1,192,951	990,345
Mean	10.33	12.48	7.75
Standard Dev.	10.68	11.71	8.59
Skew	4.66	4.09	6.44
0.1	1.92	2.21	1.64
0.25	3.38	4.06	2.89
0.5	6.88	9.39	5.26
0.75	14.20	17.74	9.57
0.95	22.86	26.99	16.72

The latitude split attempts to isolate curvature values that are associated with flow shears occurring at higher latitudes over the polar cap. There are some obvious differences between the two distributions in Figure 4.14; for latitudes under 80° there is a broader distribution showing that it is more typical for lower latitude flows to exhibit higher areas of flow shear. This is not unexpected as from inspection of the typical convection patterns shown by statistical averages and case studies, the flows in the polar cap for southward IMF are generally directed anti-sunward, albeit with some wavy motion as noted in section 4.2

A threshold of 5.26 on the absolute value of the average curvature is chosen as significant, corresponding to the 0.5th percentile of values over 80° MLAT. This acts to remove half of the data in the higher latitude region most likely associated with polar cap flow and to filter out insignificant flow shear in the lower latitude region. If the 5.26 threshold is applied 40.2% of all the peaks found in the three-month period (contributing to Figure 4.13) are removed. In addition, a second parameter was used to determine clear flow shear, i.e. areas that exhibited a significant drop in average curvature value after a local maximum is observed. This parameter is the 'peak to trough height' i.e. the difference in average curvature from a local maximum and the next local minimum or the difference between a red point and next corresponding blue point shown in Figure 4.12. If analogous plots to Figures 4.13 and 4.14 are plotted they are found to follow a similar relationship and thus a threshold value is obtained from the same reasoning as with the absolute value of CC. This corresponds to a peak to trough height of 3.82 and is applied to the dataset in addition to the absolute value. When both thresholds are applied it leads to a reduction in data of 52% of the original dataset.

4.4 Summary

A new technique to extract a boundary from SuperDARN global convection maps is presented as an alternative to the CRB. The Cartesian location of each equipotential is extracted for a given SuperDARN map at a pre-defined resolution. Vectors between each grid point are found and the degree of direction change per unit length is calculated at each point to give a quantification of the relative change in direction. The curvature for the global map is averaged in bins of one hour MLT and 1° latitude. Along each

latitudinal hour profile local maxima in the curvature are identified along with local maxima to local minima height. Any maxima or maxima to minima values that do not meet both threshold criteria (5.26 and 3.82 respectively) are excluded. In this way we extract CCB boundaries at each hour of MLT.

This new boundary technique based on the relative change in flow direction as given by SuperDARN map potential data is expected to have use when applied to the noon and midnight regions. A more detailed statistical study and comparison to the CRB will be presented in chapter 5 to capture the key similarities and differences including the effect of a range of IMF conditions. As the CRB has been extensively studied, understanding the subtleties between the two techniques is important in determining its applicability for use in future studies.

Chapter 5

Statistical Comparison between the Convection Reversal Boundary (CRB) and Convection Curvature Boundary (CCB)

This Chapter will focus on statistical comparison between the Convection Curvature boundary (CCB) as outlined in Chapter 4 and the Convection Reversal Boundary (CRB). The CRB is readily observable using global SuperDARN data as the sunward/anti-sunward direction of flow forms a separator between two distinct magnetospheric regions (*Sotirelis et al.*, 2005). As has been discussed in Chapter 4 this definition is widely-used but is also recognised to be less well-defined in the noon/midnight regions. This motivated the derivation of an alternative boundary extraction from SuperDARN in an effort to combat some of these problems. In this chapter emphasis will be placed on comparing the statistical differences between these two techniques over a common dataset. Understanding the subtleties of how each method responds to varying IMF conditions and during solar minimum and maximum is important to assess the new technique for future use.

5.1 Methodology

In this section the primary datasets from SuperDARN used in this chapter are described. The CCB and CRB methods (outlined briefly below) are used to extract boundary locations for all SuperDARN maps during May 2000 to August 2002. This particular time period is chosen for analysis to coincide with the IMAGE satellite orbit during which an extended time was spent imaging the northern polar cap. In this way the statistical results of the boundary technique can be directly compared to the IMAGE global auroral data/OCB (see chapter 6). CRB and CCB locations are also extracted from a secondary time interval spanning May 2010 until August 2012. Although this time period cannot be utilised in Chapter 6 to directly compare with IMAGE auroral data it will provide a 'solar minimum' dataset for comparison with the 2000-2002 data which incorporate solar maximum. Figure 5.1 shows the locations and fields of view of the nine operational northern hemisphere SuperDARN radars during these two time spans. This figure shows the interval between the two periods saw a significant expansion of the SuperDARN network in the northern hemisphere. The number of radars has doubled

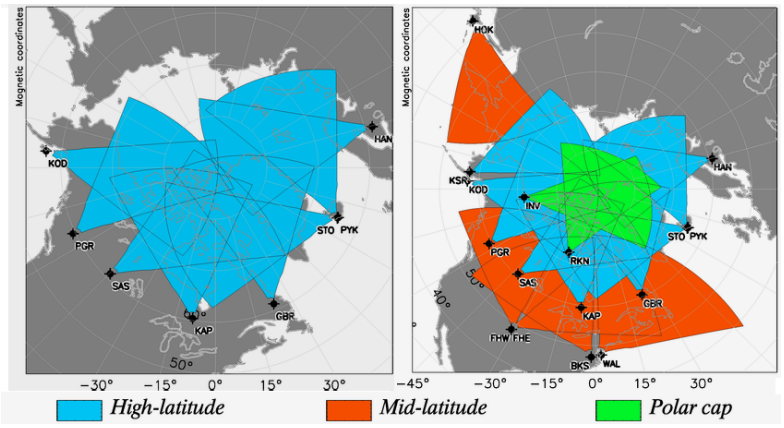

FIGURE 5.1: The locations and fields of view of the operational northern hemisphere SuperDARN radars during the time periods A) May 2000 - August 2002 B) May 2010 - August 2010. [image credit: vt.superdarn.org]

and the later coverage includes the polar cap and lower latitude radars (green and red respectively).

The Convection Reversal boundary (CRB) is extracted from the SuperDARN map data and follows a similar method to that outlined in *Bristow and Spaleta* (2013). Their study utilised the SuperDARN global convection maps and averaged the zonal velocity components in 1 hour MLT and 1° magnetic latitude bins. The CRB boundary extraction used by *Bristow and Spaleta* (2013) constrained the analysis to MLT regions where there were direct radar measurements both poleward and equatorward of the boundary, as is evident in Figure 5.2. The analysis in this chapter puts no such constraints on

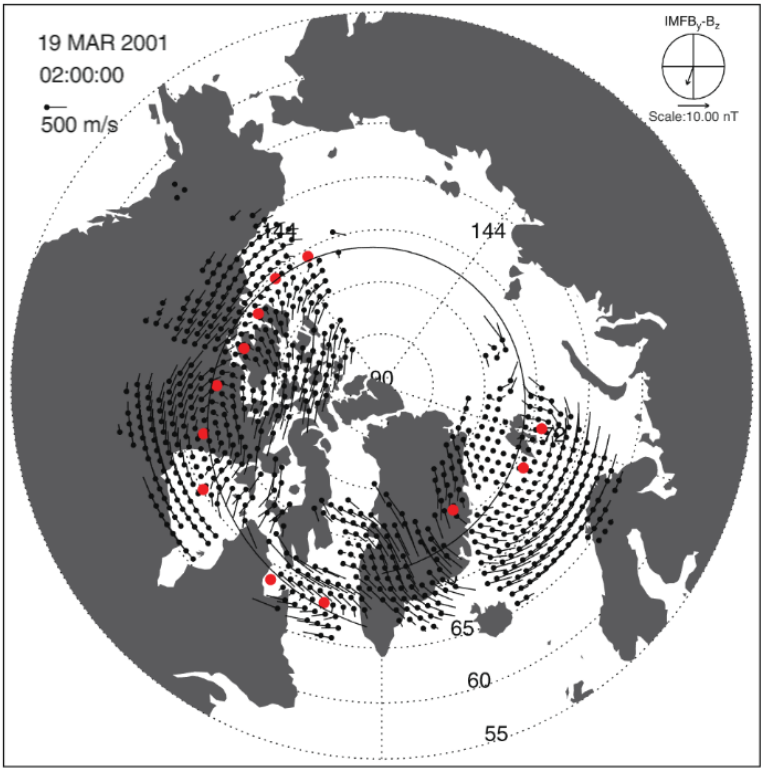

FIGURE 5.2: An example showing the CRB identifications in each MLT sector (red dots) extracted from a SuperDARN global convection map and taken from *Bristow and Spaleta* (2013). The plot is shown in geomagnetic coordinates with the magnetic pole at the centre, Noon to the top and Dusk to the left. The IMF clock angle and magnitude is shown in the dial in the top right corner.

location and quantity of radar backscatter and boundaries from all hours of MLT are utilised. Instead, it is our goal to compare the two techniques as applied globally to the SuperDARN convection patterns, as provided by ECLAT. We consider separately the significance of radar data coverage in Chapter 6.

Extraction of the Convection Curvature Boundary (CCB) has been thoroughly outlined in Chapter 4 and this method extracts boundaries from all available SuperDARN maps. The next section will first present examples of CRB/CCB boundary determinations at two time periods to highlight some behaviours of both techniques. Following this a statistical overview of the CRB/CCB boundary determinations and their distributions over a number of IMF conditions and at differing periods of the solar cycle is shown. Discussion of the results and concluding remarks are presented in Sections 5.3 and 5.4 respectively.

5.2 Data Presentation

5.2.1 Examples of CRB/CCB determination

Figure 5.3 shows a convection map on 30 December 2001 at time 21:58 UT plotted in geomagnetic coordinates. The IMF had a strong, predominantly B_z negative component of -8nT. There is good coverage of the dusk cell and midnight region with velocity data covering well the region 68° - 80° MLAT. The blue dots on the map show the CCB boundary identifications and the red dots the CRB. Boundary observations are calculated in all MLT sectors. It is evident that in a significant number of MLT sectors multiple

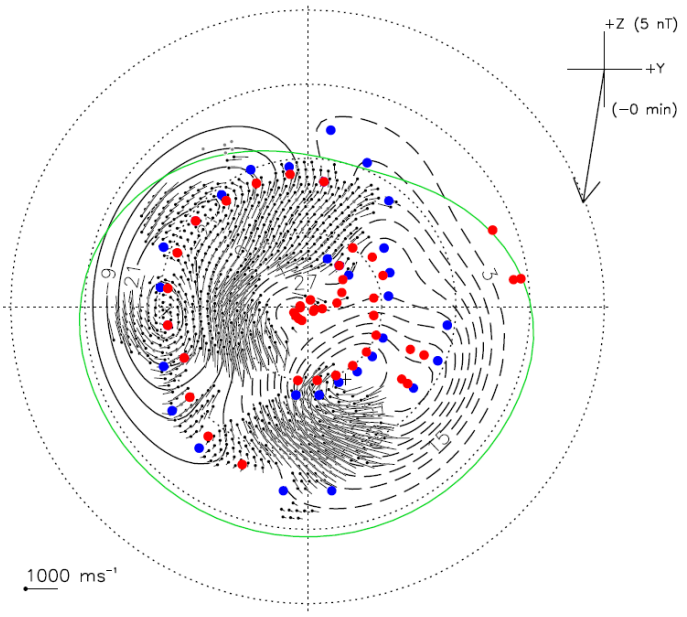

FIGURE 5.3: Convection map for 2158 UT on 30 December 2001 showing CRB identifications in red and CCB identifications in blue. The map is plotted in geomagnetic coordinates, with the magnetic pole at the center, noon at the top, and dusk on the left. The clock dial in the upper right shows the IMF magnitude and polar angle.

boundaries are identified. There are a cluster of very high latitude CRB boundaries close to 90° which act to cause multiple boundaries to be recorded at dawn and dusk (05-07 and 15-19 MLT). These appear to be the result of irregular kinks in the convection flow estimate as a result of poor map potential model fitting in this area. Close to 90° MLAT the dominant east-west velocity direction becomes less well defined and makes the presence of these boundaries more likely. Over the 12-22 MLT region the two boundaries behave very similarly noting that the CCB tends to be 1° - 2° lower in latitude than the CRB in regions with strong flow shear. This is likely due to the fact that the CCB identifies an area that first experiences a significant flow direction change which usually occurs before the dominant east-west direction changes.

This figure shows some additional differences. The first is the addition of a low-latitude

CCB identification in the 23-00 MLT sectors. There are still significant velocity measurements in the region reducing the likelihood of curvature being related to a bad model fit. The subtle change in direction of flow is identified by the CCB but not the CRB as it does not switch predominant direction from east to west. The CRB jumps over 10° MLAT forming a discontinuity between 23-00 MLT, such as has been found by *Bristow and Spaleta* (2013). Identification of a lower latitude CCB between 22-01 MLT that does not observe a latitude jump and is consistent with the velocity data could indicate that the CCB is able to identify flow associated with lower latitude phenomena. Secondly, a group of 3 CRB identifications at 06 and 08 UT MLT at 62° MLAT are on the edge of the convection pattern. This can be a common feature at MLT's close to dawn and dusk where additional cells can be present as an artefact of the map potential fitting algorithm, but these are not included in the CCB.

Figure 5.4 shows a second convection map example of 2 April 2002 04:48 UT. Some features applicable to this map have already been identified in the previous figure. Namely, CRB identification at the edge of the convection pattern close to dawn and multiple identifications of the CRB due to curvature close to 90°. Additionally, a group of apparently erroneous CRBs are seen to extend to lower latitudes through 09-11 MLT and 21-23 MLT. These boundaries are due to east-west flow reversals occurring at potential magnitudes of less than |3|kV and as such the corresponding equipotential cannot be seen on this map format.

This map is interesting as the CCB technique extracts two boundaries in the 15-19 MLT dusk region. One of these lies as 80° MLAT alongside the CRB where there are no direct radar measurements. At lower latitudes of approximately 70° MLAT there are direct

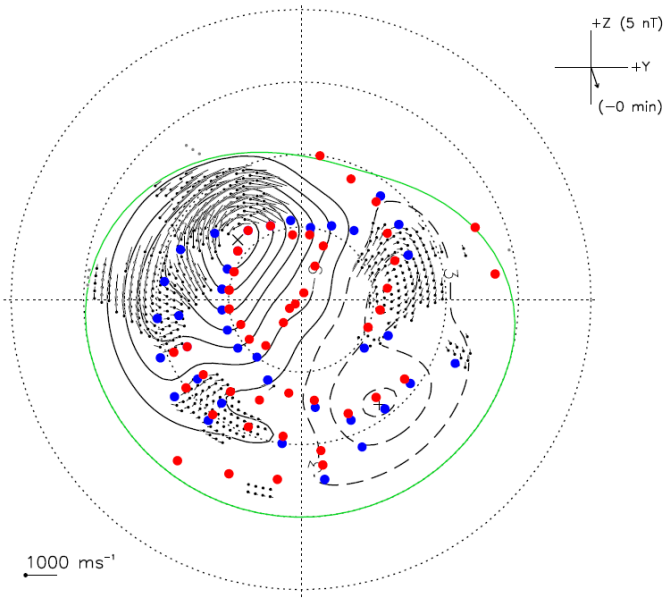

FIGURE 5.4: Convection map for 0448 UT on 02 April 2002 showing CRB identifications in red and CCB identifications in blue. The map is plotted in geomagnetic coordinates, with the magnetic pole at the center, noon at the top, and dusk on the left. The clock dial in the upper right shows the IMF magnitude and polar angle.

radar observations and evidence of a second boundary. In particular at 18 MLT, a clear reduction in flow strength is apparent at 72° MLAT, indicating a real physical change in the flow. Again, this shows an example of the predominant east-west flow direction not changing but some significant flow direction change observed. This consistently occurs with a more rounded cell (as the two examples have shown) and highlights a difference in the behaviour of the CCB to the CRB. The CCB identifies regions where there is a physical change irrespective of the dominant east-west flow direction.

5.2.2 Overview of CRB/CCB boundary determinations

An overview of the number of SuperDARN boundaries extracted for both the CRB and CCB techniques is presented in Figure 5.5. Occurrences of boundaries for the CRB are

shown in Figure 5.5a and occurrences for the CCB are shown in 5.5b. Additionally, as multiple boundary locations can be extracted from a latitudinal profile per MLT this figure also shows the frequency of extracting a single (dark blue), double (light blue) or triple(+) (yellow) boundary location for a given MLT sector. Triple(+) is so-called as it could contain three or more boundary locations. The CRB method shows an approximately bimodal distribution for the frequency of observing a single boundary in a given MLT region, peaking at (3-4) and (14-18) MLT. In the pre-noon region it becomes more likely to observe more than one boundary location. The maximum number of boundaries are extracted at times close to midnight for the CRB as it is most likely to extract a triple(+) boundary as shown by the yellow fraction.

This result is not unexpected as the CRB is latitudinally constrained at dawn/dusk as convective flow travels perpendicular to a magnetic longitude line. Therefore a CRB boundary can be extracted with little ambiguity and the likelihood of multiple boundaries in these sectors is reduced. Pre-noon and Pre-midnight show the largest occurrences of multiple boundary extractions. From the dayside to nightside cusp the direction of travel often straddles a magnetic longitude line i.e. the boundary of whether flow is deemed 'eastward' or 'westward'. This means the possibility of flow changing east/west direction over the polar cap is high, giving way to a higher frequency of boundaries extracted. In the pre-midnight sector the size of convection extends to lower latitudes making triple(+) boundary locations the favoured result.

Across all magnetic local times the occurrence of CCB locations appears more stable. The greatest occurrence of single boundaries occurs at 14-15 MLT with another smaller peak at 06-08 MLT. The liklihood of a single boundary decreases as we move around to

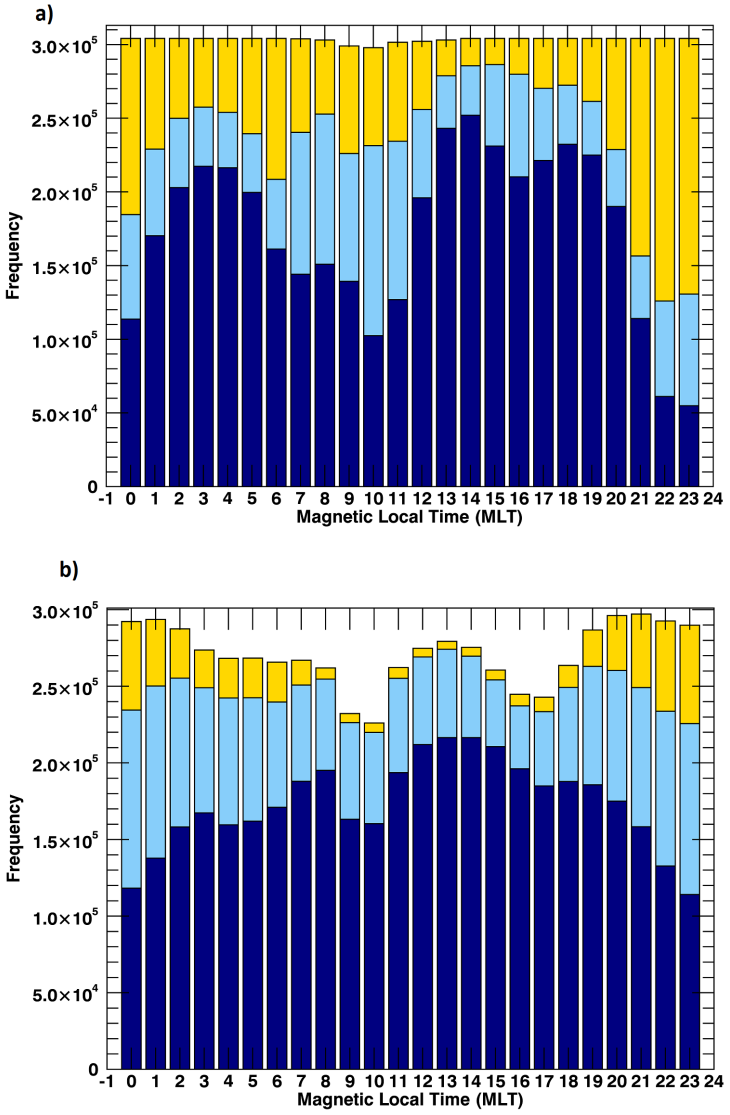

FIGURE 5.5: The frequency a single [Dark Blue], double [Light Blue] or triple(+) [Yellow] boundary location extracted from a given SuperDARN map using data from May 2000 to August 2002 for a) the CRB technique and b) the CCB technique.

midnight and double identifications are favoured. In general at most MLTs it is more likely that a single CCB is extracted with the exception being between 22-01 MLT. The reason that double or triple(+) identifications are more likely here could be due to contamination from 'wavy' contours due to the cross polar cap flow. Another reason could be boundaries associated with low latitude flows as were seen, for example in the test case shown in section 5.2.1 (Figure 5.3). Given that the extraction of a CCB location is constrained to equipotentials greater than |3|kV and threshold values are applied to reduce 'insignificant' flow shear, it is expected that fewer CCB boundary locations are extracted overall than for the CRB. In addition, this threshold criterion is the reason why there is a dip in Figure 5.5b pre-noon. The pre-noon region is the typical separator between the 'Dungey-like' dawn and dusk cells presenting a small gap between the |3|kV equipotentials as can be seen in climatological maps of the convection e.g. (*Ruohoniemi and Greenwald*, 1996). As such it is possible if this region spans an MLT hour then no boundary will be detected.

The CCB technique shows less possibility overall to extract multiple boundaries, three or more in an MLT sector occurs relatively infrequently. In the nightside region (between 22-02 MLT) the likelihood of multiple boundaries is increased. The largest difference between the two techniques can be seen pre-noon. It is much more likely to observe a single boundary using the CCB.

5.2.3 Distributions of CCB/CRB identifications

5.2.3.1 Justification for binning according to the minimum HMB

As discussed in the introduction the large-scale convection pattern at a given time is ultimately dependent on the IMF clock angle and magnitude, the dipole tilt angle e.g. (*Ruohoniemi and Greenwald*, 1996; *Pettigrew et al.*, 2010) and magnetotail effects driven by internal plasma processes (e.g. *Grocott et al.* (2017)). During the following sections statistical dependencies of both boundary techniques are presented according to various parameters. It is common in such studies (e.g. *Bristow and Spaleta* (2013); *Koustov and Fiori* (2016); *Chen et al.* (2015); *Chen and Heelis* (2018)) to organise the observational data according to combinations of IMF clock angle and magnitude. As a first approximation the entire convection pattern can be characterised according the IMF. In reality, the resultant pattern can be considered as a combination of two separate time-dependent processes occurring (Holzworth and Meng, 1985). Firstly, reconnection at the dayside magnetopause from solar wind-magnetosphere coupling which may result in a delayed tail response to the conditions of the solar wind-magnetosphere coupling. As the high latitude ionospheric response to incoming solar wind conditions is not the same across all MLT sectors the convective flow is better characterized by the OCB (*Cowley and Lockwood*, 1992). *Sotirelis and Newell* (2000) and most recently *Chisham* (2017) all took steps in their analysis to account for an expanding and contracting OCB. As flow can change sharply at the OCB the result of not accounting for the changing size of the boundary is that statistical patterns can become smoother and more spread out. Any sharp features around the boundary locations may not be fully captured. Each mentioned study concluded that this gave results that more accurately resembled

observations with *Chisham* (2017) presenting specifically the improvement that can be achieved when applying this consideration to SuperDARN data. As such the decision was made to order the boundary distributions presented here by the size of the polar cap. Owing to a lack of a continuous OCB monitor for the intervals under investigation we choose instead to use as a proxy the Heppner-Maynard boundary (HMB). We acknowledge that the relationship between the HMB and OCB is not strictly linear, but it has been shown to be a suitable proxy by *Imber et al.* (2013). Thus, although this analysis does take place in a fixed geomagnetic coordinate system, binning by the minimum latitude of the HMB should effectively scale the convection patterns and order the latitudinal spread in our statistical results.

5.2.3.2 Instrumental Bias

An important consideration to make before drawing conclusions between the distributions is the extent of SuperDARN coverage of the northern hemisphere at each time period. SuperDARN increased its number of operating radars in the northern hemisphere from 8 to 15 as shown in Figure 5.1. The differing latitudinal range of the radars between the two time periods will affect the low-latitude cut-off. The 2000-2002 radar network is comprised of the high-latitude radars. These have a low latitude limit of approximately 60° although the optimum observational limit is farther poleward (*Bristow and Spaleta*, 2013).

Figure 5.6a shows the frequency of velocity observations as a function of magnetic latitude and local time for the 2000-2002 period. The highest incidence of radar observations is centered on 70° MLAT across 22-00 MLT although all nightside MLTs show a peak

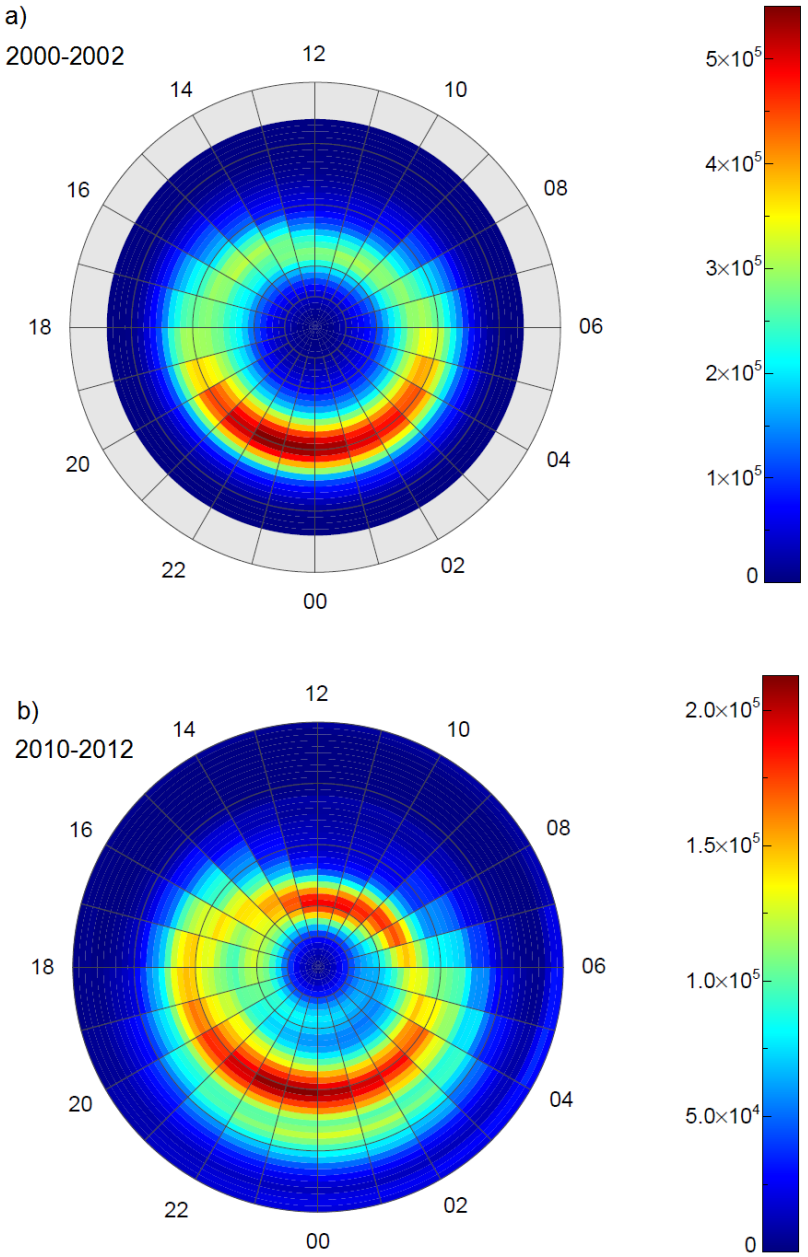

FIGURE 5.6: The incidence of velocity observations as a function of MLT and magnetic latitude for a) May 2000 to August 2002 and b) May 2010 to August 2012. The circular gray lines begin at 50° MLAT and increment every 10°.

in incidence at 70° MLAT. Towards the dayside the peak in incidence shifts poleward where, at noon it centres on 77° MLAT. Figure 5.6b shows the result for the 2010-2012 years where there are some notable differences. Radar observations are now observed down to 50° MLAT. The peak incidence for the nightside has shifted equatorward a few degrees to 68°-69° as well as a secondary peak at approximately 63° between 22-02 MLT. There are also a greater number of observations at all MLTs farther equatorward than in Figure 5.6. As with 2000-2002 the peak incidence occurs at higher latitudes as you approach noon however, in this case the peak incidence is farther poleward at 79° compared to 78°. As the SuperDARN data is organised according to the HMB the convection patterns are effectively scaled. As the results are presented the HMB can be chosen to mitigate the effect of the low-latitude cut-off of the radars. This will be done by ensuring the majority of the boundary identifications occur poleward of the highest incidence of scatter.

5.2.3.3 Comparison between datasets

Figure 5.7 shows the spatial distribution for the CRB (5.7a and 5.7b) and the CCB (5.7c and 5.7d). Figures 5.7a and 5.7c show the results for May 2000 - August 2002. Figures 5.7b and 5.7d show the results for May 2010 - August 2012. The latter years form a complimentary dataset that occurs during the ascending phase of the solar cycle allowing comparison of the data over different periods. The results are shown for a HMB of 55° as this is high enough that both the 2000-2002 and 2010-2012 datasets contain peak boundary identifications that occur clearly within the low-latitude limit of radar observations (as presented in Figure 5.6).

Both the CCB and CRB show similarity in the dawn and dusk regions, specifically between 14-20 MLT and 02-08 MLT in that there is a clear dominant peak occurrence around 75° MLAT. The CRB technique (5.7a and 5.7b) has a spread of occurrences at the lower latitudes that peaks at the edge of the observations (57.5°-65°) at almost all MLT sectors in both the 2000-2002 and 2010-2012 datasets. The highest incidence for this lower latitude population is in the pre-noon sector, although, for Figure 5.7a high occurrences occur through to dawn. The CCB technique in Figures (5.7c and 5.7d) show a relatively small lower latitude population in the 04-08 MLT sector spread between 63°-68° latitude. In the pre-noon region the CCB diverges into two clearly identifiable regions, a higher (81.5°) and lower latitude band (72.5°-74.5°). In the 2010-2012 distribution these two pre-noon regions are sharpened. In this MLT region the CRB is less clear and there is a lot of variability in the locations of the boundary identifications including boundaries identified right up to the pole. In the pre-midnight region there is a lot of variability in boundary latitude identifications for both the CRB and CCB technique. Both reveal a distinct lower latitude population at approximately 64.5° MLAT. In the 2010-2012 dataset this population becomes sharper and extends into the early morning sector for both techniques

Figure 5.8 shows the median and interquartile range (IQR) of the boundary identification latitudes for each MLT sector. The top plot shows the result for the CRB technique (corresponding to Figures 5.7a and 5.7b), the dark red colour shows the result for the 2000-2002 dataset and the result for the 2010-2012 dataset is overlayed as the light red. In addition to the mean and IQR solid squares are also overplotted, these are manually identified peaks using the MLT sector distributions to highlight latitudes that have a clear boundary identification population. The bottom figure shows the result for the

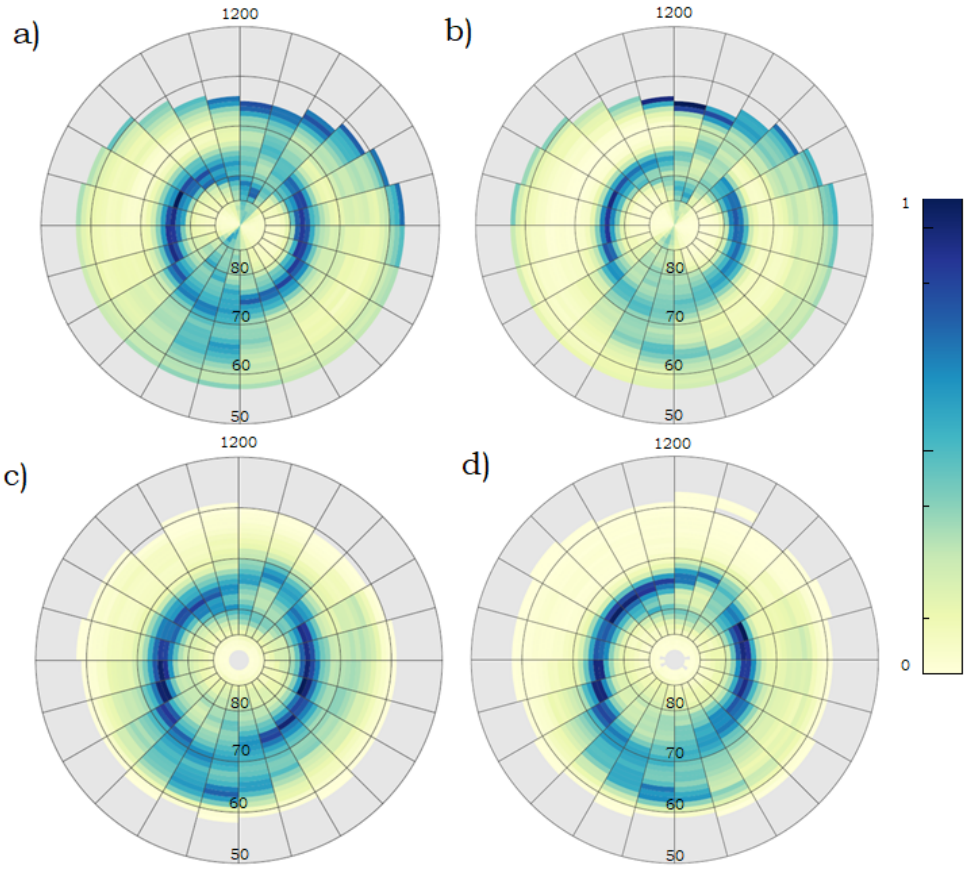

FIGURE 5.7: Distributions of CRB (top two) and CCB (bottom two) identifications over May 2000 - August 2002 (left) and May 2010 - August 2012 (right). The plots show the result of all SuperDARN maps in the mentioned time periods with a minimum Heppner-Maynard latitude of 55°. The grey grid is centred on the magnetic pole and extends to 50 MLAT, noon is orientated to the top of the page and dusk to the left.

CCB and is in the same format as described above, although, this time the results for the 2000-2002 dataset are dark blue and results for 2010-2012 shown in light blue.

The CRB technique shows a large IQR across almost all MLT's, this is most obvious from the midnight to pre-noon region. The IQR range is much larger than expected in the dawn region, the solid squares indicate the latitude where there is a peak in the boundary identifications. There are many peaks at the edge of the convection pattern as were seen in the distribution plots (5.7a-b). This low-latitude population of boundary identifications is responsible for the large IQR across almost all MLTs as the median value is shifted equatorward away from the 'main' occurrence at approximately 75°. This is true also for the CCB technique (the bottom plot in Figure 5.8) where the dawn region was shown to have a spread of low latitude boundary identifications increasing the IQR. In the pre-noon to noon region the CRB shows at least 3 solid squares indicating peaks in boundary locations at a variety of latitudes, this, together with a large IQR highlights the high level of variability here. For the CCB technique there are two solid peaks which correspond to the high and low latitude band observed in the distribution plots in Figure 5.7. The median value is shifted to sit between both peaks which suggests that although the lower-latitude peak is contributing the most, the poleward peak is still significant. In the nightside region the peak boundary identification latitudes are harder to discern as there are large populations of data occurring at a wide range of latitudes. This made identifying clear peaks difficult. For both the CRB and CCB there were two identifiable peaks, one at a latitude of 70° and a lower latitude peak at 65°. The nightside lower latitude peak of boundary identifications is seen across 23-01 MLT for the CRB and 23-02 MLT for the CCB. In addition, there are also significant high-latitude populations

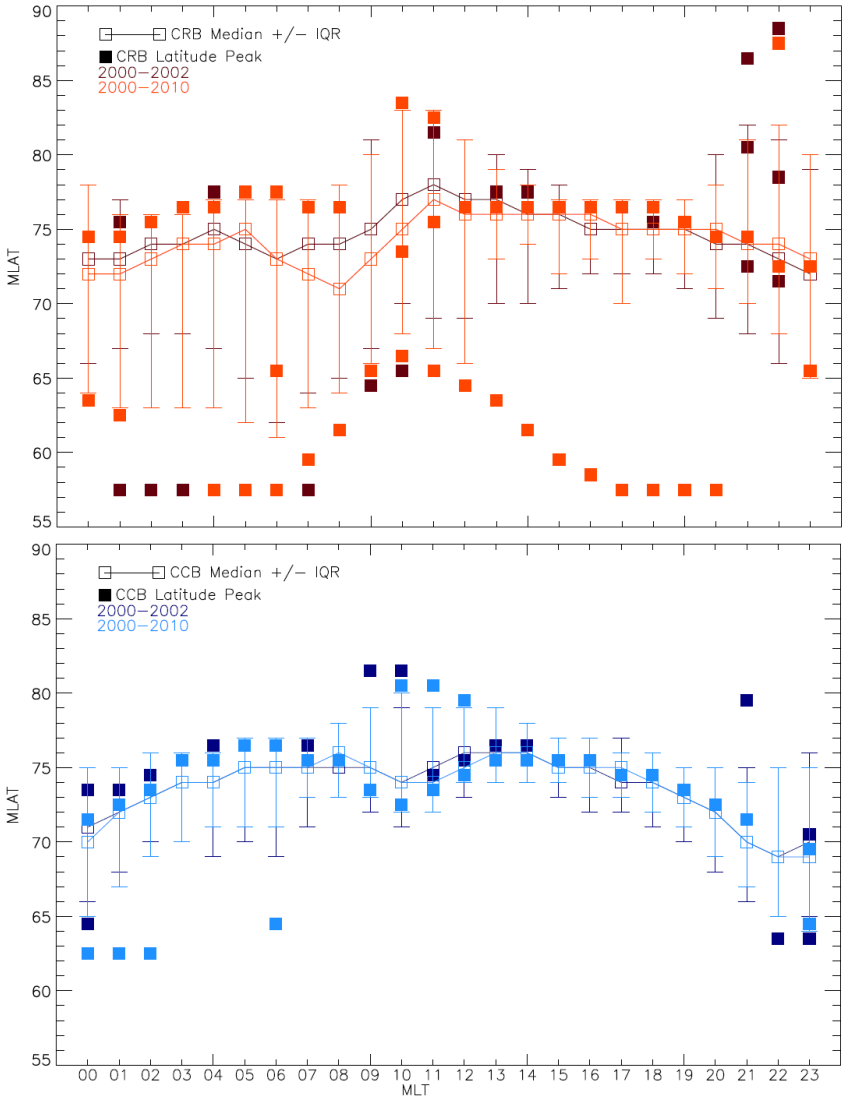

FIGURE 5.8: An MLT/MLAT plot for the CRB (top) and CCB (bottom) showing the median and interquartile range for a minimum Heppner-Maynard boundary of 55°. The dark colour in each plot shows the result from May 2000 - August 2002 and the lighter colour for May 2010 - August 2012. The solid squares show the locations of clear manually identified peak occurance latitudes.

TABLE 5.1: The median and IQR for the CRB and CCB techniques in four MLT regions for the 2000-2002 dataset. Values are taken from Figure 5.8.

2000 - 2002				
	CRB		CCB	
MLT	Median	IQR	Median	IQR
05	74°	12°	75°	7°
11	78°	12°	75°	7°
17	75°	5°	74°	5°
23	72°	13°	70°	11°

TABLE 5.2: The median and IQR for the CRB and CCB techniques in four MLT regions for the 2010-2012 dataset. Values are taken from Figure 5.8.

2010 - 2012				
	CRB		CCB	
MLT	Median	IQR	Median	IQR
05	75°	15°	75°	5°
11	77°	14°	74°	7°
17	76°	4°	75°	3°
23	73°	14°	69°	10°

of CRB identifications as can be seen in MLT regions 21-22 MLT.

Tables 5.1 and 5.2 summarise the median and IQR for the 2000-2002 and 2010-2012 datasets for both the CRB and CCB (taken from Figure 5.8)in four key regions dawn(05 MLT), pre-noon (11 MLT), dusk (17 MLT) and pre-midnight (23 MLT). The IQR for the CCB is less than the CRB IQR across almost all MLT regions, except the dusk region where the values are comparable.

The CRB median value is almost always higher than its CCB counterpart (the exception being at 05 MLT). However, looking at the median value alone may not give an accurate comparison between the techniques because as we have seen, the CRB medians are pulled equatorward, especially around dawn due to the numerous boundaries identified at latitudes close to the edge of the convection pattern. These additional low-latitudes boundaries are attributed to the common presence of additional, low potential cells in

the dawn and pre-noon sectors. This agrees with examples presented in section 5.2.1 (and others)and confirms that they are a common feature of the CRB technique. In fact, for the 2000-2002 dataset the largest peak latitude occurrence was at 77° compared the the CCB at 76°, which suggests for this main population the CRB is centred 1° higher than the CCB, contrary to what the medians suggest. At dusk, where the IQR is the smallest for both the CRB and CCB the median is centred on the largest peak latitude occurrence suggesting the median and IQR well capture the spread. As Table 5.1 shows, here the CRB main boundary latitude occurrence is 1° higher than the CCB. In the pre-noon region the CRB median value is significantly higher than the CCB. This is due to a dominant population of CRB identifications at higher-latitudes (81° MLAT) consistent with previous observations where the CRB is shifted towards the pole as a result of the CRB being less defined here. There is still large variability in this sector and a significant portion of boundaries being identified at the edge of the convection pattern. This is as a result of unphyiscal boundaries being extracted due to poor model fitting close to the boundary. This has been shown earlier in this chapter in one of the test case SuperDARN maps (Figure 5.4). The CCB has shown two clear latitude bands over the noon sector with less variability than the CRB with the peak occurrence at 73° which is much more consistent with its expected location. In the nightside region Tables 5.1 and 5.2 show that the CCB median is shifted to lower latitudes than the CRB. One of the reasons for this is that the CCB technique makes some effort to remove contamination by cross polar cap flow, therefore boundary identifications at higher latitudes will be less common than for the CRB, shifting the median value equatorwards. In addition, the CCB has shown a clearer more dominant population at lower latitudes in the distribution plots (Figures 5.7c-d) which will also act to shift the median value more equatorwards.

For both the CRB and CCB there are large IQR values which highlights that boundaries are observed over a wide range of latitudes.

From 2000-2002 to 2010-2012 the IQR gets smaller across almost all MLTs for the CCB (except pre-noon). The distribution plot (Figures 5.7c-d) has shown that the peak occurrence latitudes become sharper and there are fewer boundary observations equatorward of the main population. This is likely because of the increase in radar coverage to the lower latitudes. The increase of radar observations at the lower latitudes will decrease the likelihood of boundaries that are identified as a result from poor model fitting as the SuperDARN maps become more data-driven. Interestingly the IQR is seen to increase for most MLTs for the CRB technique. At dawn and pre-noon this is due to an increase in the boundaries that are identified at the edge of the convection pattern. The dusk region does not identify these edge-of-convection pattern identifications and here the IQR does actually improve. In the midnight region the IQR remains similar for both techniques which suggests that there is still a lot of variability in the latitude of boundary observations.

Koustov and Fiori (2016) conducted a statistical analysis of the CRB over a solar cycle and found that the CRB was clearly shifted to lower latitudes during high solar activity (solar maximum) in the dawn and dusk regions. It was noted that the CRB was not well defined in the noon-midnight region and so the relationship in these regions is more variable. The median values of the CRB between Tables 5.1 and 5.2 do show higher latitudes for the 2010-2012 period which coincides with solar minimum. This is not obviously the case for the CCB values which show the pre-noon and midnight region at higher latitudes during the 2000-2002 years which occur close to solar maximum. However, at dawn and dusk, the median values are well constrained with a low IQR and are

shifted poleward by 1° during 2010-2012 in line with the result from *Koustov and Fiori* (2016).

5.2.3.4 Comparison between minimum HMB latitudes

The following analyses investigate the behaviour of the distributions over different minimum Heppner-Maynard boundary latitudes to account for differing activity levels. Figure 5.9 shows the spatial distribution for the 2000-2002 dataset for the CCB a) HM:52°, b) HM:57° and c) HM:62°. For HM:57° the CCB shows similar behaviour across all MLTs as has been described in section 5.2.3.3 for the CCB HM:55° 2000-2002 dataset. For HM:52° there are clear peaks of boundary identifications across the dawn and dusk latitudes at approximately 75°. There are also significant occurrences of boundary identification spread over the lower latitudes, this is especially obvious pre-midnight to dawn. This effect lessens as the HMB increases up to 62°. The midnight region displays high variability across all three HMB latitudes but they all show a low latitude peak population close to the edge of the observed boundary locations. At HM:52° the latitudinal spread covers over 10° MLAT which reduces with the minimum HMB latitude. In the pre-noon region, as the minimum HMB increases the two peak boundary identification latitudes become more clearly separated.

Figure 5.10 shows the median and interquartile range (IQR) of the boundary identification latitudes for each MLT sector for HM:52° (dark blue), HM:57° (light blue) and HM:62° (yellow). The solid overplotted squares are manually identified peak latitudes from the MLT sector distributions. To make this plot more readable and to see all features for each latitude, the information is slightly separated along the MLT axis.

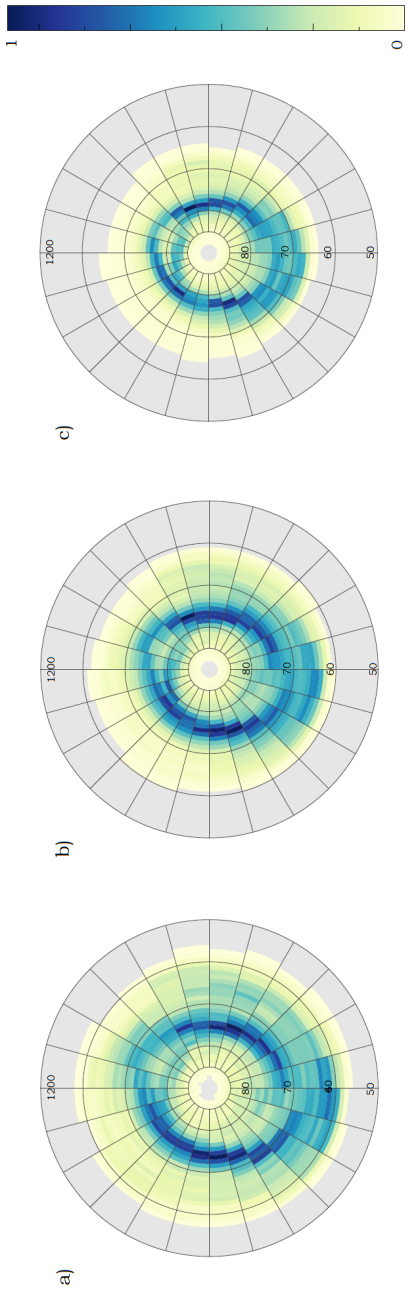

FIGURE 5.9: Distributions of CCB identifications over May 2000 - August 2002. The plots show the result of all SuperDARN maps in the mentioned time period with a minimum Heppner-Maynard latitude of a) 52° b) 57° c) 62° respectively.The grey grid is centred on the magnetic pole and extends to 50 MLAT, noon is orientated to the top of the page and dusk to the left.

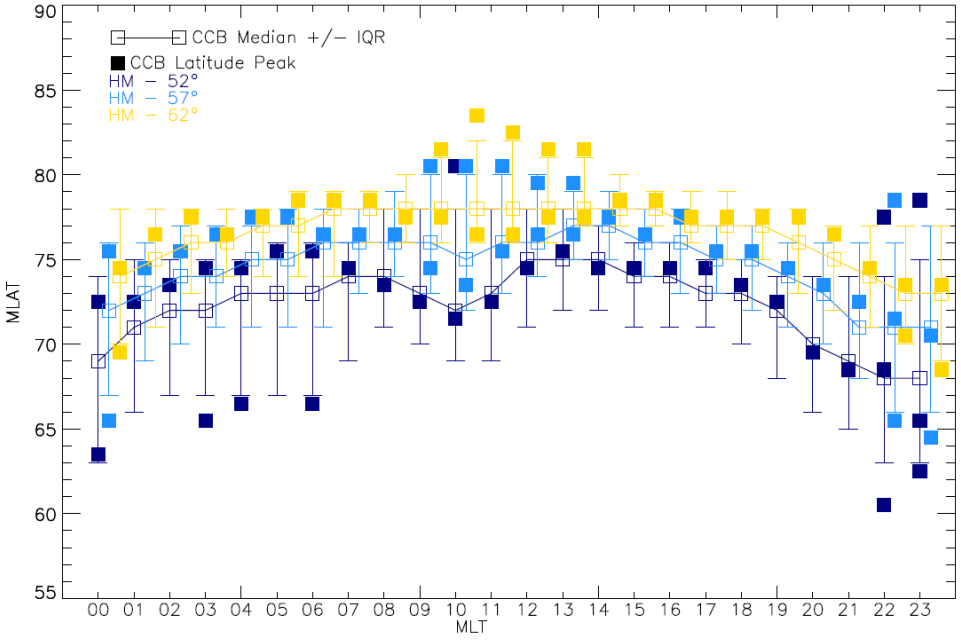

FIGURE 5.10: An MLT/MLAT plot for the CCB with the median and interquartile range of the minimum Heppner-Maynard boundary of 52° (Dark Blue) b) 57° (Light Blue) c) 62° (Gold). The solid squares show the locations of clear manually identified peak occurance latitudes.

In the dawn region the HM:52° has a much larger IQR than the other two minimum HMB latitudes. This is due to the large number of lower latitude boundary identifications in this region as seen in figure 5.9. As the HMB increases the IQR reduces and the median value converges on the peak latitude occurrence (shown as the solid squares). In the dusk region the median and IQR are centred on the peak latitude occurrences showing that a single boundary identification is highly likely here. The dominant peak in the dawn and dusk regions shifts poleward on the order of 3° as the minimum HMB latitude increases from 52° to 62°. In the pre-midnight region there are peak boundary identification latitudes at 60°-63° for the HM:52° case, these lower latitude peaks occur at 68°-71° for HM:62°. The shift of these is approximately 8°, larger than the shift at the dawn and dusk MLT sectors.

TABLE 5.3: The median and IQR for CCB technique in four MLT regions for HM:52°, HM:527° and HM:62°. Values are taken from Figure 5.10.

CCB						
	HM:52°		HM:57°		HM:62°	
MLT	Median	IQR	Median	IQR	Median	IQR
05	73°	9°	75°	7°	77°	5°
11	73°	9°	76°	7°	78°	6°
17	73°	4°	75°	4°	77°	4°
23	68°	12°	71°	11°	73°	8°

Table 5.3 summarises the median and IQR for HM:52°, HM:57° and HM:62° in four key regions dawn(05 MLT), pre-noon (11 MLT), dusk (17 MLT) and pre-midnight (23 MLT). The median values increase approximately 4° in each MLT region with the IQR reducing as the minimum HMB increases. The dawn region is the best constrained with the lowest IQR, with the pre-midnight region being the most variable (with the highest IQR). The shift poleward of the peak boundary latitude at dawn and dusk is consistent with results found by *Bristow and Spaleta* (2013) and *Koustov and Fiori* (2016) who showed that their CRB latitude shifted equatorward by 1°-2° with increasing strength of the IMF B_z. Given the strong correlation between the HMB latitude and IMF B_z (*Heppner and Maynard*, 1987), our result is attributed to the same physical mechanism. The poleward shift of the low-latitude population in the nighstide was shown to be on the order of 8° which is double that is observed at dawn and dusk. When the minimum HMB is at lower latitudes the ionospheric convection pattern is large which is suggestive of high levels of activity e.g. magnetospheric substorms (*Imber et al.*, 2013). During these times the auroral oval can broaden (*Craven and Frank*, 1987) and associated ionospheric flows which occur at the equatorward boundary, for example, the Harang discontinuity, occur at lower latitudes. If the low-latitude peak boundary identifications for the HM:52° are connected with these types of flows it could explain why there is such a difference in

latitude between HM:52° and HM:62°.

Figure 5.11a-c shows the spatial distribution for the CRB 2000-2002 dataset for a) HM:52°, b) HM:57° and c) HM:62°. At all HMB latitudes there is a clear peak boundary identification around dawn and dusk. At HM:52° and HM:57° there is variability observed over a wide range of latitudes from pre-midnight to post-noon. In particular, there are clear populations of boundaries identified at the edge of the convection pattern as has been noticed in section 5.2.3.3 extending from dawn to dusk over the noon region. At HM:62° this effect is mostly reduced to the pre-noon region although there is some limited evidence of it from 15-18 MLT. Between 10-11 MLT the HM:52° does not appear to have a clear dominant latitude for the boundary identifications and a discontinuity can be seen at around 75°. As the minimum HMB increases a high latitude population becomes more well defined at approximately 86°.

Figure 5.12 is the same format as figure 5.10 which is described earlier in this section. The dawn region has the largest IQR across all the MLTs and particularly for HM:52° the median is shifted equatorward from the peak boundary identification latitude (solid square) which is approximately 4° higher than the median. This effect lessens as the minimum HMB increases and the populations of the low latitude identifications decrease. At dawn the dominant peak occurrence shifts poleward by 4° as the minimum HMB increases from 52° to 62°. At dusk the latitude shift is the same order of magnitude. The noon and midnight regions are shown to be highly variable with peak boundary identifications occurring over a wide range of latitudes. As the minimum HMB boundary increases to 62° the number of high latitude populations increases. In the noon region the median value for HM:62° is shifted significantly more poleward towards the peak

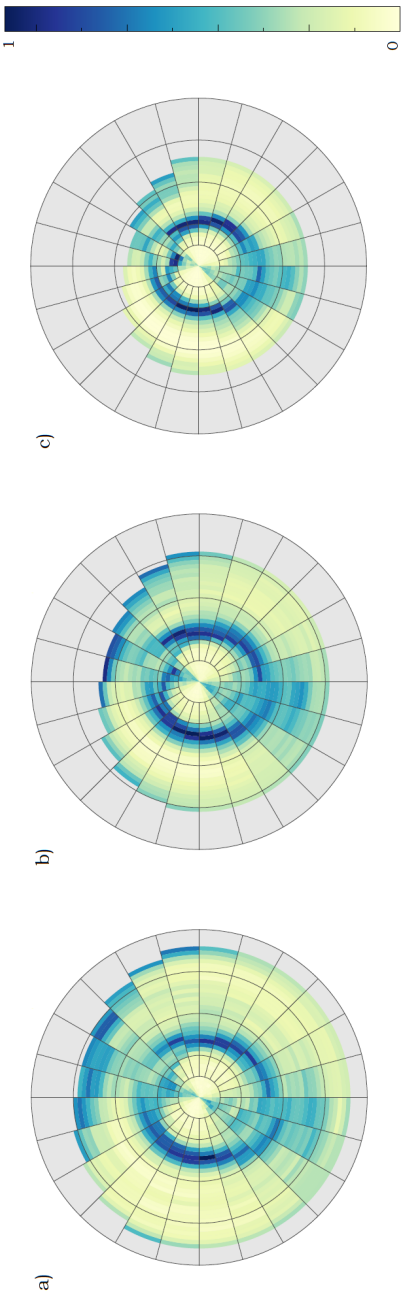

FIGURE 5.11: Distributions of CRB identifications over May 2000 - August 2002. The plots show the result of all SuperDARN maps in the mentioned time period with a minimum Heppner-Maynard latitude of a) 52° b) 57° c) 62° respectively.The grey grid is centred on the magnetic pole and extends to 50 MLAT, noon is orientated to the top of the page and dusk to the left.

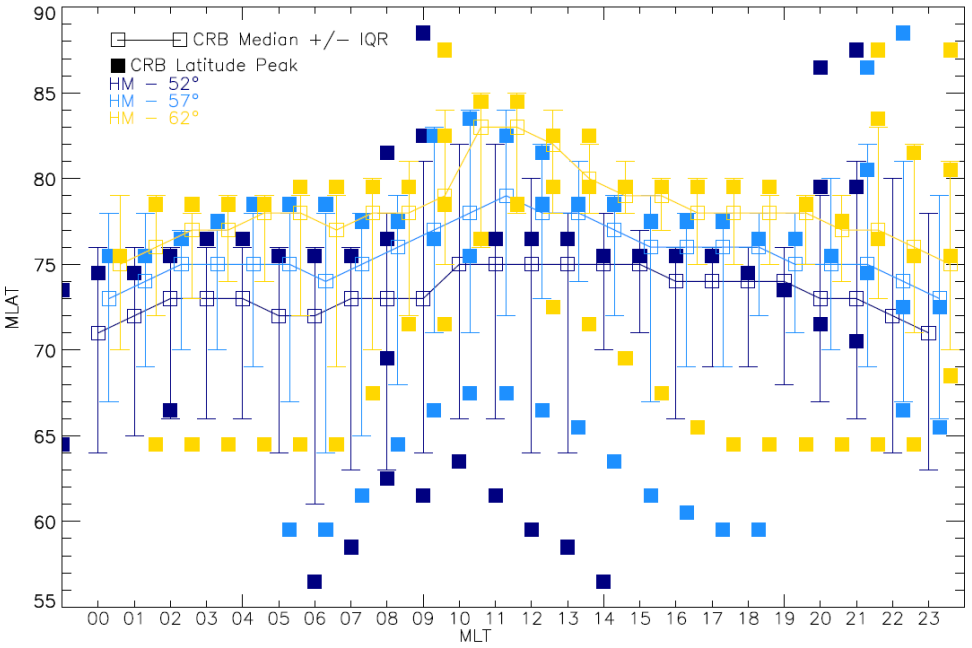

FIGURE 5.12: An MLT/MLAT plot for the CRB with the median and interquartile range of the minimum Heppner-Maynard boundary of 52° (Dark Blue) b) 57° (Light Blue) c) 62° (Gold). The solid squares show the locations of clear manually identified peak occurance latitudes.

TABLE 5.4: The median and IQR for CRB technique in four MLT regions for HM:52°, HM:57° and HM:62° for four . Values are taken from Figure 5.10.

CRB						
	HM:52°		HM:57°		HM:62°	
MLT	Median	IQR	Median	IQR	Median	IQR
05	72°	12°	75°	11°	78°	7°
11	75°	16°	79°	12°	83°	7°
17	74°	7°	76°	9°	78°	5°
23	71°	15°	73°	13°	75°	11°

boundary identification latitude at 84°, showing that this has become the dominant boundary for this MLT sector with less variability than the other HMB distributions.

Table 5.4 summarises the median and IQR for HM:52°, HM:57° and HM:62° in four key regions dawn(05 MLT), pre-noon (11 MLT), dusk (17 MLT) and pre-midnight (23 MLT). The median values shift poleward by approximately 8° for 05 and 11 MLTs which is larger than was observed for the CCB. However, these values are also accompanied

by a large IQR and as shown in Figure 5.12 the medians are often offset from the main peak boundary occurence in these locations. At dawn where the IQR is the smallest the poleward shift is on the order of 4° which is consistent with the CCB. In general, it is more difficult to assess the patterns and trends for the CRB as they are more variable particularly around the dawn and pre-noon MLT regions.

5.2.3.5 Effect of By on the CCB and CRB identifications

The final analysis of the boundary data concentrates on the distributions for the CRB/CCB over the 2000-2002 dataset split according to the predominant IMF B_y conditions. For each minimum HMB latitude all maps were split into two groups based on the IMF B_y direction associated with the SuperDARN map. The resultant spatial distributions are shown in Figure 5.13 with 5.13a-b showing the results for the CRB technique and 5.13c-d showing the results for the CCB. The IMF B_y orientations are split with 5.13a and 5.13c showing the result for IMF B_y+ and 5.13b and 5.13d showing the result for IMF B_y-. Many of the features of the distributions have already been discussed in sections 5.2.3.3 and 5.2.3.4 so only newly identified features related to the IMF B_y will be mentioned.

The distributions show significant deviation from previous results in sections 5.2.3.3 and 5.2.3.4 in the pre-noon sector. For the IMF B_y+ case (5.13a and 5.13c) both the CRB and CCB techniques show a discontinuity in the peak boundary identification latitudes between 09-11 MLT. The gap jumps from lower latitudes in the dawn sector to higher latitudes just post-noon with the CRB identifications peaking at latitudes of 85° compared to 80° for the CCB. For the IMF B_y- case (5.13b and 5.13d) a discontinuity

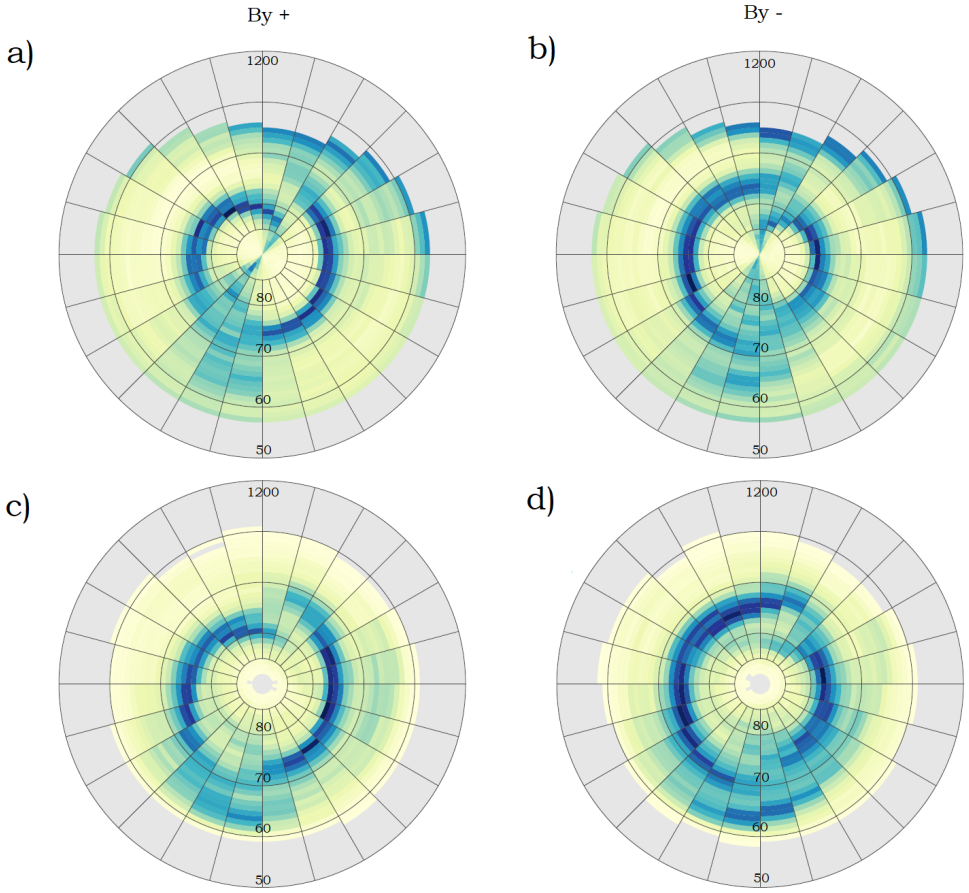

FIGURE 5.13: Distributions of CRB (top two) and CCB (bottom two) identifications for B_y positive (leftmost) and B_y negative (rightmost) over May 2000 - August 2002 (left). The plots show the result of all SuperDARN maps in the mentioned time periods with a minimum Heppner-Maynard latitude of 55°/The grey grid is centred on the magnetic pole and extends to 50 MLAT, noon is orientated to the top of the page and dusk to the left.

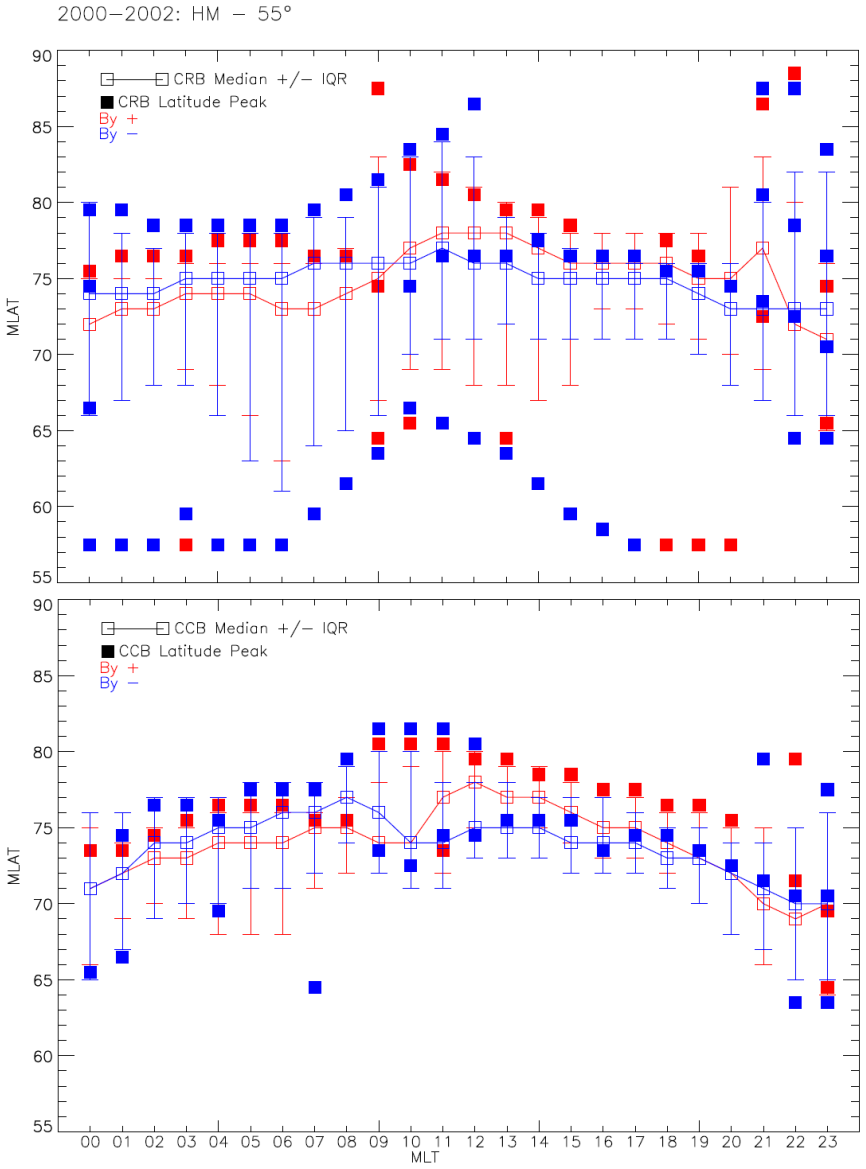

FIGURE 5.14: An MLT/MLAT plot for the CRB (top)/ CCB (bottom) showing the median and interquartile range for a minimum Heppner-Maynard boundary of 55° over May 2000- August 2002). The solid squares show the locations of clear manually identified peak occurrence latitudes.

exists again in the 09-11 MLT region but now the dawn region peak boundary latitude jumps from higher latitudes to lower latitudes at 11 MLT. Another difference to be noted is in the midnight region for the CCB IMF B_y- case. There is a clear low latitude dominant peak in boundary identifications that increases in latitude as it moves from 22 - 02 MLT. A low latitude population is also evident for the CCB IMF B_y+ case that extends from 21-01 MLT although this is not as clear as the B_y- case. The discontinuities associated with IMF B_y appear more physical for the CCB. In the noon region the discontinuity is $\sim 10^\circ$ compared to $\sim 20^\circ$ for the CRB. In the midnight region the CCB shows more clearly how the lower-latitude discontinuity evolves in MLT from the high-latitude one for the CCB, but just appears isolated for the CRB.

Figure 5.14, shows the median and IQR and is in the same format as figure 5.10 which is described earlier in this section. The top panel shows the CRB IMF B_y- and B_y+ results and the bottom panel the results for the CCB. For both techniques the median values for the B_y- are at higher latitudes at dawn and after the pre-noon sector (10 MLT) the median values become more equatorward than the B_y+ case. This relationship is also shown in the main boundary identification latitude regions shown as the solid blue and red squares between 75°-80°. In the pre-noon region at the location of the discontinuity the CRB has peak boundary latitudes that clearly extend up to very high latitudes (86°). For IMF B_y- this begins in the dawn region from 07 MLT and the peak boundary latitude gets gradually higher up to 12 MLT. For IMF B_y+ the peak boundary identification at high latitude begins at 10 MLT and gradually occurs more equatorward until 17 MLT. A similar asymmetry is evident for the CCB case although, the discontinuity at 80° at 10-12 MLT for both the IMF B_y+ and B_y- datasets is significantly narrower.

TABLE 5.5: The median and IQR for the CRB and CCB technique for IMF B_y+ and IMF B_y- in four key MLT regions. Values are taken from Figure 5.14

CRB					CCB				
	B_y+		B_y-			B_y+		B_y-	
MLT	Median	IQR	Median	IQR	MLT	Median	IQR	Median	IQR
05	74°	10°	75°	16°	05	74°	8°	75°	7°
11	78°	13°	77°	13°	11	77°	8°	74°	7°
17	76°	5°	75°	5°	17	75°	4°	74°	4°
23	71°	11°	73°	16°	23	70°	12°	70°	11°

Tables 5.5 summarises the median and IQR from figure 5.14 for the CCB and CRB IMF B_y+ and IMF B_y- in four key regions, dawn(05 MLT), pre-noon(11 MLT), dusk(17 MLT) and pre-midnight(23 MLT). The median values in the 05 MLT region show a 1° offset poleward for the IMF B_y- case and a corresponding 1° offset equatorward at 17 MLT. This is consistent with a duskward shift in the peak boundary identification latitudes for IMF B_y-. This agrees with statistical studies published by (*Bristow and Spaleta*, 2013; *Chen et al.*, 2015; *Koustov and Fiori*, 2016; *Chen and Heelis*, 2018) who found that on average their CRB identifications were shifted towards dusk for negative IMF B_y conditions.

The low latitude population at approximately 62° that was shown in the spatial distribution for the CCB technique (figure 5.13) was seen to be more prevalent in the IMF B_y- case. An interpretation of this is that these identifications close to the edge of the convection pattern and over 10° in latitude away from the main dawn and dusk peak boundary latitudes are associated with substorm-related flows. *Weimer* (1999) found that the Harang discontinuity becomes more pronounced during substorm times extending into the post midnight region, particularly for IMF B_y- . More recently, *Grocott et al.* (2010) showed that the nightside region can be heavily dependant on internal plasma processes (e.g. substorms) and that regardless of the IMF B_y an azimuthal extension of the dusk

cell is a key feature. An extension of the dusk cell could explain the low latitude boundary identifications and, as the IMF B_y- leads to the more pronounced configuration it could explain why the CCB identifications are more dominant in that case.

The median values at 11 MLT shown in Table 5.5 for the CCB shows a significantly higher value for IMF B_y+ than for IMF B_y-, this reflects the preference for boundary identifications to occur at lower latitudes here than for IMF B_y- as a result of the discontinuity. The CRB shows two relatively high median values (table 5.5) for both orientations of B_y, compared to other MLTs which highlights the preference for boundary identifications to occur at higher latitudes in the pre-noon region for both senses of B_y. The tendency for the CRB to identify boundaries at anomalous high latitude regions in the noon region was one of the motivating factors for developing a new identification technique.

Figures 5.15a-b and 5.16a-b show the distributions of the CRB and CCB boundary identifications specifically for the dayside region (06-18 MLT) for each sense of IMF B_y. Figure 5.15a-b shows the distribution for the CRB (5.15a) and CCB (5.15b) for IMF B_y+ and figure 5.16a-b shows the distribution for the CRB (5.16a) and CCB (5.16b) for IMF B_y-. For the IMF B_y+ case both the CRB and CCB show a preference for the peak latitude to decrease from 76° to lower latitudes from dawn around to the pre-noon sector. From dusk around to pre-noon the peak boundary latitude increases from 75° to higher latitudes. For the CRB technique (figure 5.15a) this clearly extends to much higher latitudes (85° at 10 MLT) than for the CCB case which stops at 80°. In addition, the CRB shows a very low latitude population at 10 MLT at 65°. This population has been shown in previous sections of this chapter and is attributed to un-physical boundaries

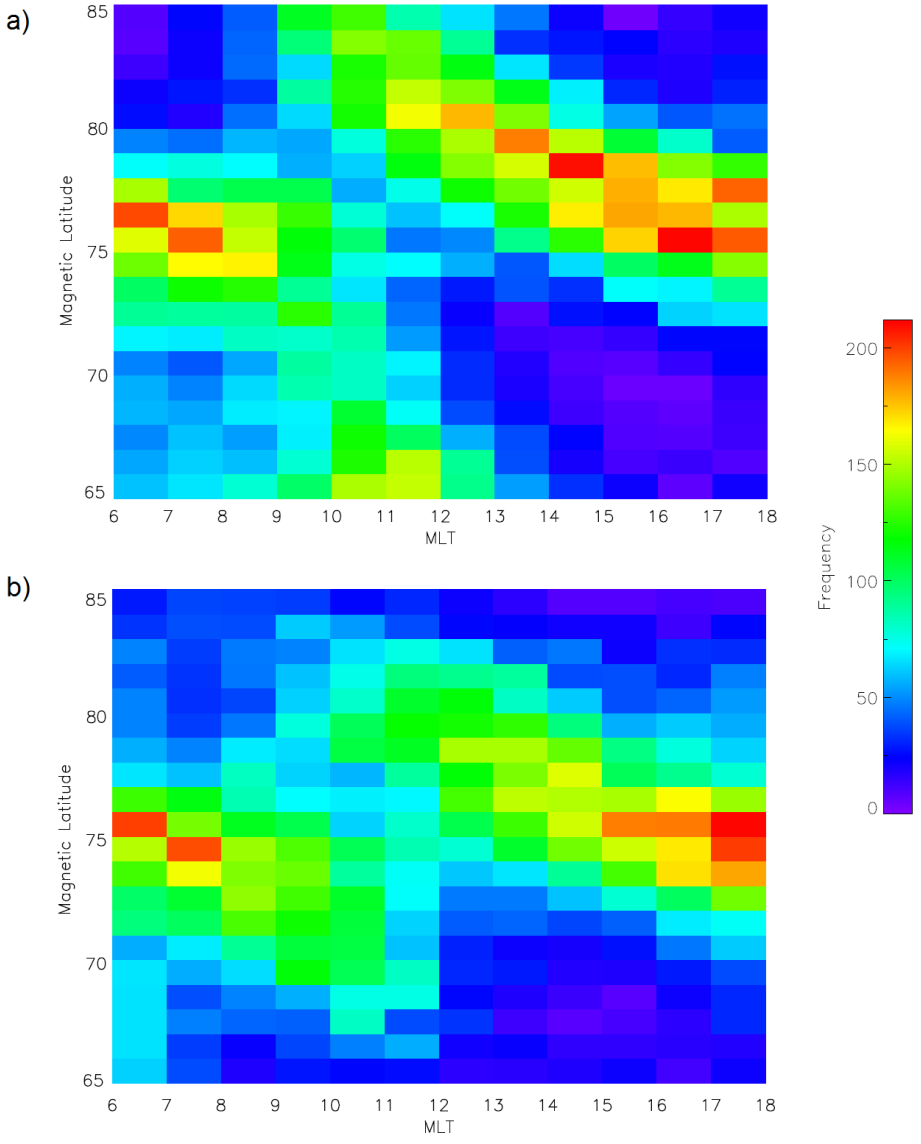

FIGURE 5.15: The occurrences of a) CRB and b) CCB boundary identifications binned by MLT over the dayside region and 1° MLAT for IMF B_y+

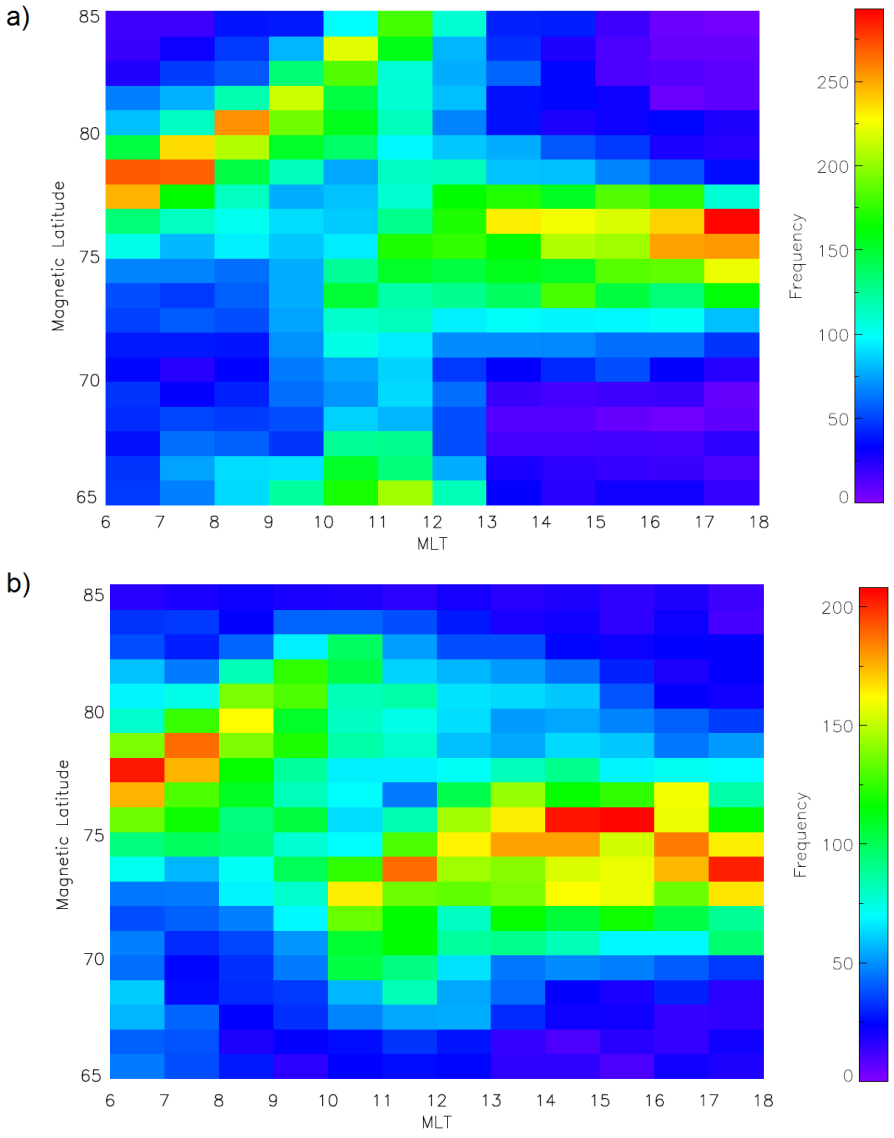

FIGURE 5.16: The occurrences of a) CRB and b) CCB boundary identifications binned by MLT over the dayside region and 1° MLAT for IMF B_y-

identified near to the edge of the convection pattern. For the IMF B_y- case (figure 5.16) from dawn through pre-noon the peak boundary identification moves to higher latitudes from 77° to 82° for the CRB. From dusk through noon the peak latitudes stay similar for the CRB, but the CCB shows some evidence of the peak latitudes moving to lower latitudes between 10-12 MLT. Again, the CRB shows the low-latitude population at very low latitudes at 12 MLT as for the IMF B_y+ case.

Given our understanding of the IMF B_y influence on the convection pattern then some asymmetry is also expected in the CCB/CRB for dominant IMF B_y conditions.This has been discussed in section 1.7 and referring to figure 1.13, if we look, for example, down the 12 MLT line in both cases there is a latitudinal offset between the dawn and dusk cell FACs. For IMF B_y+ the dawn cell FAC is farther equatorward than the dusk cell which corresponds to the results shown in Figure 5.15 where boundaries associated with the dusk cell occur at higher latitudes than those for the dawn cell. The opposite sense is also seen in our results for IMF B_y+ which agrees with the sketch. Peak boundary latitudes for IMF B_y+ and B_y- show CRB identifications across 11-12 MLT range over 84°-64°. The CCB, in comparison shows peak latitude identifications from 80°-76° which is much more consistent with the theoretical considerations by *Cowley et al.* (1991).

5.3 Summary

In this chapter a statistical comparison has been shown between the CRB and CCB techniques in order to assess their performance under a variety of conditions. The main results are summarised below:

The CRB and CCB both show a dominant peak in the identified boundary latitude at

dawn and dusk although the CRB tends to identify a significant portion of unphysical boundaries close to the edge of the convection pattern in the dawn and noon regions. The CRB dominant peak is offset 1° from the CRB in the dawn and dusk regions on average. In the pre-noon region the CRB predominantely identifies boundaries at high latitudes compared to the CCB. Over the midnight region there is a lot of variability for both techniques although the CRB is more likely to identify boundaries close to the pole. There is a large spread of boundary identifications that occur down to low-latitudes for both the CCB and CRB and this effect is seen over a wider portion extent of MLT for the CCB.

When results from 2000-2002 were compared to the 2010-2012 dataset the CRB and CCB values shifted poleward by 1° in the dawn and dusk regions, consistent with previous observations of the CRB (*Koustov and Fiori*, 2016). During this later period the latitudinal spread of boundary identifications became smaller at dawn and dusk for the CCB but the CRB showed an increase in the number of boundaries that were identified at the edge of the convection pattern.

As the minimum HMB increased by 10° the peak boundary latitude was shifted poleward by 3°-4° for both the CRB and CCB in the dawn and dusk regions. In the nightside region the CCB identified a clear peak in the boundary identifications at low latitudes which shifted poleward by 8° as the minimum HMB increased from HM:52°-62°.

When the IMF B_y effect was considered it was found that both techniques revealed a duskward shift of 1° for the B_y- case which is consistent with previous studies. A discontinuity is apparent in both techniques in the 10-12 MLT region. For IMF B_y- the pre-noon boundaries jump from higher to lower latitudes, with IMF B_y+ producing the opposite sense. It was found that the CRB observed discontinuities in this MLT region

that ranged from 65°-85°, whereas the CCB technique revealed a gap of 76°-80° which is more consistent with the expected location.

The CCB appears to be more robust than the CRB, which can be subject to un-physical boundaries which infiltrate the data. The CCB is more likely to identify a more physical boundary at most local times. In the next chapter we investigate this further by considering the relationship between the CCB and the poleward auroral boundary latitude (PALB) observed in global auroral imagery.

Chapter 6

Comparison of the CCB and CRB to the IMAGE Poleward Auroral Latitude Boundry

Determining proxies for the Open Closed Field line boundary (OCB) has spanned decades and countless studies using a multitude of different instruments have been published. *Vampola* (1971) found that solar electrons do not become stably trapped in high enough quantities on closed field lines. This leads to a sharp transition in the characteristics of particle populations in each magnetospheric domain which can be exploited with low altitude satellites. The DMSP mission has been used extensively over the last 25 years to investigate the properties of this transition region and determine characteristics of the OCB (*Makita et al.*, 1983; *Mishin et al.*, 1992; *Newell et al.*, 1991, 1996; *Sotirelis and Newell*, 2000; *Longden et al.*, 2010). Using a low-altitude satellite gives the best estimation of the OCB but is limited temporally and spatially as only instantaneous measurements at the location of the satellite can be taken.

Imaging satellites also offer a valuable dataset, especially if they are able to image the entire polar region for an extended period of time. The VIKING, POLAR and IMAGE

satellites have all been utilised to investigate and correlate the relationship of the location of the auroral oval with the OCB (*Brittnacher et al.*, 1999; *Kauristie et al.*, 1999; *Baker et al.*, 2000). Statistical correlations of the imaging satellites to a secondary dataset have been also been published and provide calibration offsets for more accurate results (*Carbary et al.*, 2003; *Boakes et al.*, 2008; *Longden et al.*, 2010; *Chisham*, 2017).

Ground based instruments can also be exploited to investigate the OCB, some of which have been identified in Chapter 5. For example, *Sotirelis et al.* (2005) found good correlation between the SuperDARN convection reversal boundary (CRB) and the OCB. Since then statistical studies using SuperDARN HF radar to determine the CRB have presented long term trends and response to various IMF parameters (*Bristow and Spaleta*, 2013; *Koustov and Fiori*, 2016; *Chen et al.*, 2015; *Chen and Heelis*, 2018). Although a clear benefit to using alternate datasets is the greater spatial and temporal coverage other studies that utilise HF radars have focused on specific MLT regions. For example, specific radar signatures such as the spectral width boundary, (SWB) can be used as a proxy to identify the post-noon and cusp region of the OCB (*Baker et al.*, 1995; *Chisham et al.*, 2001, 2002; *Chisham and Freeman*, 2003). Other ground based instruments include All-Sky Cameras (*Feldstein and Galperin*, 1985) to Meridian Scanning Photometers (e.g. *Blanchard et al.* (1995)).

Utilising ground-based datasets to determine an OCB proxy such as those mentioned above will require extracting information from the associated ionospheric convection. The global morphology is known to be highly sensitive to IMF control at any given time. An increasingly negative IMF B_z component for example, is well correlated with an increased rate of magnetic reconnection and enhancements in the size of the convection pattern. The presence of a significant IMF B_y component in the prevalent solar wind

modifies the preferred reconnection site and introduces asymmetries into the magnetospheric system (*Haaland et al.* (2017) and references within).

Ruohoniemi and Greenwald (1996, 2005); *Pettigrew et al.* (2010); *Thomas and Shepherd* (2018) have presented the climatological patterns of the convection using SuperDARN data for several clock angle dependencies. Due to the highly averaged nature of these patterns the convection morphology does not adequately capture the full response due to magnetotail processes. For example, work done by *Grocott et al.* (2017, 2010) presented statistical averages of the convection grouped by substorm MLT onset location. The dayside morphology followed the expected asymmetry according to the IMF clock angle but the nightside region was reordered according to the local time of substorm onset. This results in more complicated flows such as the 'double reversal' (*Grocott et al.*, 2010) that do not necessarily fit the more simplistic rounded and crescent cell (*Lockwood et al.*, 1990) . A technique that could not only infer the location of the OCB but secondary flows associated with geophysical phenomena would have a significant advantage over current techniques. This chapter aims to compare the automated SuperDARN CCB and CRB techniques with IMAGE FUV auroral images which are used as a verified proxy for the OCB (*Boakes et al.*, 2008; *Longden et al.*, 2010).

6.1 Methodology

6.1.1 Extracting the Poleward Auroral Latitude Boundary (PALB) using IMAGE SI12

All auroral images used in this analysis come from the IMAGE spacecraft providing global auroral data for comparison to SuperDARN boundaries from May 2000 until August 2002, a period during which significant time was spent imaging the northern hemisphere polar cap. Given that this chapter aims to validate a new boundary extraction technique at all magnetic local times, the SI12 instrument is used in analysis as, although not as high resolution as WIC, is less susceptible from the effects of dayglow. The Poleward Auroral Boundary Latitude (PALB) is determined using the method described by *Longden et al.* (2010).

The Si12 images are transformed into an altitude adjusted corrected geomagnetic coordinate system (AACGM) to be consistent with ionospheric convection data and so direct comparisons with SuperDARN are possible. Average emission intensity profiles in bins of 1° magnetic latitude and 1 hour of magnetic local time with a latitude range covering 50° - 90° are constructed from the auroral images. The technique models these latitudinal profiles per MLT sector as one of two options. 1) a single gaussian function with a quadratic background or 2) two gaussian functions with a quadratic component. The latter gives a better estimate of the PALB in the case the oval shows bifurcations, as is the case for 35% of the profiles in the nightside MLT region. For a single gaussian the PALB is located poleward of the gaussian peak by the full width half maximum (FWHM), this is also the method used in similar studies from *Carbary et al.* (2003) and

Boakes et al. (2008). If the double gaussian provides the better fit then the PALB is located poleward by the FWHM as before but taken from the most poleward gaussian peak.

There are some further quality checks imposed on the data and PALB locations associated with a poor fit or incomplete data are disregarded. This gives auroral boundary latitudes for all hours of MLT where the luminosity profile can be sufficiently determined. The method is described in full with complete justifications in *Longden et al.* (2010).

A final step is to adjust the PALB at certain MLTs to account for systematic offsets that arise as a result of the instrumentation. The particle precipitation boundaries (PPB) extracted from low-altitude spacecraft such as DMSP is thought to provide the closest approximation to the OCB. Both *Carbary et al.* (2003) and *Boakes et al.* (2008) noticed systematic latitudinal offsets in their statistical studies comparing Polar UVI/ IMAGE FUV with DMSP data. To combat this they both calculated adjustments for all MLT regions by minimising the errors in statistical comparisons of DMSP PPB and the auroral images. *Longden et al.* (2010) follows a similar procedure and provides calibration for each hour of MLT for each IMAGE satellite instrument.

Figure 6.1a and 6.1b present two example images taken over the Northern Hemisphere using the SI13 instrument onboard IMAGE. The first image is taken on 6 December 2000 02:38 UT and the second on 28 October 2001 09:17 UT. The yellow squares show the resultant PALB locations identified using the *Longden et al.* (2010) method for a) a smaller, quiet time oval and b) an active, higher intensity oval. The overlayed red symbols show the result of the PALB after the aforementioned corrections have been applied.

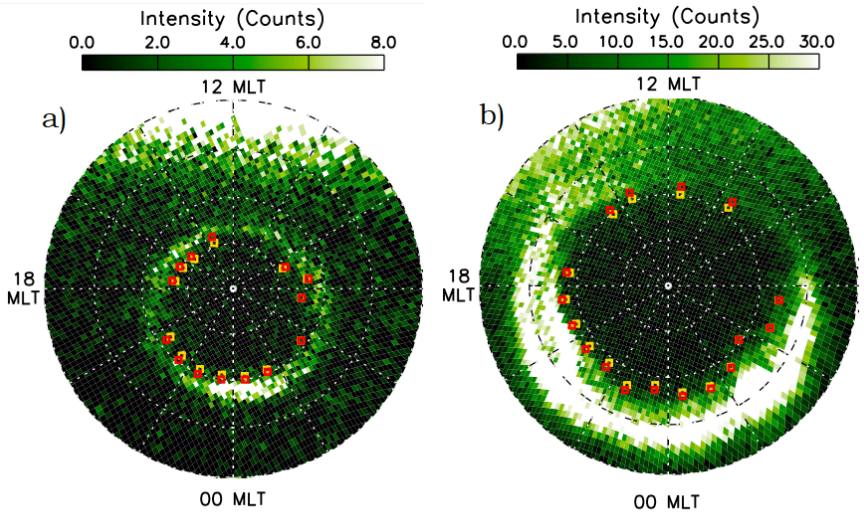

FIGURE 6.1: Taken from Figure 2 of *Chisham* (2017) a) shows SI13 images from 02:38 UT on 6 December 2000, b) data from 09:17 UT on 28 October 2001. The yellow square symbols represent poleward auroral luminosity boundary (PALB) estimates determined from the IMAGEFUV SI13 images at a 1 h MLT resolution. The red square symbols represent the corrected locations of these PALB estimates using the corrections outlined in *Longden et al.* (2010)

6.1.2 Extracting the CCB and CRB from SuperDARN

SuperDARN data over May 2000 to August 2002 is available at two-minute cadence, however only times containing at least one SI12 IMAGE PABL can be used for analysis. The CRB and CCB boundaries with corresponding auroral data are extracted using the methods and justifications outlined in chapter 4. As part of this chapter involves investigating multiple boundary identifications for the CCB and CRB it makes more sense to isolate the analysis to each hour of MLT and assess the performance separately. Characterisation of the relationship of double or more boundary identifications and their location relative to the PALB will help make conclusions about their origin.

6.1.3 Considerations on data coverage

An important consideration to discuss is the location and global coverage of direct radar observations. A common threshold when using SuperDARN global convection maps in statistical studies is to demand at least 200 data points to ensure the map is data-driven e.g. (*Imber et al.*, 2013). This however, puts no emphasis on the distribution of data points over the MLT/ MLAT plane. Previous studies e.g. (*Bristow and Spaleta*, 2013) limited their extraction of the CRB to hours of MLT where there were sufficient direct radar observations poleward and equatorward of the identified boundary. It has been a conscious choice in Chapter 5 to put no such criteria on the location and quantity of radar backscatter. This allowed an assessment on the performance of the boundary techniques on the ECLAT database of modelled ionospheric convection patterns as a whole. As was found in Chapter 5, additional boundary identifications at un-physical MLT/MLAT locations are a common feature. This is particularly the case for the CRB and presented case studies highlighted that this can arise in areas of poor fitting, usually where there is an absence of direct radar observations. A secondary aim for this chapter is to investigate the amount of local coverage in each MLT region and to see if there is any improvement in the correlation between the SuperDARN boundary and the PALB. A secondary aim for this chapter is to investigate the amount of local coverage in each MLT region and to see if there is any improvement in the correlation between the SuperDARN boundary and the PALB.

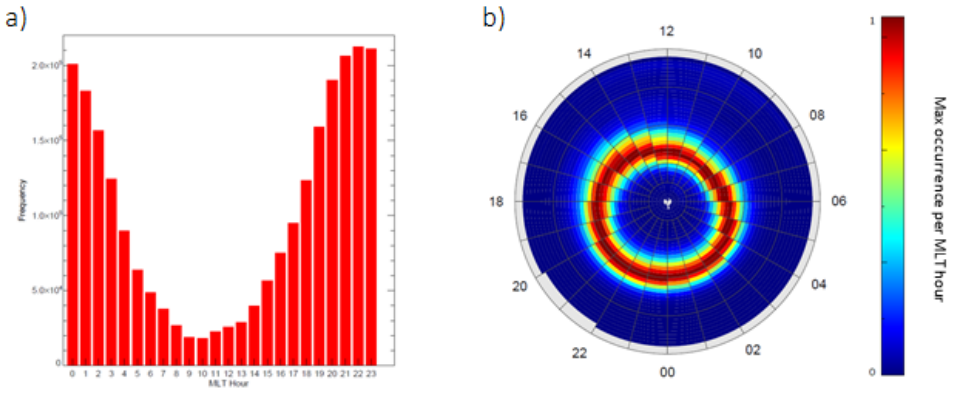

FIGURE 6.2: a) The frequency of PALB IMAGE FUV SI12 observations in each MLT bin from May 2000 - August 2002. b) A polar plot in AACGM geomagnetic coordinates centered on the magnetic pole and extending to 50°. Noon is orientated to the top of the plot and dusk to the left. The distribution of the PALB identifications shown in a) by latitude. The blue to red colour scale represents increasing occurrences of PALB locations and each MLT hour is scaled independently to its maximum occurrence.

6.2 Overview of the auroral boundary data

CCB identifications extracted from SuperDARN convection maps and IMAGE auroral data are compared during the period May 2000 to August 2002. During this time a total of 394,082 viable images of the northern hemisphere polar cap are taken. The occurrence of auroral boundaries extracted using the *Longden et al.* (2010) method per MLT sector is shown in figure 6.2a. A clear observational bias in the IMAGE auroral boundary data occurs as a direct result of dayglow obscuring observations towards noon. The IMAGE detectors are able to image the nightside auroral oval much more frequently than the dayside. The number of observations towards noon are an order of magnitude lower than those towards midnight. As boundaries in each MLT sector are compared this will have an implication on the reliability of a statistical result in the dayside region.

Figure 6.2 b) shows the distribution of PALBs identified using the IMAGE SI12 instrument in the MLT/MLAT plane to show the average PALB locations over the analysis

time period. Due to the observational bias of PALB identifications in each MLT sector, each hour of MLT is colour-scaled individually according to the highest frequency in that region. This was done so that the average distributions can be clearly identified by eye. The average position of the PALB follows an approximate circle shape offset towards midnight and dusk, as is consistent with observations and circle fitting technique of *Milan et al.* (2009b). The highest incidence of observations over the nightside region (20-03 MLT) is at 70° MLAT up to 76° between (11-13 MLT).

6.3 Statistical comparison of CCB and CRB identifications to the PALB

In this section CCB and CRB identifications are compared to corresponding IMAGE PALB identifications extracted using the method outlined by *Longden et al.* (2010) in order to evaluate its performance as a proxy for the OCB. At present no constraint has been imposed on the quality of a given SuperDARN map and as such all maps with boundary identification(s) that have a corresponding IMAGE PALB identification are used in the analysis. Each hour of MLT is treated independently, which means that recorded offset latitudes (CCB(CRB) MLAT, PALB MLAT) in each sector come from a different total number and combination of SuperDARN maps. Note that positive offsets are associated with a boundary identification that occurs poleward of the PALB.

6.3.1 Single CCB and CRB boundary identifications

In the first instance only MLT hours that observe a single CCB or CRB are identified. Figure 6.3 shows the distribution of (CCB-PALB) offsets in one hour of MLT and 1° latitude bins. As each hour of MLT is treated independently the colour scale is normalised in each MLT sector to clearly see peaks in the distribution. The median and Interquartile Range (IQR) for each bin is plotted over each distribution and the black dashed line at 0° highlights the zero offset line where the CCB is aligned with the PALB. Figure 6.4 shows a plot in the same format as described above but shows the MLT-MLAT distribution for the (CRB-PALB) offsets.

This section will first describe the main features of the (CCB-PALB) offset distributions followed by a description for the (CRB-PALB) offsets. The relationship of the offsets to their global and local radar coverage will also be examined. Figure 6.3 shows normal distributions centred on a peak offset latitude for almost all hours of MLT (except those between 10-12 MLT). This indicates that the median and IQR can adequately characterise the peak offset latitude and corresponding spread. The median value of the CCB is located poleward of the PALB for all magnetic local times. The furthest deviations occur between 02-04 MLT with a peak offset of 3° and between 15-19 MLT with a peak offset of 4°. The best agreement with the PALB occurs in the nightside region between 22-00 MLT with an poleward offset of 1°.

This result seems unusual as the dawn and dusk regions show the least agreement when these areas, associated with strong flow shear should theoretically be the easiest to identify. *Sotirelis et al.* (2005) performed a statistical analysis comparing the SuperDARN CRB to DMSP PALB identifications. They found an equatorward offset at midnight

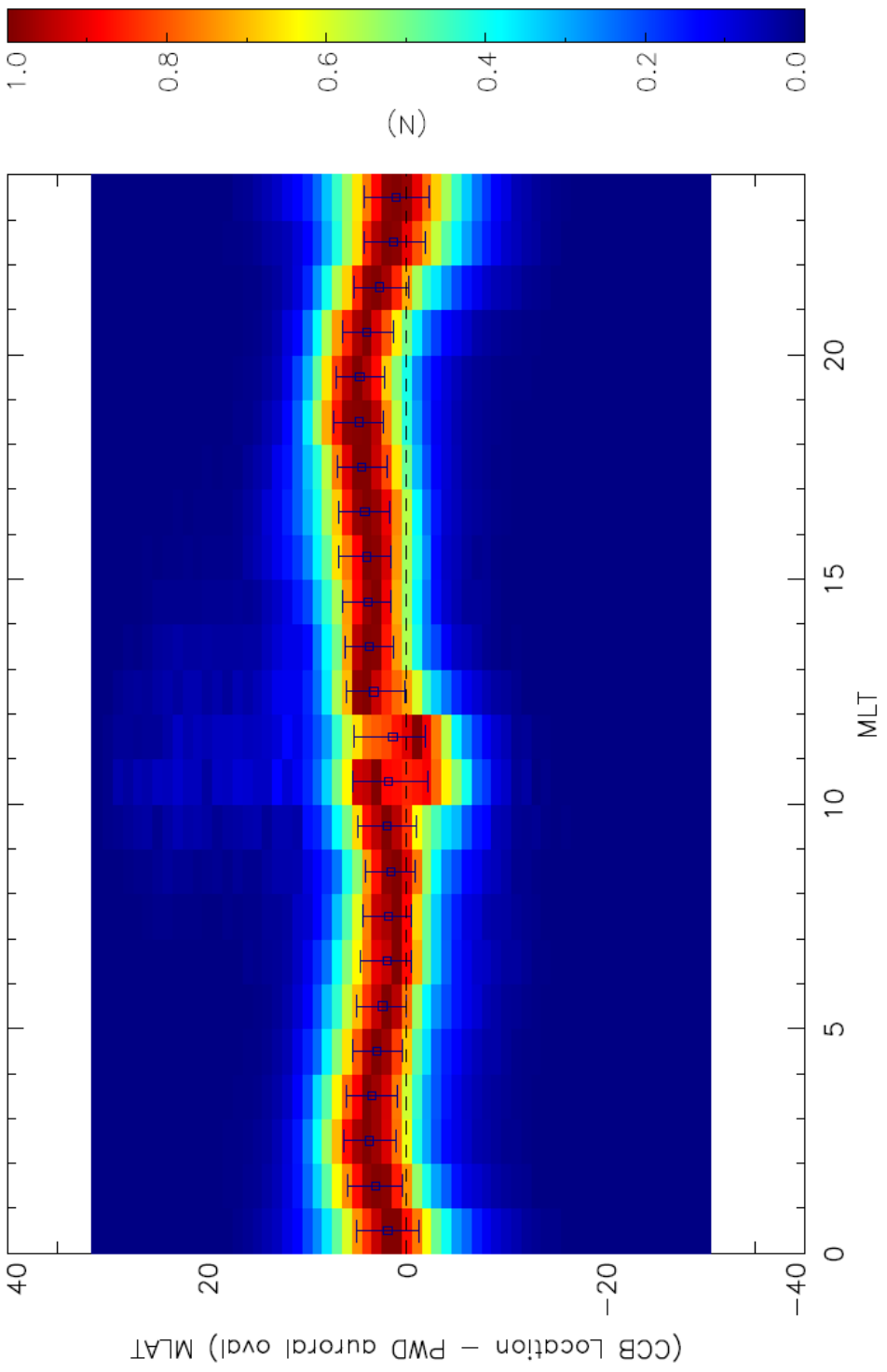

FIGURE 6.3: The distribution of the (CCB-PALB) MLAT boundary identification offsets for single CCB identifications in a given MLT hour.Each hour MLT is colour-scaled relative to the maximum occurrence in that bin. The median and IQR are overplotted in black.

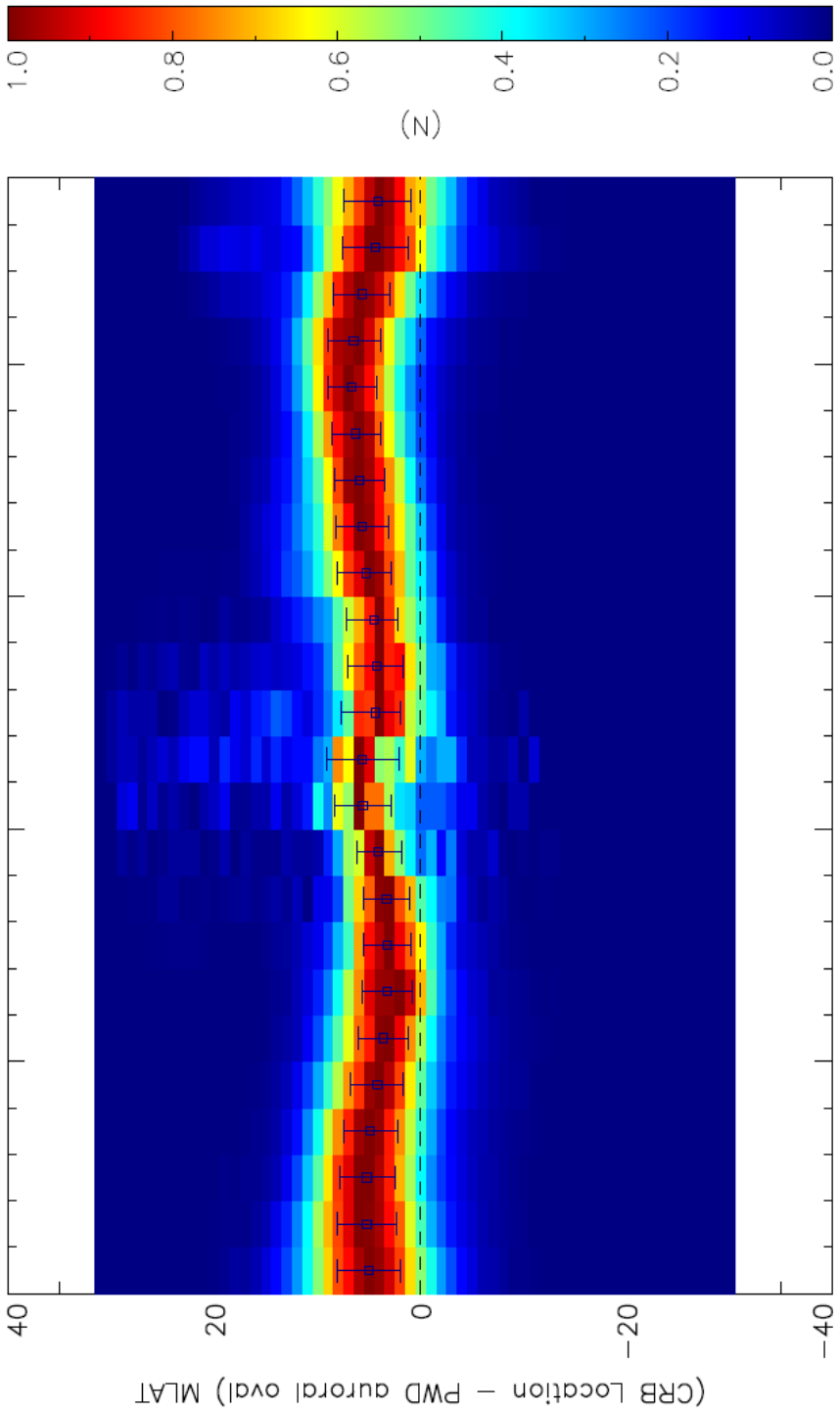

FIGURE 6.4: The distribution of the (CRB-PALB) MLAT boundary identification offsets for single CRB identifications in a given MLT hour.Each hour MLT is colour-scaled relative to the maximum occurrence in that bin. The median and IQR are overplotted in black.

varying from 0° at noon to 1° at dawn and dusk. The 1° equatorward offset at dawn/-dusk was attributed to a small viscous-like interaction region between the magnetosheath and low-latitude boundary layer. They found the best correlation between 16 - 20 MLT with the worst at 00-04 MLT. Results from Chapter 5 have shown that the CRB performs similarly to the CCB at dawn and dusk, so it may be expected to exhibit a similar correlation in this dataset. However, in contrast to those findings Figure 6.3 shows that the worst performance for single CCB identifications is between 15-19 MLT although the 02-04 MLT region also shows considerable deviations which is similar to *Sotirelis et al.* (2005).

Figure 6.4 shows the MLT/MLAT distributions for the (CRB-PALB) offsets. The median values across all MLT are offset even farther poleward than for the CCB identifications. Again, the post-midnight (01-04 MLT) and dusk (16-20 MLT) regions show some of the largest offsets from the PALB with deviations of 5° and 7° respectively. Across the pre-noon region (09-11 MLT) the behaviour of the CRB is quite different to that of the CCB. There are sporadic occurrences of (CRB-PALB) offsets spread over a large latitudinal area, from $-15°$ to 30°. The IQR is correspondingly large in this region, particularly for 11-12 MLT. The median value is shown to deviate further poleward,from 3° at 09 to 6° at 11 MLT. In the noon region this poleward offset of the (CRB-PALB) is expected as the CRB technique tends to identify boundaries at high latitudes due to the east-west reversal being less well defined here. This has been shown in the statistical analysis in chapter 5 and also previous studies (e.g. *Koustov and Fiori* (2016)).

Figures 6.5a-b show the distribution of the global radar coverage for the SuperDARN maps which contribute to the (CCB or CRB)-PALB offset measurement in each MLT sector. Even though the offset measurement is confined to one hour of MLT, the global

contribution of radar coverage will ultimately affect the reliability of the entire map making it a useful consideration. The darker colour shows a higher proportion of maps observing a given number of radar measurements over the entire map for each hour of MLT. Each MLT is again, treated independently and colour-scaled relative to the maximum occurrence in that bin. The number of radar measurements over the map is binned in a size of 25 measurements. The black crosses over plotted show the median value to give a quantative representation of the average coverage at each MLT. The black dashed line overpotted is the average of the median values in an effort to quantify the overall level of global coverage for single CCB and CRB identifications. Figure 6.5a shows the distribution for the CCB technique. The median value is highest from 04-08 MLT but all values follow a similar line centred on approximately 325 radar measurements. The spread about the median is clearly not normal as there are a significantly high population of maps for all MLTs grouped together with global measurements of less than 300. Figure 6.5b shows the distribution for the CRB technique. In this case the average of the median values is shifted a little higher to 375 radar measurements however, this is due to a significant shift in the median values over the 09-14 MLT region due to a wide range of different coverage levels being observed. It is worth noting that the probability of a CRB identifying a single boundary in the 09-14 MLT bins is only 30% (As shown in figure 5.5 in chapter 5), this and the limited auroral observations in these regions means that there are fewer data points in these bins. As with the CCB, there are a high population of maps over the other MLT sectors with global measurements of less than 200 radar measurements.

These poleward offsets of the CCB and CRB are likely to be related to the overall data

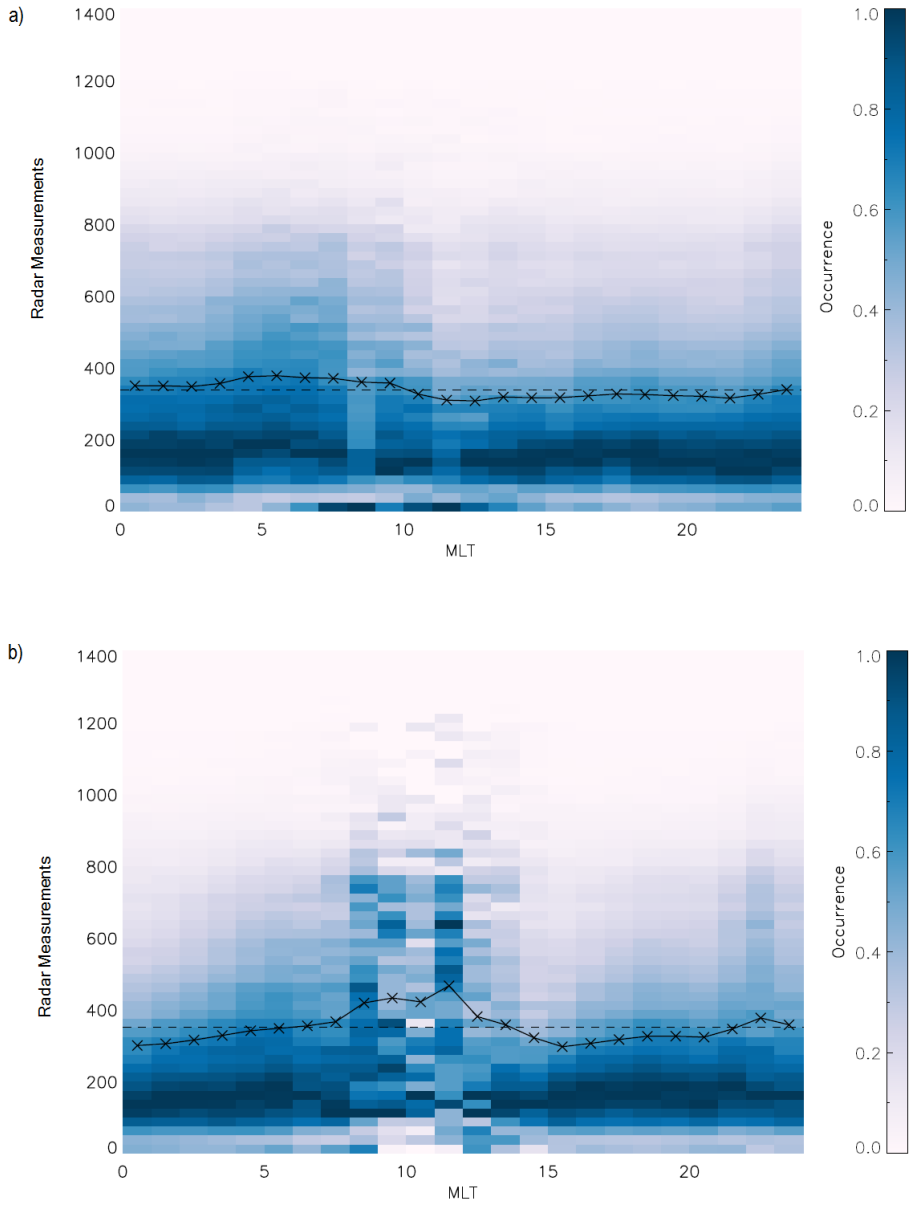

FIGURE 6.5: The distribution of the global level of radar coverage for each contributing SuperDARN map to each hour of MLT for a) the CCB and b) the CRB

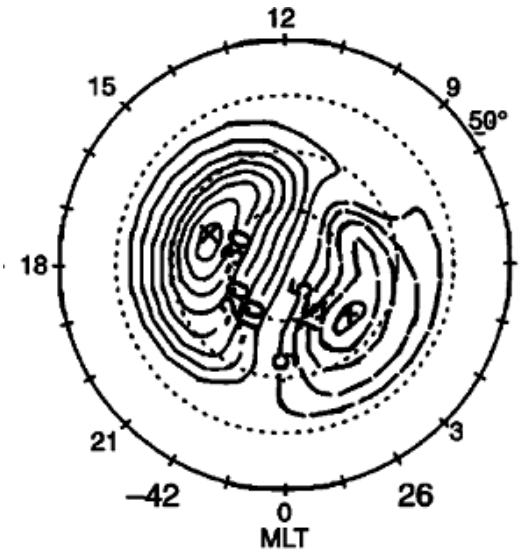

FIGURE 6.6: The statistical pattern of the ionospheric convection for the IMF B_z negative condition for moderate solar wind driving taken from *Ruohoniemi and Greenwald* (1996)

coverage and the quality of the maps used in the analysis. The map potential fitting algorithm described in Chapter 3 utilises any available line of sight radar observations and provides a global estimate based on these measurements. If there are no available line of sight measurements, then the data is supplemented by a background statistical model based on the IMF orientation at the time of the radar scan. The SuperDARN data used here uses the statistical convection patterns presented in *Ruohoniemi and Greenwald* (1996) (RG96). An example showing the average convection pattern with data taken from the Goose Bay radar from 1987-1993 for 4nT $< B_t <$ 6nT is shown in Figure 6.6.

The map is centred on the AACGM pole and extends to 50° MLAT, the dashed circles represent the magnetic latitude in increments of 10°. The solid black curves represent the ionospheric equipotentials in intervals of 5 kV. The two crosses mark the area of highest and lowest potential and can be referred to as the foci of the map (17 and 03

MLT). This average pattern is generated with moderate IMF driving for predominantly IMF $B_z < 0$ and is shown as a 'typical' background model example to the SuperDARN data. As shown in figure 6.6, the average location of the foci according to the 'typical' case statistical model would occur somewhere close to 75°. The foci should ideally represent a clear separator between sunward and anti-sunward flow and coincide with a CCB or CRB boundary. The average location of the PALB (as shown in figure 6.2) in the 17 and 03 MLT bins is 72° i.e. equatorward of the RG96 flow reversal. If a significant portion of SuperDARN maps contain insufficient data to accurately reflect the extent of the convection pattern they will be dominated by the RG96 model and so then a poleward offset from the PALB could be expected. The CCB-PALB offsets in the 17 and 03 MLT sectors shown in Figure 6.3 revealed poleward offsets of 3°-4° which is consistent with the RG96 model. The (CRB-PALB) offsets show a poleward deviation of 5° and 7° for the 17 and 03 MLT bins which is more than would be expected if the deviation was only due to maps converging on the background statistical model. In the statistical analysis undertaken in chapter 5 it was shown that the CRB tends to identify boundaries 1° higher than the CCB on average. This could account for some of the offset from the PALB. Another factor could be CRB identifications occuring at higher latitudes, close to the pole that contribute to the dataset and skew the median value slightly more polewards from the PALB. This is more likely to affect the CRB as it frequently identify kinks close to the pole due to 'wavy' contours from the cross polar cap flow and the fact that the east-west reversal becomes less defined close to 90° MLAT. In the midnight region the (CCB-PALB) offset was shown to have the closest correlation with the PALB, however, it also has the largest IQR and spread about the median than at other MLTs. This suggests that there is still considerable variability here. If the

above interpretation of an underestimate of extent of the SuperDARN convection is to be accepted then this would imply the midnight region should also show a significant poleward offset. The pre-midnight to midnight region is associated with the Harang Discontinuity (HD) (*Heppner and Maynard*, 1987; *Harang*, 1946); a velocity shear zone in the auroral ionosphere. It is a permanent feature of the high latitude convection creating an extended dusk cell across the 22-00 MLT region and is closely related to the development of substorms (*Koskinen and Pulkkinen*, 1995) . Identifications associated with the HD and possible substorm related flows which tend to occur equatorward of the PALB would thus more closely align with the auroral boundary if the SuperDARN convection pattern was underestimated.

The global coverage showed that 50% of the maps used in the interval had less than 300 radar measurements, with many less than 200. Using maps with at least 200 observations globally is often used as a basic threshold of map quality (e.g. *Imber et al.* (2013)). The significant portion of data with less than 200 radar points is consistent with a map defaulting to the background model.

The latitudinal coverage of the radars during 2000-2002 may also impact the accuracy of the modelled ionospheric convection. *Thomas and Shepherd* (2018) presented a new statistical model derived from a complete network of low-latitude, mid-latitude and polar radars over 2010-2016. This study found that during strong solar wind driving the addition of the polar and low-latitude radars (not available for the time interval for this analysis) increased the measured cross-polar cap potential (CPCP) by 40%. A more recent study by *Mori et al.* (2012) compared SuperDARN radar velocities to ionosonde data and found that the separation between the foci of the large-scale convection pattern is often underestimated. A combination of the SuperDARN modelled ionospheric

convection defaulting to the background statistical model and underestimation of the large-scale pattern from the latitudinal coverage of the network is consistent with a poleward offset from the PALB in the dawn and dusk region.

The level of global coverage can be a useful tool as an initial check to quantify the level of data in a SuperDARN map but it does not tell the whole story. It is possible for a map to have poor global coverage but to contain smaller areas with sufficient data for the map potential model to adequately capture the convective flows. The next section will show how the (CCB and CRB)-PALB offsets vary with increasing amounts of local data coverage.

6.3.2 Effect of local radar coverage on the (CCB and CRB)-PALB offsets

The (CCB-PALB) and (CRB-PALB) offset distributions are plotted for increasing levels of local radar data coverage. The local coverage is defined here as the number of radar observations in the MLT hour. Figures 6.7a-b and 6.8a-b show two example MLTs (07 and 11) that reveal more about the radar coverage dependence of the CCB/CRB and highlights differing behaviour between the two. The overall trends at other MLTs will be presented after. Figure 6.7 shows the result at 07 MLT for the CCB (6.7a) and CRB (6.7b). The x-axis is binned every 5 radar observations but note that the 0-1 radar observation bin is left intentionally off this plot due to the significantly high number of maps that contained no radar measurements. When this bin was included it made it difficult to see any trends in the data as the occurrences were an order of magnitude higher. The y-axis is binned in 1° MLAT offsets. The black crosses are plotted to show

the median value and the straight black line shows the line of best fit through the data points.

For both the CCB and CRB poleward offsets can be seen when there is little radar coverage. For 1-4 radar measurements, the CCB is on average, offset 2° compared to 4° for the CRB. Large offsets are also possible in this coverage bin with the CCB showing occurrences offset +/-15° from the PALB. These large offsets are also seen for the CRB but these tend to be concentrated poleward of the PALB, which implies that if the CRB identifies a single boundary in the MLT region it is more likely to show a poleward offset from the CRB. Interestingly as the amount of local coverage increases the median (CCB-PALB) and (CRB-PALB) offsets tend to shift towards the PALB and the spread about the median reduces. At approximately 60 radar measurements in the MLT hour the offset median value for the (CCB-PALB) reduces to the PALB. The (CRB-PALB) offset median reduces by approximately 2° and converges towards the PALB.

Results in chapter 5 have shown that the CRB and CCB exhibit different behaviour in the pre-noon region and this is also reflected by the distributions shown in Figure 6.8a-b. In the top panel (6.8a) the CCB median is closely aligned with the PALB for all levels of radar coverage. A slight equatorward shift of the (CCB-PALB) median offset is visible up to 25 radar measurements, after this there are very few observations so the medians shown after this bin do not carry much statistical weight. Again, large offsets are possible in this MLT region however, the large deviations from the PALB tend to be located poleward as opposed to the 07 MLT where they occurred both poleward and equatorward. In contrast to the CCB, the (CRB-PALB) median offsets show the opposite trend and tends to shift farther poleward of the PALB, in addition there are

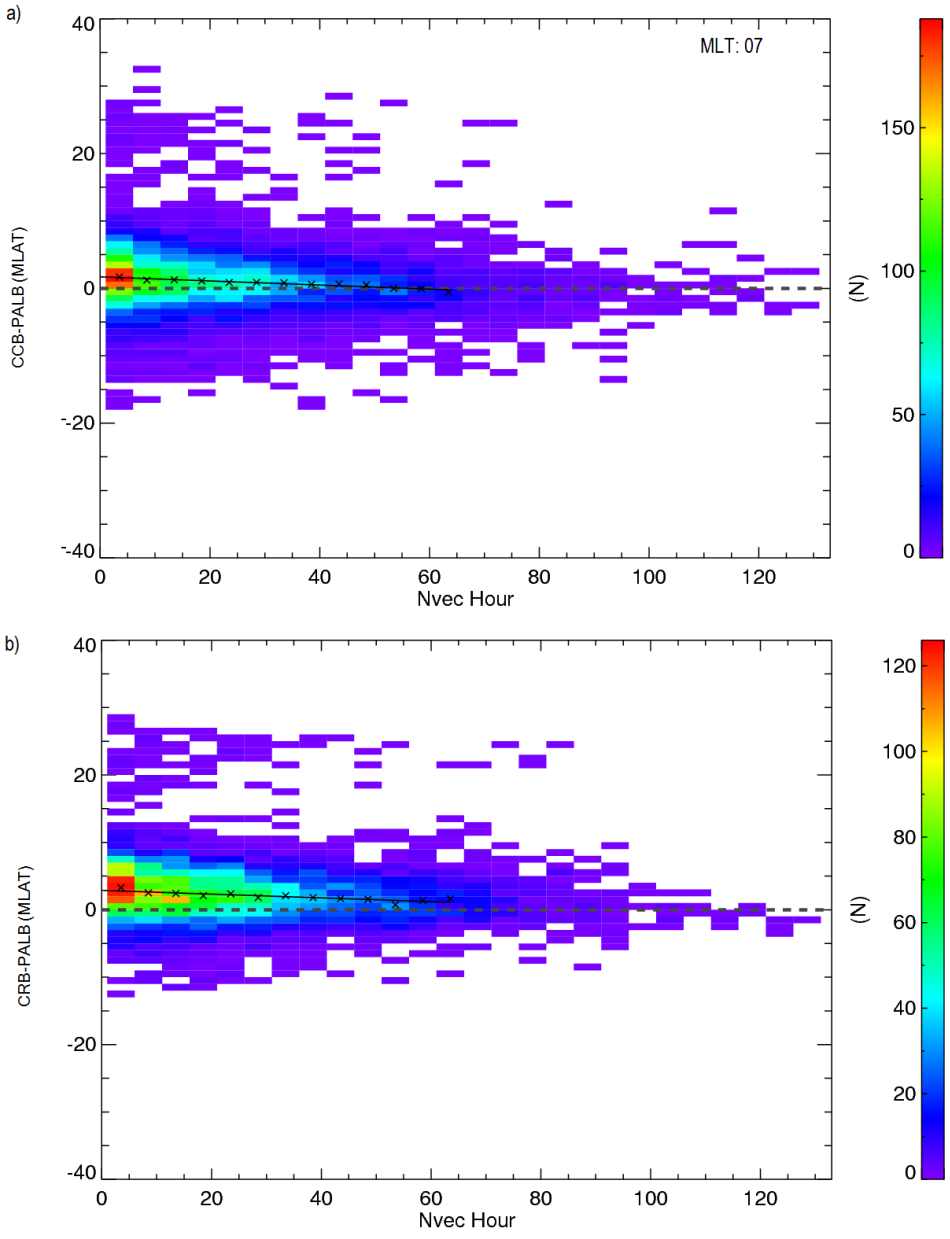

FIGURE 6.7: The a) (CCB-PALB) and b) (CRB-PALB) offset distributions at 07 MLT for increasing levels of local radar data coverage. The local coverage, binned in 1° MLAT and 5 radar measurements. The black dashed line shows the zero-offset line, the black crosses show the median value and the straight black line is the line of best fit plotted through the medians

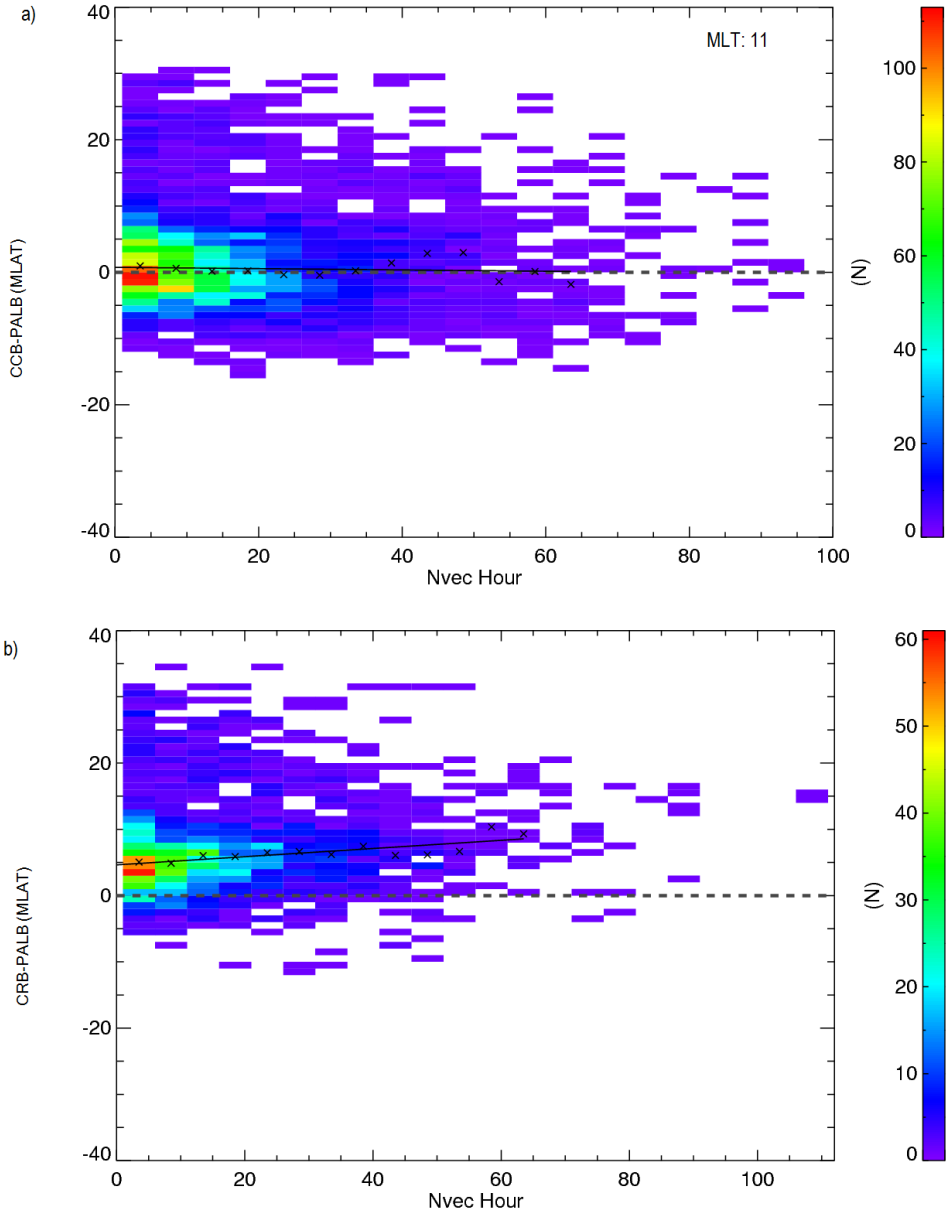

FIGURE 6.8: The a) (CCB-PALB) and b) (CRB-PALB) offset distributions at 11 MLT for increasing levels of local radar data coverage. The local coverage, binned in 1° MLAT and 5 radar measurements. The black dashed line shows the zero-offset line, the black crosses show the median value and the straight black line is the line of best fit plotted through the medians

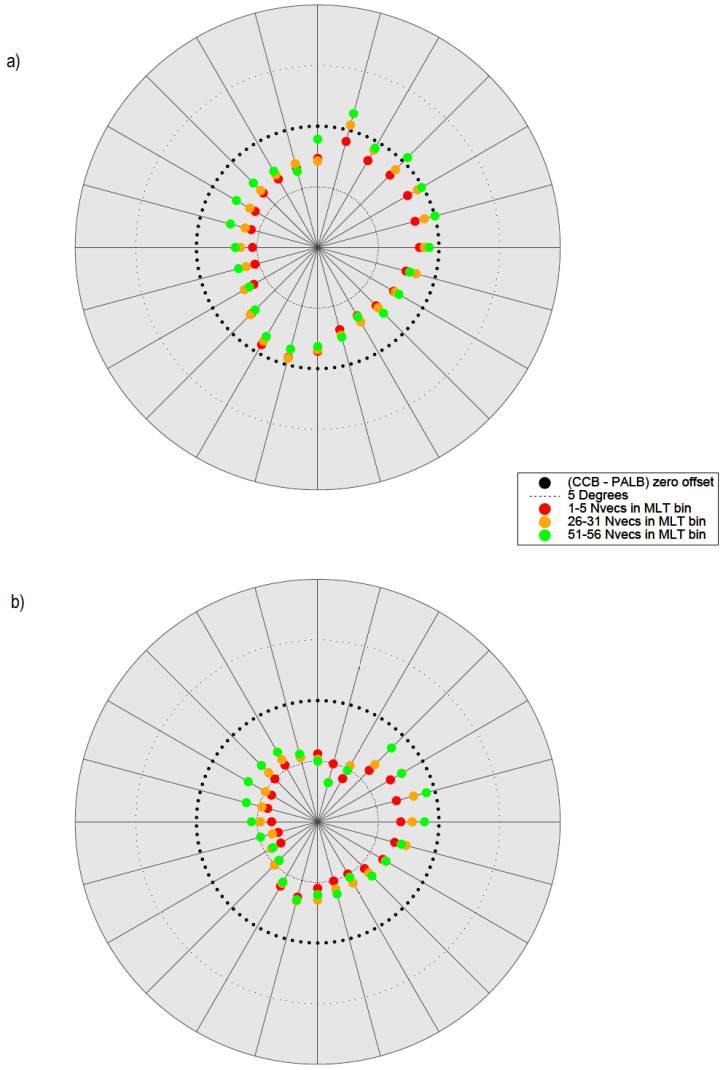

FIGURE 6.9: The plots are presented in a polar grid with the largest black dots showing a zero offset to the PALB. The solid lines directed radially outward separate the MLT hours and the small dots show a 5° offset to the PALB. For each hour of MLT the median value at 1-5 (red), 26-31 (orange) and 51-56 (green) are overplotted for a) the (CCB-PALB) and b) the (CRB-PALB)

very few boundary identifications made equatorward of the PALB.

To show the result of the general trends across all MLT regions the (CCB or CRB) offset median values at three radar coverage levels are plotted in Figure 6.9a-b. A 'good' level of radar coverage was chosen as 51-56 measurements in a given MLT bin as figure 6.7 showed that for the CCB in this bin the median offset converged to the PALB. The lowest level of coverage is the 1-5 measurement bin and a middle value of 26-31 was chosen as a medium level of coverage. The plots are presented in a polar grid with the largest black dots showing a zero offset to the PALB. The solid lines directed radially outward separate the MLT hours and the small dots show a 5° offset to the PALB. For each hour of MLT the median value at 1-5 (red), 26-31 (orange) and 51-56 (green) are overplotted, if the median is shown above the large black dots towards the centre of the plot this means the median value is offset polewards from the PALB.

Figure 6.9a shows the result for the (CCB-PALB) median offsets and 6.9b the result for the (CRB-PALB). From 06-10 MLT and 02-05 MLT both techniques show that increasing the amount of local radar coverage improves the correlation with the PALB. For the CCB increasing the local radar data coverage to 51-56 measurements in the 06-10 MLT region shows close alignment to the PALB. Although increasing the radar data coverage in the 02-05 MLT region improves the offset there is still a polewards shift of 2°. The (CRB-PALB) median offsets are still consistently poleward despite the improvement made by the local coverage in the previously mentioned MLT regions. Figure 6.8a-b showed that the CRB and CCB revealed opposite trends at 11 MLT. Figure 6.9 shows that this is typical behaviour of both techniques over the pre-noon region with increasing data coverage improving the CCB-PALB relationship but worsening it in the

CRB-PALB case. At 51-56 vectors in the MLT bin the CCB and CRB median offsets can separated up to 7°. In the midnight region the addition of more radar measurements does not seem to have an effect on the (CCB-PALB) or (CRB-PALB) median offsets. In the dawn and dusk regions single boundary identifications could be expected as the sunward and anti-sunward flow creates a clearly defined boundary. Increasing the local radar coverage in these regions could explain why they tend towards the PALB. In the previous section the poleward offsets at dawn and dusk were attributed to the under-estimation of the convection pattern due to low amounts of data coverage. Increasing the coverage in these regions could explain why CRB and CCB identified boundaries tend converge on the PALB as the SuperDARN maps become more data driven and less reliant on the background statistical model. This does imply that the local coverage can have a significant impact on the quality of the SuperDARN map. In this case 55 measurements alone in one hour of MLT are required for the CCB SuperDARN boundary to converge on the PALB at any MLT, although we note that they do not converge at all MLTs for even the highest data coverage. A global limit of 200 with no geometric criteria on the radar measurement may be insufficient to fully capture the convection morphology. The nightside regions do not seem to respond to the increase in data coverage, this could be attributed to the ionospheric flows in the nightside being more compicated e.g. (*Grocott et al.*, 2010, 2017) implying that there is not a simple relationship to radar coverage. Overall the plots in this section have shown that single identification boundaries identified with the CCB technique show closer alignment than the CRB to the PALB.

6.3.3 CCB and CRB boundary identifications

The next data presentation shows a similar analysis but for intervals where two boundaries are identified by the CCB and CRB techniques in a given MLT bin. Figures 6.10a-b and 6.11a-b show four plots in the same format as in the previous section with the distribution of (CCB or CRB)-PALB MLAT offsets shown per MLT. The top panel in each case shows the distributions for the poleward offset and the bottom the equatorward offset. The median, IQR and 0° MLAT offset line are over plotted.

For the poleward identified (CCB-PALB) offset, between 01-03 MLT and 17-20 MLT the median is the farthest offset from the PALB and by 8° MLAT. The closest agreement occurs between 09-13 MLT over the noon region with the median 4.5° from the PALB. The spread of data is normally distributed about the medians although the IQR varies with MLT. The IQR is largest between 21-01 MLT and has a value of 6° MLAT. The IQR decreases through dawn and dusk to noon where it is the smallest with a value of 2.5° MLAT. The (CRB-PALB) poleward offset shows variation over different MLT regions but all median values are offset poleward of the PALB. The farthest deviation is in the pre-midnight region where the median is 9° away from the PALB, this is also accompanied with CRB boundary identifications offset up to 20°. This is likely due to boundary identifications at high latitudes. The pre-noon region is also one of the farthest offset from the PALB by 7°. The closest agreement is in the dawn region from 06-08 MLT where the median is only offset from the PALB by approximately 3°. The IQR here is also small suggesting that the poleward CRB identification in this region correlated to the PALB.

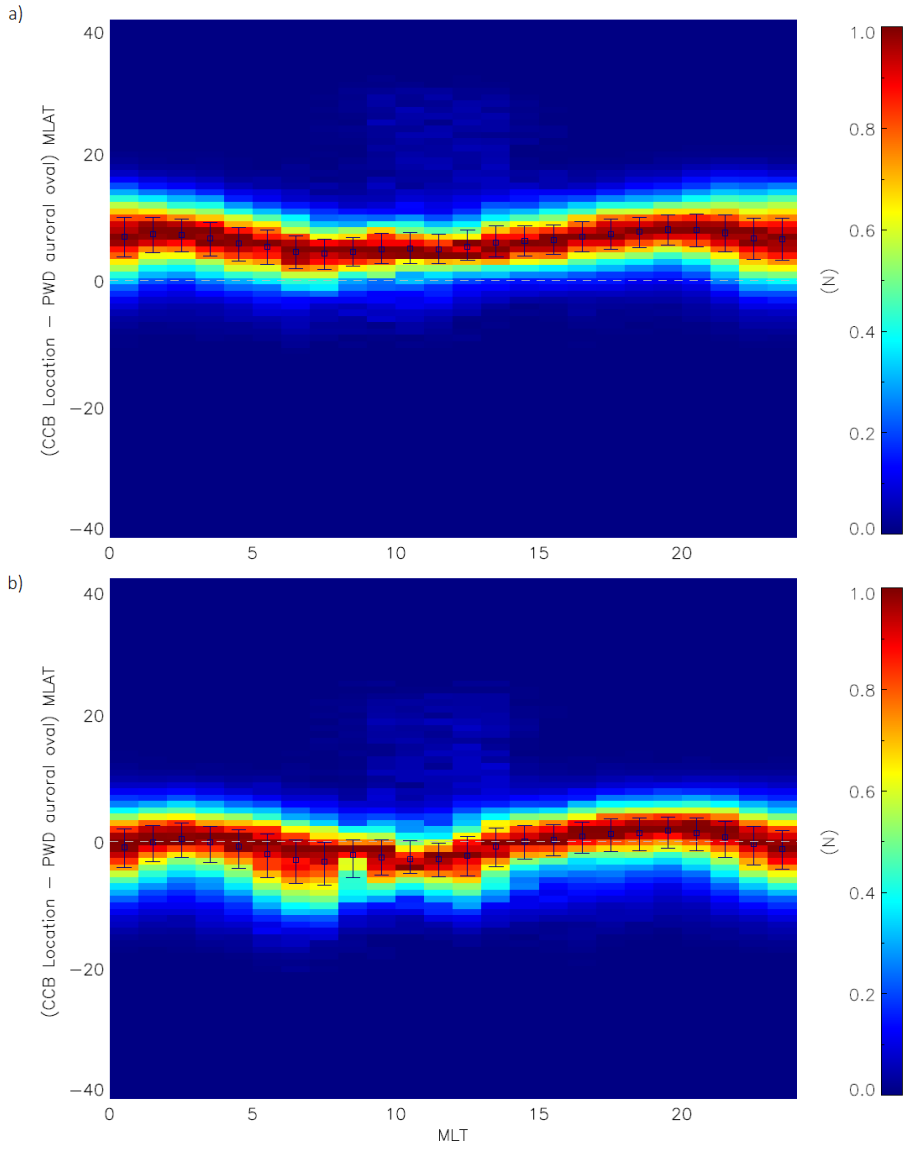

FIGURE 6.10: The distribution of the (CCB-PALB) MLAT boundary identification offsets for double identifications in a given MLT hour.Each hour MLT is scaled in colour relative to the maximum occurrence in that bin. The median and IQR are over plotted in Black and the zero offset line as a grey dashed line for reference. Plot a) shows the distribution of the poleward identification and b) the distribution of the equatorward identification.

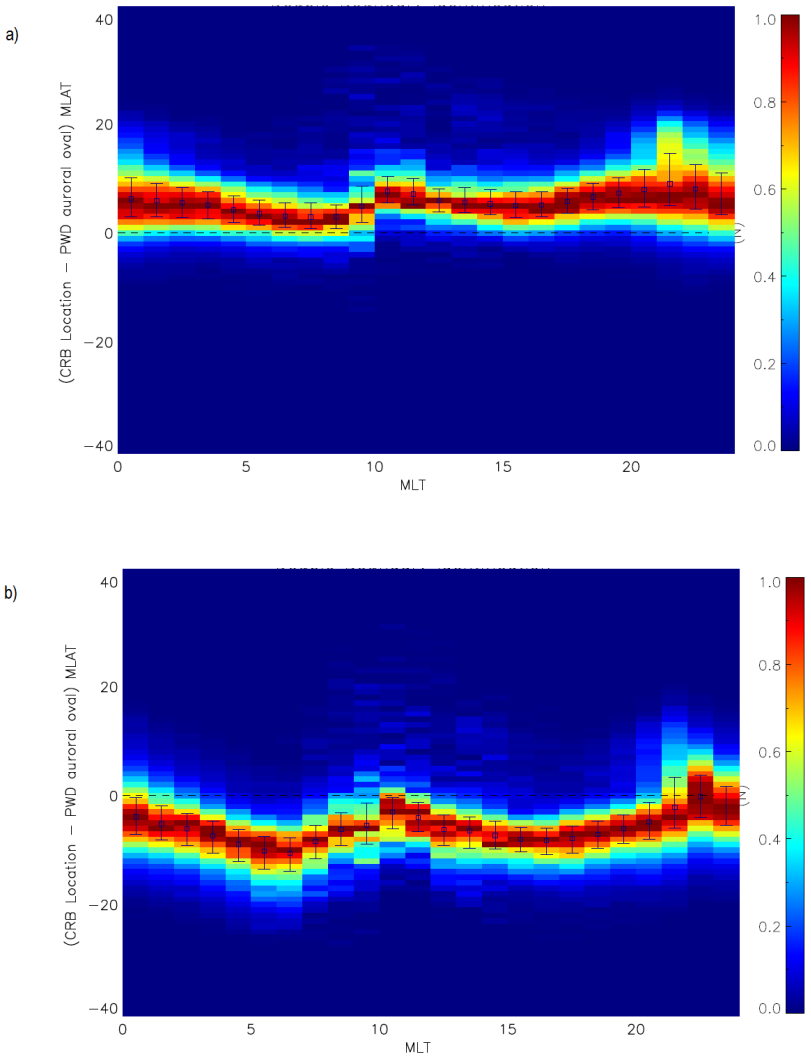

FIGURE 6.11: The distribution of the (CRB-PALB) MLAT boundary identification offsets for double identifications in a given MLT hour.Each hour MLT is scaled in colour relative to the maximum occurrence in that bin. The median and IQR are overplotted in Black and the zero offset line as a grey dashed line for reference. Plot a) shows the distribution of the poleward identification and b) the distribution of the equatorward identification.

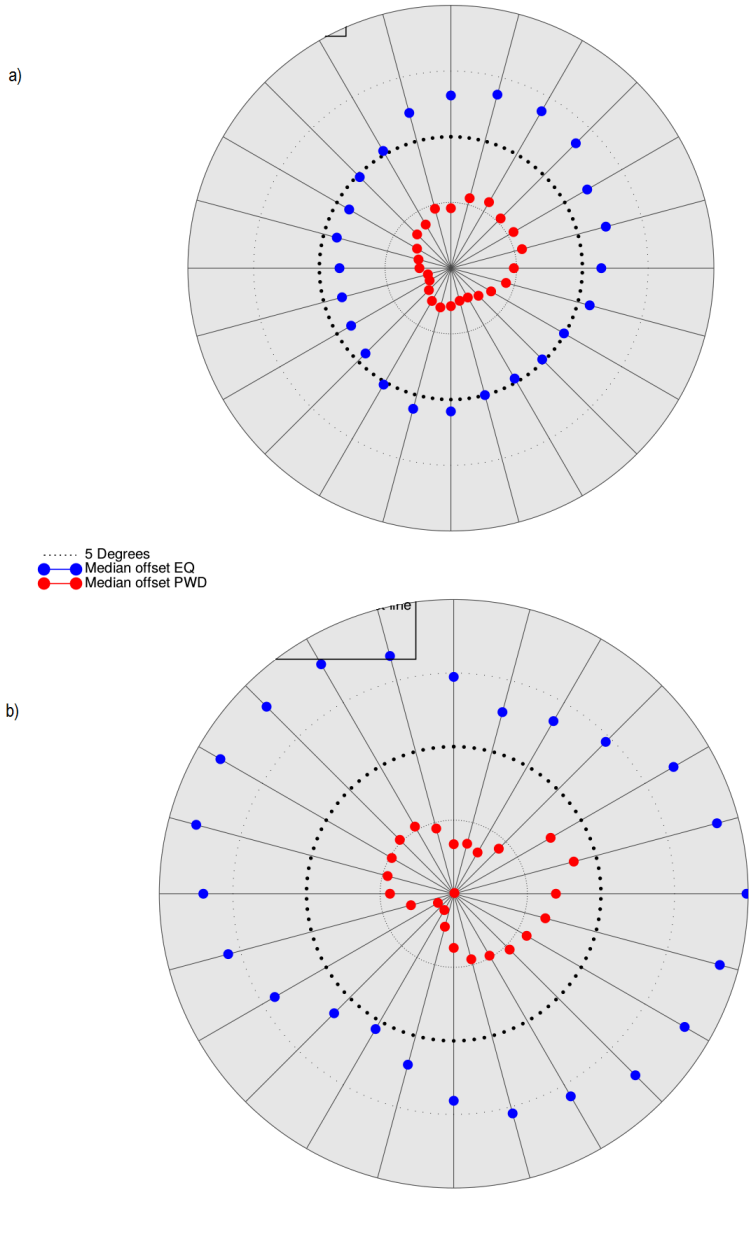

FIGURE 6.12: The plots are presented in a polar grid with the largest black dots showing a zero offset to the PALB. The solid lines directed radially outward separate the MLT hours and the small dots show a 5° offset to the PALB. For each hour of MLT the median value for the poleward (red) and equatorward (blue) a) (CCB-PALB) and b) (CRB-PALB) is shown.

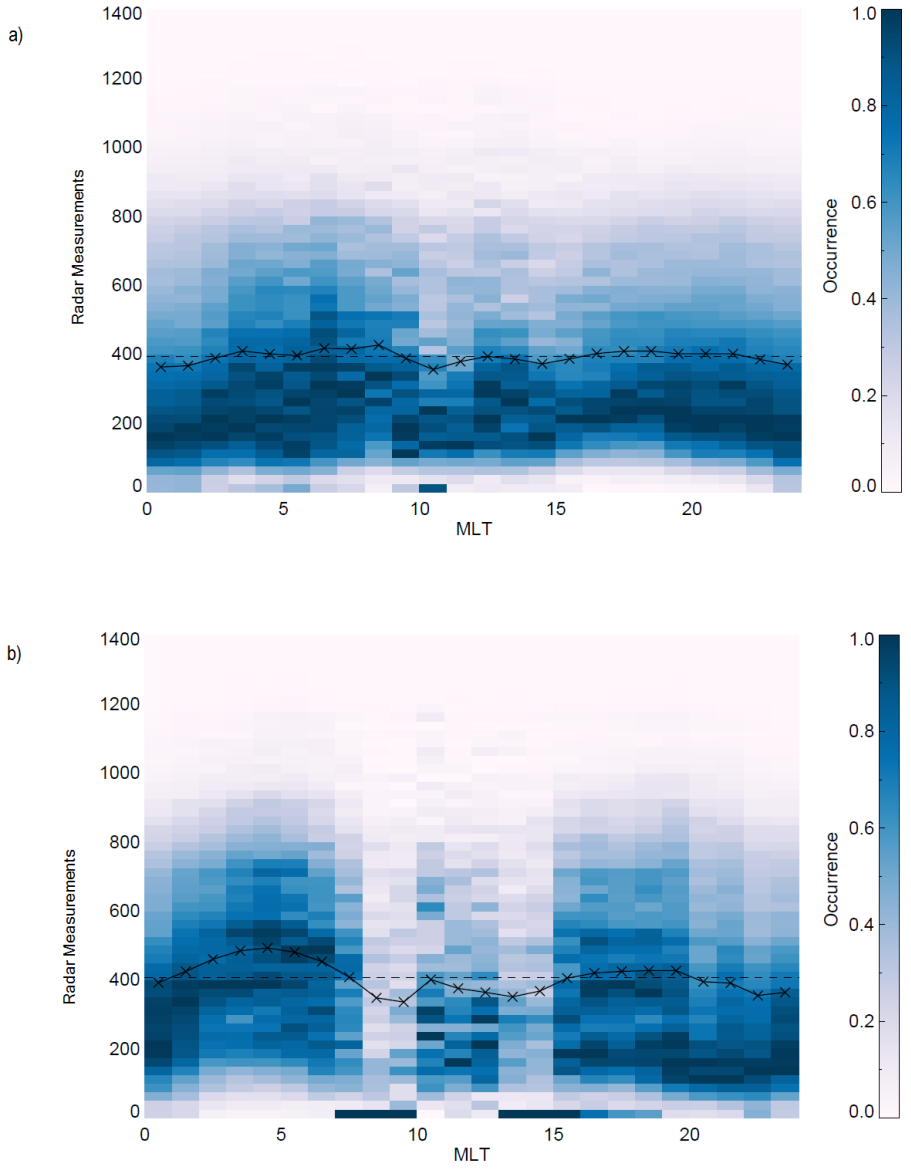

FIGURE 6.13: The distribution of the number of global radar observations for a) the double CCB identifications and b) the double CRB identifications in each hour of MLT. The number of radar observations is grouped in bins of 25 measurements. The black cross and line overplotted gives the median value in each MLT bin. The dashed black line is the average of the median values.

The equatorward identified CCBs reveal a more variable spread across different MLT regions. The IQR is on the order of 5° MLAT except between 05-08 MLT where it increases to 7° MLAT. In the latter region the spread about the mean appears skewed towards negative offsets reaching values of -15°. The equatorward identified offsets agree better with the PALB than the poleward identified offsets. Between 01-04 MLT and 14-18 MLT the offset reduces to within 1° of the PALB. From dawn through to noon (06-13 MLT) the offset shifts equatorward to approximately 2°-3° with the IQR being 2° lower between 10-12 than the other MLT sectors. The (CRB-PALB) equatorward median offsets are farther away from the PALB than for the poleward counterparts in general. The furthest is in the 06-08 MLT region which is shifted 12° equatorward of the PALB, coincidently this was the MLT region that closest agreed with the PALB for poleward offsets. The (CRB-PALB) median at 15-18 MLT is also significantly equatorward and is offset by 12°. The pre-noon and pre-midnight regions show local times that have the closest agreement with the PALB where the median is shifted 3° and 1° equatorward of the PALB respectively. At local times 21-23 the IQR is larger than at other local times and significant variation can be seen across a wide extent of (CRB-PALB) offsets. Apart from the 06-08 MLT region it is not clear if the poleward or equatorward identified boundary most clearly associated with the PALB. Figure 6.12a-b gives an overview of the average locations of the poleward and equatorward offsets from the PALB for each technique. The polar plots are in the same format as figure 6.9, the red dots show the median of the most poleward offset to the PALB for a) the CCB and b) the CRB with the blue dots showing the equatorward median. This clearly shows that for the CCB the equatorward offset aligns closely with the physical boundary for almost all local times. This is less so in the pre-noon sector where the equatorward medians shift equatorward

of the PALB. In general, the result for the CRB technique shown in 6.12b shows neither the poleward or equatorward boundary identifications align closely with the PALB.

As with the single CCB and CRB identifications Figure 6.13 provides an overview of the level of global coverage for each MLT sector for the distributions. The average of the median values across the MLTs is now approximately 400 radar measurements. The spread about the median is not normal but there is a clear shift of the frequency of maps to higher global averages of coverage, especially for the CRB. This is most clearly seen between 15-20 MLT for the CCB case (figure 6.13a) and 02-05 MLT for the CRB case (figure 6.13b) where there are less occurrences of maps with fewer than 150 global radar measurements.

6.3.4 Discussion of double CCB and CRB Identifications

One of the differences between the single and double boundary identifications for both techniques is that on average the double identification was accompanied by an overall higher level of global coverage. Contributions to increased global coverage during the time of this statistical analysis come from a network of nine high-latitude radars. The increase in coverage is latitudinally constrained to the FOV of these radars and covers 65° to 85° MLAT. Since the polar region is not well covered the lack of available data here can distort the map potential fitting and create unphysical kinks at magnetic latitudes greater than 80° MLAT which can affect the dawn and dusk regions. A lack of polar coverage and an increase of high latitude coverage can make the map unbalanced and contribute to unusual equipotential shapes. In the statistical analysis in chapter 5 it was shown that the CRB identifications showed a lot of variability over a wide extent of

latitudes and local times. For example, the unphysical boundary locations at the edge of the convection pattern that were a common occurrence around dawn and noon or the susceptibility to identify boundaries at high latitudes close to the pole particularly around pre-noon and pre-midnight. Given the distributions of the poleward and equatorward identified CRB boundaries in figure 6.11 and their relationship to the PALB it is hard to associate either one with a physical boundary. This is likely due to a combination of the unphysical high and low latitude features contribute to shifting the median CRB-PALB values to higher or lower offsets making it difficult to physically interpret these distributions.

This is not necessarily the case for the CCB. Given that the poleward (CCB-PALB) offsets are significantly higher than for the single CCB identifications it implies that these are related to poor fitting at higher latitudes. For the dusk region (14-20) MLT the equatorward median offset reduces to 1°. The dawn sector between (05-08) MLT is shifted further equatorward of the PALB but during these hours there is significant spread of offsets extending far equatorward of the PALB. This is not as pronounced at other local times. Chapter 5 presented a statistical study of the CCB that showed some lower latitude CCB identifications and attributed these to poor fitting in this region. The electric field is weaker in the dawn cell (*Ruohoniemi and Greenwald*, 1996; *Sotirelis and Newell*, 2000) and as a result, the fitting of the dawn cell is not as stable as the dusk and is more prone to unphysical kinks (resulting in additional lower latitude boundary identifications). At dawn and dusk the poleward boundary is not the one associated with the PALB. The equatorward boundary in both cases agrees much more closely, particularly around dusk. At dawn it is harder to be as confident as unreliable fitting at lower latitudes can impact the result.

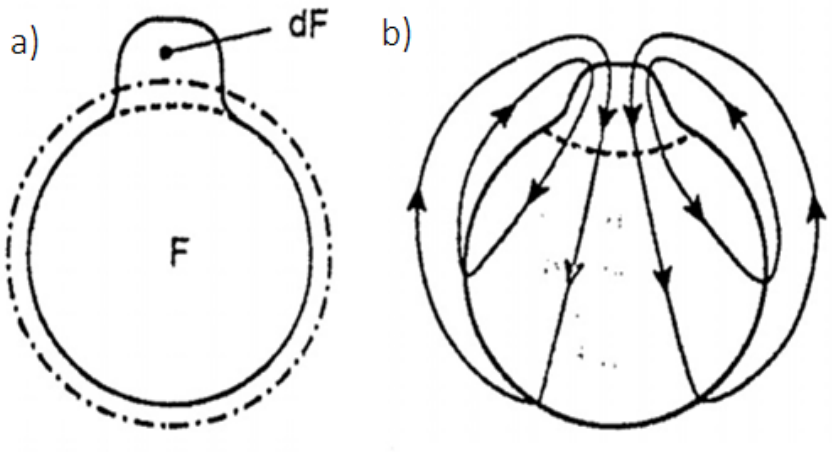

FIGURE 6.14: schematic taken from *Cowley and Lockwood* (1992) showing the a) OCB as the solid black line. The inner dashed line represents the OCB prior to the addition of flux dF and the dotted/dashed line represents the expansion of the OCB after the addition of dF has been redistributed. b) shows the convection flow contours overlaid.

In the noon region (between 10-14 MLT) there appear to be two clear distinct regions with their medians and IQR clearly separated. This is also what was found in Chapter 5, one equatorward and one poleward identification. Interestingly neither boundary seems to associate completely with the PALB but rather occur on either side. The equatorward CCB associates the closest with the PALB offset by $-2.5°$ as opposed to $5°$ for the poleward CCB.

One possible interpretation for the equatorward offset is that just before reconnection the magnetic flux about to be 'opened' lies just equatorward of the OCB. Figure 6.14 shows a schematic taken from Cowley and Lockwood, 1991 showing the a) OCB as the solid black line. The inner dashed line represents the OCB prior to the addition of flux dF and the dotted/dashed line represents the expansion of the OCB after the addition of dF has been redistributed. b) shows the convection flow contours overlaid. Therefore, newly opened flux and the convective flow associated with this could lie equatorward of the OCB. The equatorward CCB identification does agree closest to the PALB compared

to the poleward identification which suggests this boundary is the most likely to be associated with the PALB.

The nightside MLT sectors (21-01) MLT typically have some of the largest IQR and so CCB identifications are spread over a wide range of latitudes. For the poleward CCB identification the median is 7° offset from the PALB, and the equatorward is −1°. It has been shown in chapter 5 that the CCB is still susceptible to high latitude identifications as kinks associated with cross-polar cap flow are picked up. This is likely to explain the higher CCB offsets. The median value for the equatorward CCB is located at lower latitudes than the PALB. It is shifted equatorward 2° compared to the single identification case. Thus there is a significant spread of values occurring equatorward of the PALB. This could be attributed to the presence of secondary flows associated with geophysical phenomena such as substorms.

6.4 Summary

This chapter presented a statistical comparison between automated CCB and CRB SuperDARN identifications and the PALB identified using IMAGE FUV observations and the method described by *Longden et al.* (2010). Single and double CCB identifications are treated separately and split into two sections for analysis purposes. The reasoning was that different MLT regions may be expected to have a single identification, for example found at dawn and dusk. At midnight and noon it may be more likely to observe two, by looking at the most equatorward and poleward offsets for the multiple identifications the systematic offsets could be interpreted. The main findings are summarised below:

For the single CCB and CRB identifications the dawn/dusk MLT regions were furthest

offset from the PALB, by 3°-4° abd 3°-7° respectively. These were the regions theoretically most likely to observe a clear single boundary, the reason for the offset was attributed to the level of radar observations constraining the model. It was found that a significant portion of the global coverage was less than 200 radar measurements. This implies the map potential fitting was reliant on the background model which would likely underestimate the convection pattern and lead to poleward offsets at dawn and dusk by a few degrees.

For the single CRB identifications the offsets were considerably further poleward than the PALB at most local times than for the CCB. As the CRB tends to identify boundaries at high latitudes to the pole it is likely that they are contributing to the shift.

The midnight MLT region for the CCB technique agrees the best with the PALB but a large spread is observed. If the convection pattern is underestimated then identifications associated with the Harang Discontinuity or equatorward flows would shift the median and cause a better agreement.

It was found that for increasing local coverage in certain MLT regions caused better agreement with the PALB. At approximately 60 vectors in the MLT bin, the offset became much more closely aligned to the PALB offset. This suggests that a high number of radar observations is needed locally to constrain the fit. A global threshold of 200 with no condition on the MLT/MLAT spread may not be enough to quantify what constitutes a reliable map.

The double boundary identifications corresponded to higher level of global coverage than for the single. For the CRB neither the poleward or equatorward boundaries aligned closely with the PALB. For the CCB the poleward offsets were mostly attributed to poor fitting of the map potential model at high latitudes and the equatorward offsets

agree much more closely to the PALB at most local times. At noon two separate regions are identified either side of the PALB.

Around midnight the most equatorward CCB identification more closely aligns with the PALB and its median value being offset by 1° from the auroral boundary. This could show evidence of the presence of secondary flows associated with substorms occurring equatorward of the PALB shifting the median value downward. It is not easy to tell however, as this region is also associated with a large IQR.

Chapter 7

Summary and future directions

This thesis has focussed on the applicability of using SuperDARN convection maps as a tool to identify meaningful geophysical boundaries. SuperDARN provides a wealth of high latitude ionospheric convection measurements spanning two decades making it an invaluable archive of data. Proxies for the polar cap boundary can provide useful information on the time-dependent dynamics of the coupled solar wind-magnetosphere-ionosphere system. These are widely utilised by both spacecraft and ground-based instruments with a large range of techniques. The most accurate global proxy for the OCB is usually made with an imaging spacecraft and this is limited to the years of spacecraft operation and so continuous observations are not available. This makes further investigating the relationship of SuperDARN observations to the OCB a worthwhile and meaningful endeavour.

Currently the convection reversal boundary is a common technique used to identify a proxy OCB and has yielded comparable results to low-altitude spacecraft and auroral images in selected studies. However we find that unchecked, this technique can identify unphysical boundary locations at a variety of local times, especially close to noon and

midnight. Chapter 4 has presented a new boundary technique that follows the location of maximum curvature across successive convection streamlines (the convection curvature boundary, or CCB). The CCB appears to be more robust, identifying a more physical boundary at most local times in a statistical comparison between it, and the CRB, as was presented in Chapter 5. Both of these techniques were also compared to observations of the PALB made by the FUV instrument on board IMAGE, a well-established proxy for the OCB. The CCB was shown to be a good proxy for the PALB showing agreements on the order or 1° providing there are enough radar measurements.

Both the effect of radar coverage and magnetotail phenomena (substorms) have an effect on the ionospheric convection and the subsequent reliability of the derived convection map. These two things are inter-related and the effects of each at times can be difficult to distinguish. Clearly there is scope for further work in this area to better understand their effects. The sections below highlight some preliminary work that has been undertaken that could form the basis of future studies.

7.1 Comparison of the nightside throat location to IMAGE observations

A number of studies have described the average statistical patterns of the ionospheric convection according to the IMF orientation using ground observations from SuperDARN as presented above and also spacecraft observation of the polar cap electric fields e.g. (*Ruohoniemi and Greenwald*, 1996, 2005; *Thomas and Shepherd*, 2018). Furthering this, some recent studies have been conducted using the SuperDARN network to elucidate the average convection flow pattern during substorm times (*Grocott et al., 2009*) and

also to understand the combined effect of the IMF dawn-dusk component and substorm time dynamics on the flow (*Grocott et al.*, 2010, 2017). Most recently *Grocott et al.* (2017) created average convection patterns that were grouped by substorm onset latitude, magnetic local time and the IMF B_y condition. They found clear evidence in their statistical averages that the nightside convection throat was largely aligned with the substorm onset locations as opposed to the prevailing IMF conditions. If this is the case, then the nightside convection throat at substorm onset in an individual map should also see the same relationship. To investigate this the *Frey* substorm list is used to identify substorm onset locations and a corresponding dataset of SuperDARN maps is generated. The initial list presented by Frey et al., (2004) spans May 2000 to December 2002 and identifies 2437 individual substorms. The list has since been updated to include events up to December 2005 and now totals a list of 4193 substorms.

In this instance a rudimentary technique was used to identify the night throat region in an automated way, similar to the CCB technique discussed in chapter 4. The average potential value was found along each line of latitude starting at the Heppner-Maynard boundary between 18-06 MLT (nightside). When a line of latitude was reached where the average potential value was at least |3| kV the minimum potential along that latitude was found. Figure 7.1 shows an example SuperDARN plot from 20 January 2000, 19:08 UT with a red cross shown where the automated routine chose the throat location. In general this appeared to work quite well when a clear two-cell configuration was present but, at times could be placed in an un-physical location as a result of bad fitting.

As an initial test the SuperDARN night throat locations are plotted against the substorm onset location. The result is shown in figure 7.2 with the red line overlayed showing the

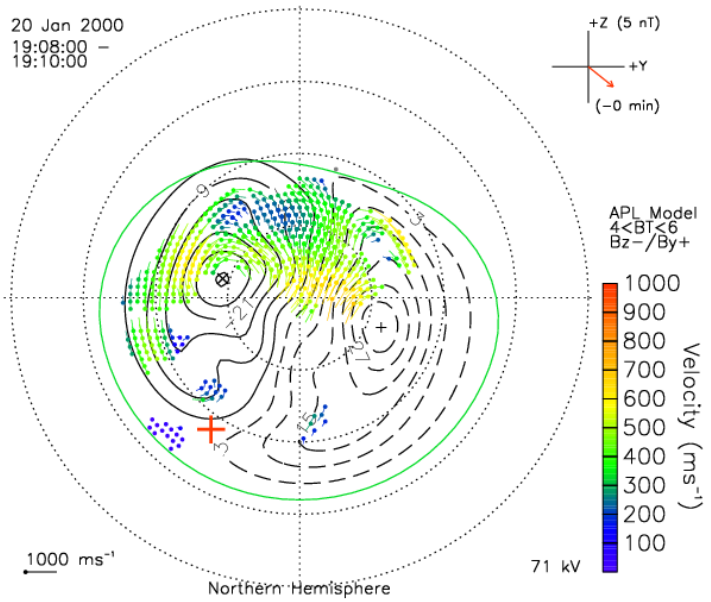

FIGURE 7.1: A test SuperDARN map showing the high latitude convection generated on 20 January 2000, 19:08 UT. 12 MLT is orientated to the top of the figure, the convection equipotentials are shown as the solid and dashed curved lines. The red cross is placed at the night throat location as deduced by the automated routine described in the text.

line of best fit. It is immediately obvious that the distribution of scatter is broad and there does not appear to be a relationship from this data. This is also confirmed with a low correlation coefficient R=0.11. Given that previous statistical studies had seen the substorm throat location to be ordered by the substorm onset location this was a little unexpected. The variability could come because there is not actually a 1:1 relationship between the nightside throat location and the substorm onset location.

The relationship is likely to be more complex, although the substorm onset location heavily influences the nightside convection morphology e.g. (*Grocott et al.*, 2010) other factors will likely also play a part. For example the time-history of the magnetosphere could influence the nature of the convection at onset. A more appropriate analysis for the future could be to perform a superposed epoch analysis of the throat location and

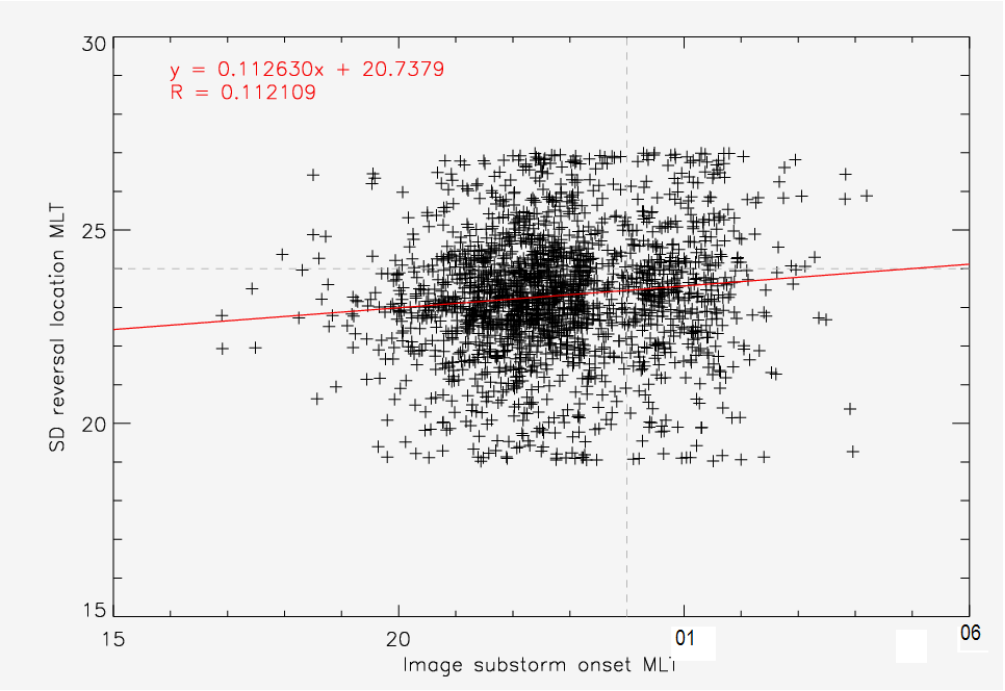

FIGURE 7.2: A comparison of the IMAGE onset location (*Frey*) with the SuperDARN nightside throat location as determined by an automated routined described in the text

its motion in MLT during the substorm growth phase. This could identify if relative changes to the ionospheric convection in the substorm region occur.

7.2 Nightside throat location and radar coverage

To inspect whether data coverage could be affecting the throat location analysis of the relationship of the nightside throat location and the spatial distribution of the radar coverage was investigated. The global convection maps provided by SuperDARN are a widely utilised data product but often only rudimentary quality flags are implemented on the level of global scatter. Chapter 6 has shown that the level of local coverage is important to the reliability of the map. There is still a need to quantify how the distribution of coverage affects the subsequent pattern. For all SuperDARN maps in January 2000

the nightside throat location was determined from the automated algorithm described in the previous section.

The distribution of radar observations for the entire month was recorded in a grid centred on the magnetic pole in 10° MLAT and 2 hour MLT bins. Then, a second set of radar observation distributions was generated grouping together maps with the same nightside throat location MLT. Finally, difference maps were produced as the monthly averaged data grid was taken away from the binned nightside throat MLT data grids.

This result for the 20-21, 23-24 and 02-03 MLT bins are shown in Figure 7.3 as the top, middle and bottom plots respectively. Areas of deeper red indicate areas with increased coverage as compared to the average and deeper blue, less coverage as compared to the average. What is interesting is that for the 'early' nightside throat locations. i.e. those at earlier local times than the average substorm average location at 23 MLT (Frey et al., 2004) there is an increase in data coverage at local times just earlier than the throat location. This is also the case for the 'late' throat locations where a clear increase over the average is seen extending into early local times. The MLT bin (23-24 MLT) at the average substorm location shows less data coverage globally than the overall average. This could be explained by the fact that if the convection pattern has low data coverage then the background model is contributing significantly to the pattern and the throat location would fall to average values. This suggests that the data coverage is playing a significant role in the morphology of the derived convection pattern at these locations. Data coverage issues could therefore be playing a significant role in the apparent lack of a relationship between the nightside throat and substorm onset MLT.

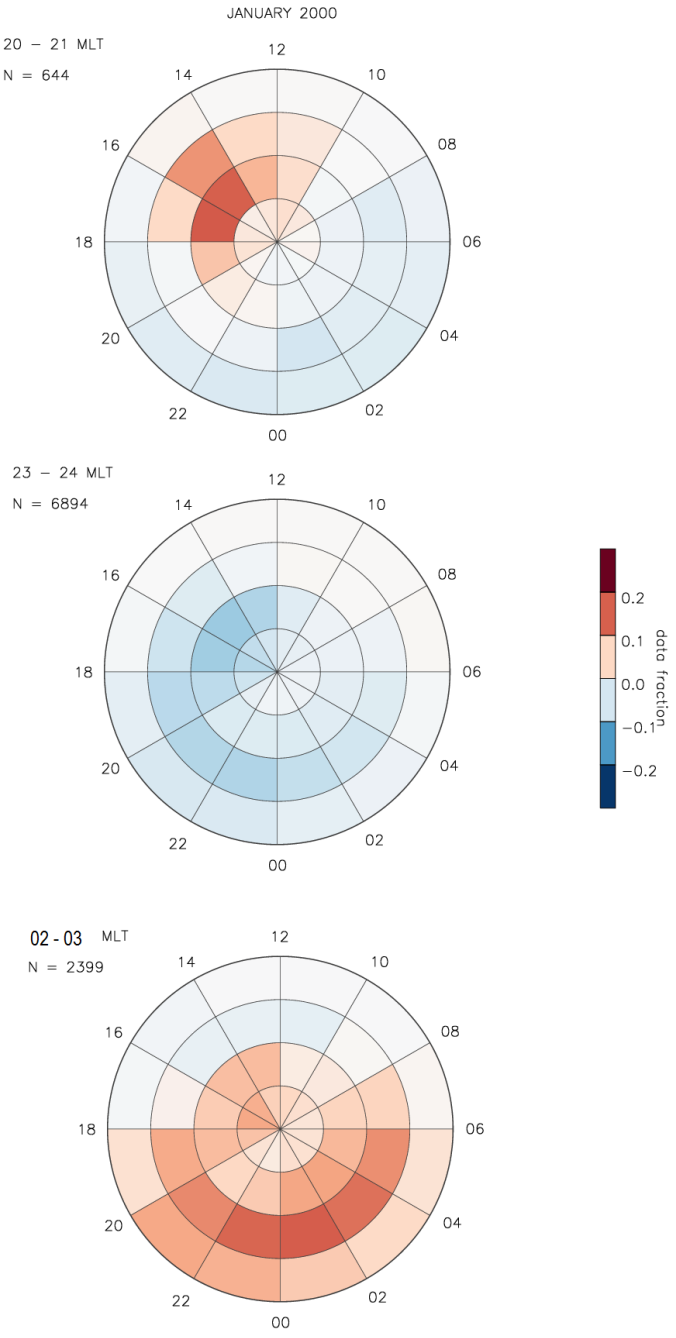

FIGURE 7.3: Three grids in polar AAGCM coordinates with the magnetic pole at the centre, noon MLT orientated to the top of the figure and dusk to the left. The lowest circle is the 50° MLAT boundary and subsequent circles decrease in 10° MLAT. The level of data coverage is grouped according to the nightside throat location in 2 hour MLT/10° MLAT bins. The diverging colour scale highlights regions on each grid that have higher (red) and lower (blue) than average radar coverage for 20-21 MLT (top), 23-34 MLT (middle) and 02-03 MLT (bottom)

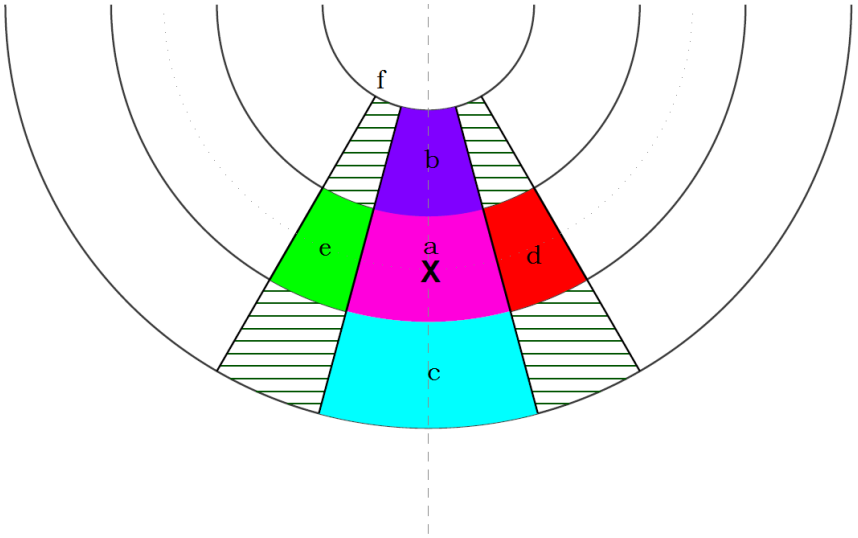

FIGURE 7.4: A sketch to show the substorm orientated boxes. The substorm onset location is shown by the cross. Each arc shows 5° MLAT increments away from the substorm onset location and the solid straight lines represent 1 and 2 hours of MLT away. The colour corresponds to the results in Figure 7.5.

modifies the global convection pattern was to look at how the amount of scatter varied relative to substorm onset, as opposed in the fixed AACGM coodinate system.

To identify individual convection maps during substorms for analysis an initial list of substorms must be compiled. In this study the same substorm list used by *Wild and Grocott* (2008) and *Grocott et al.* (2010) initially derived by *Frey* is taken.

Figure 7.4 shows a sketch of the substorm coordinate system splitting the areas directly surrounding the substorm onset location into a series of 6 boxes. There are 6 boxes in this coordinate system ranging from between +/- 5 and 10 degrees latitude and +/- 2 hours longitude from the substorm onset location as shown by the cross in Figure 7.4. Figure 7.5 presents a superposed epoch analysis over a four hour period beginning one hour before the substorm onset time. The total number of vectors in each box, for each map, across the four hour time interval are presented. The vertical dashed grey line

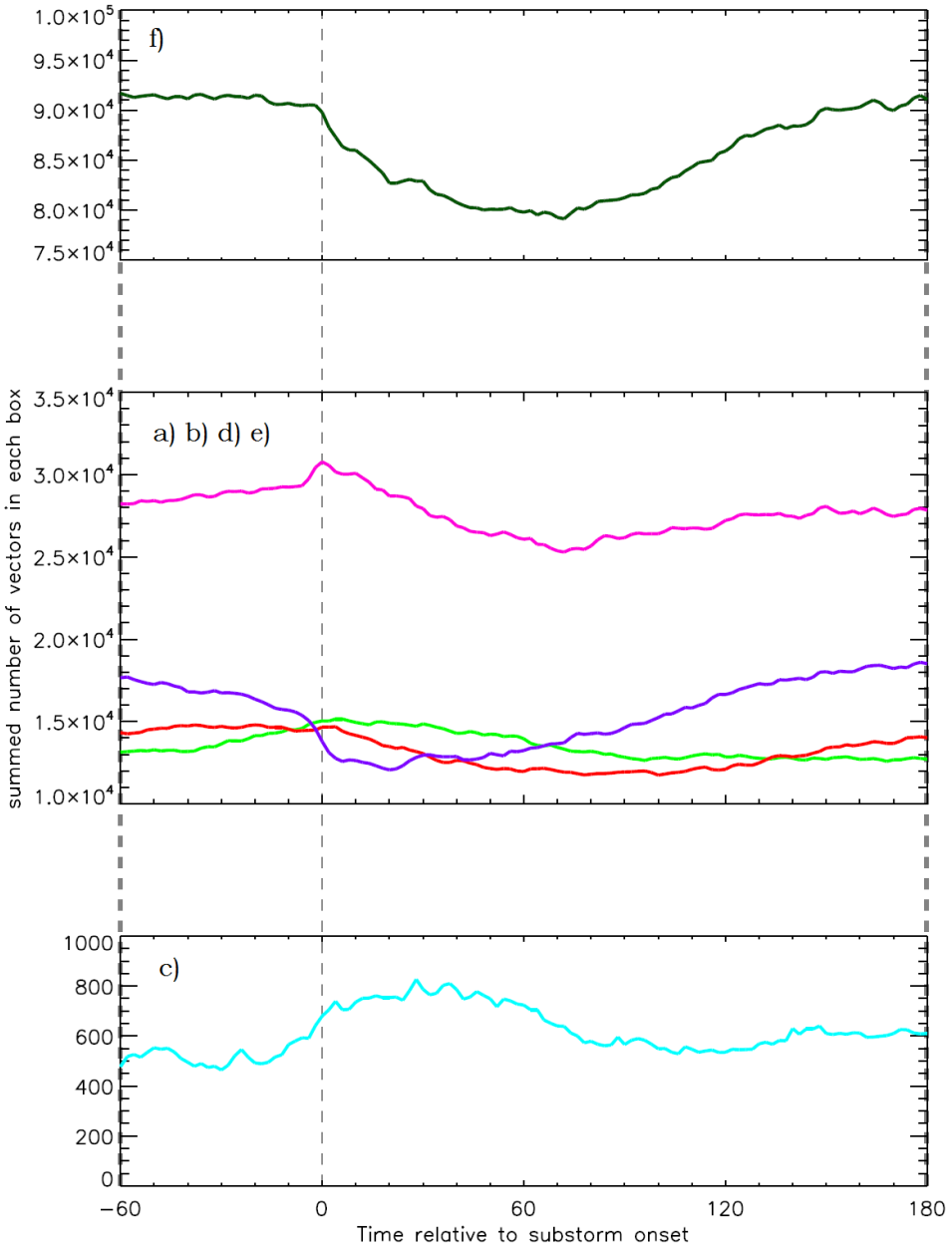

FIGURE 7.5: A superposed epoch analysis of the cumulative total number of vectors in each box defined in Figure 7.4 for a four hour period centered on the substorm onset.

indicates the time of onset.

It is clear that almost all boxes (except c, e and d) show a drop off in radar observations after the substorm onset phase consistent with results from *Provan et al.* (2004) and *Wild and Grocott* (2008). This is seen the most obviously for box (f), however this is to be expected since this box covers the larger area. For the smaller boxes some do maximise just before onset and then decrease, but there are some exceptions. Box (b), for example steadily decreases in the hour before onset and continues for approximately 30 minutes after. Interestingly, box (c) does not show a decrease after onset and instead increases, before exhibiting a slight decrease an hour after the onset time. This does imply that different regions respond differently to substorm onset and so there is a case for investigation to be done into the effect of substorm backscatter location on the generation of global convection maps.

In summary, whilst many large-scale features of the ionospheric convection pattern can be readily captured in the basic SuperDARN 'convection map' data product, as illustrated, for example by the work presented in Chapter 5 and 6 of this thesis, there are still some intricacies in the relationship between substorm flows and data coverage in particular that need to be investigated further. This chapter has shown some preliminary analyses that shed some light on this relationship, and which could be developed further in future research.

Appendix A

Coordinate Systems

This appendix provides a description of the coordinate systems used in this thesis.

A.1 Geocentric Solar Magnetic Coordinates

In the geocentric solar magnetic (GSM) coordinate system the positive X-axis is directed towards the sun from the Earth. The Y-axis is defined to be perpendicular to the Earth's magnetic dipole so that the X-Z plane contains the dipole axis and is positive towards dusk. The positive Z-axis is chosen to be the same sense as northern magnetic pole. The GSM coordinate system is typically used when studying interplanetary magnetic field effects on the magnetosphere or ionosphere.

A.2 Magnetic Local Time

Magnetic Local Time (MLT) is a coordinate system that is used to organise data and models with respect to the position of the sun as it not always appropriate to use coordinates fixed with respect to the Earth, for example magnetic longitude. *Baker and S.* (1989) define the magnetic local time as:

$$MLT = UT + (\phi + \Phi_N)/15 \tag{A.1}$$

where ϕ is the magnetic longitude, Φ_N the geographic longitude and UT the universal time specified in hours.

A.3 Altitude Adjusted Corrected Geomagnetic Coordinate System

The Altitude Adjusted Corrected Geomagnetic Coordinate System (AACGM) is very useful in space physics as it is defined such that all points along a magnetic field line have the same latitude and longitude. As magnetospheric particles travel along magnetic field lines and can precipitate into the ionosphere, having a coordinate system that traces their trajectories along the field line can help to understand how different regions of the ionosphere couple together.

To compute the AACGM coordinates at a point above the Earth's surface, defined by its geographic latitude, longitude and altitude, is determined by first tracing the magnetic field line at this point to the magnetic dipole equator. From here the latitude and longitude of the dipole field line that connects this point on the magnetic equator to the surface of the Earth defines the AACGM coordinates. The magnetic field lines are typically calculated using an International Geomagnetic Reference Field (IGRF) and the dipole latitude computed from the L-shell of the intersection point on the magnetic equator.

Figure A.1 shows three examples of determining AACGM coordinates at geographic locations covering latitudes 30°, 40° and 50°. Red lines show the IGRF magnetic field lines and join the geographic starting locations to the magnetic equator, shown as a

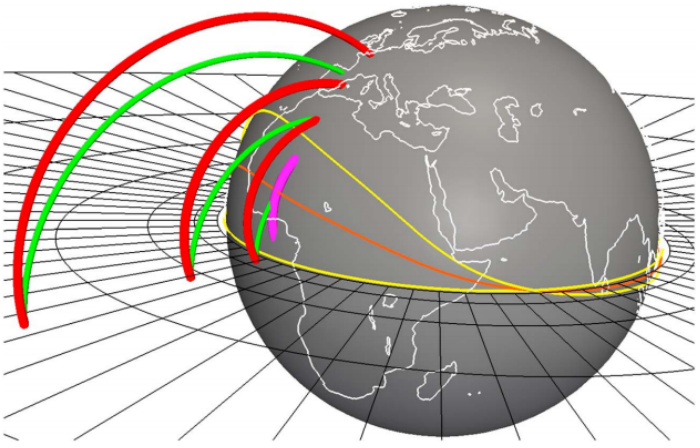

FIGURE A.1: Taken from Figure 1 of *Shepherd* (2014). Three examples of determining AACGM coordinates at geographic locations covering latitudes 30°, 40° and 50°. Red lines show IGRF magnetic field lines and join the geographic starting locations to the magnetic equator. AACGM coordinates are given by the coordinates dipole field lines, shown in green.

radial grid. AACGM coordinates are given by the latitude and longitude at the location where the dipole field line joins the Earth's surface, shown by the green lines in this figure. If the IGRF field line does not intersect the magnetic equator, as shown in figure A.1 as the magenta line, then no AACGM coordinates can be calculated.

References

(2004), *Location of Magnetopause Reconnection*.

Akasofu, S. I. (1964), The development of the auroral substorm, *Planetary and Space Science*, *12*(4), 273–282, doi:10.1016/0032-0633(64)90151-5.

Alfvén, H. (1942), Existence of electromagnetic-hydrodynamic waves, *Nature*, *150*, 405–406.

Baker, D., T. Pulkkinen, V. Angelopoulos, W. Baumjohann, and R. McPherron (1996), Neutral line model of substorms: Past results and present view, *J. Geophys. Res*, *101*, 12,975–13,010, doi:10.1029/95JA03753.

Baker, J. B., C. R. Clauer, a. J. Ridley, V. O. Papitashvili, M. J. Brittnacher, and P. T. Newell (2000), The nightside poleward boundary of the auroral oval as seen by DMSP and the Ultraviolet Imager, *Journal of Geophysical Research*, *105*(1999), 21,267, doi:10.1029/1999JA000363.

Baker, K. B., and W. S. (1989), A new magnetic coordinate system for conjugate studies at high latitudes, *Journal of Geophysical Research*, *49*, doi:10.1029/JA094iA07p09139.

Baker, K. B., J. R. Dudeney, R. a. Greenwald, M. Pinnock, P. T. Newell, a. S. Rodger, N. Mattin, and C.-I. Meng (1995), HF radar signatures of the cusp and low-latitude boundary layer, *Journal of Geophysical Research*, *100*(A5), 7671–7695, doi:10.1029/94JA01481.

Baumjohann, W., and R. A. Treumann (1996), *Basic Space Plasma Physics*, doi:https://doi.org/10.1142/p015.

Blanchard, G. T., L. R. Lyons, J. C. Samson, and F. J. Rich (1995), Locating the polar cap boundary from observations of 6300 Å auroral emission, *Journal of Geophysical Research*, *100*(A5), 7855, doi:10.1029/94JA02631.

Boakes, P. D., S. E. Milan, G. A. Abel, M. P. Freeman, G. Chisham, B. Hubert, and T. Sotirelis (2008), On the use of IMAGE FUV for estimating the latitude of the open/closed magnetic field line boundary in the ionosphere, *Annales Geophysicae*, *26*(9), 2759–2769, doi:10.5194/angeo-26-2759-2008.

Boakes, P. D., S. E. Milan, G. A. Abel, M. P. Freeman, G. Chisham, and B. Hubert (2009), A statistical study of the open magnetic flux content of the magnetosphere at the time of substorm onset, *Geophysical Research Letters*, *36*(4), 3–7, doi:10.1029/2008GL037059.

Bristow, W. A., and J. Spaleta (2013), An investigation of the characteristics of the convection reversal boundary under southward interplanetary magnetic field, *Journal of Geophysical Research: Space Physics*, *118*(10), 6338–6351, doi:10.1002/jgra.50526.

Brittnacher, M., M. Fillingim, G. Parks, G. Germany, and J. Spann (1999), Polar cap area and boundary motion during substorms, *J. Geophys. Res.*, *104*(A6), 12,251–12,262, doi:10.1029/1998ja900097.

Burch, J. L. (2000), IMAGE mission overview, *Space Sci. Rev.*, *91*(c), 1–14, doi:http://dx.doi.org/10.1023/A:1005245323115.

Carbary, J. F., T. Sotirelis, P. T. Newell, and C. I. Meng (2003), Auroral boundary correlations between UVI and DMSP, *Journal of Geophysical Research: Space Physics*, *108*(A1), doi:10.1029/2002JA009378.

Chen, Y., R. A. Heelis, and J. A. Cumnock (2015), Plasma and convection reversal boundary motions in the highlatitude ionosphere, *Journal of Geophysical Research : Space Physics*, *121*, 5752–5763, doi:10.1002/2015JA021024.Received.

Chen, Y. J., and R. A. Heelis (2018), Motions of the Convection Reversal Boundary and Local Plasma in the High-Latitude Ionosphere, *Journal of Geophysical Research: Space Physics*, *123*(4), 2953–2963, doi:10.1002/2017JA024934.

Chisham, G. (2017), A new methodology for the development of high-latitude ionospheric climatologies and empirical models, *Journal of Geophysical Research: Space Physics*, *122*(1), 932–947, doi:10.1002/2016JA023235.

Chisham, G., and M. P. Freeman (2003), A technique for accurately determining the cusp-region polar cap boundary using SuperDARN HF radar measurements, *Annales Geophysicae*, *21*(4), 983–996, doi:10.5194/angeo-21-983-2003.

Chisham, G., M. Pinnock, and A. S. Rodger (2001), The response of the HF radar spectral width boundary to a switch in the IMF By direction: Ionospheric consequences of transient dayside reconnection?, *Journal of Geophysical Research: Space Physics*, *106*(A1), 191–202, doi:10.1029/2000JA900094.

Chisham, G., M. Pinnock, I. J. Coleman, M. R. Hairston, and A. D. M. Walker (2002), An unusual geometry of the ionospheric signature of the cusp : implications for magnetopause merging sites, *Annales Geophysicae*, pp. 29–40, doi:10.5194/angeo-20-29-2002.

Coroniti, F. V., and C. F. Kennel (1973), Can the Ionosphere Regulate Magnetospheric Convection?, *78*(16), 2837–2851, doi:10.1029/JA078i016p02837.

Cowley, S. (1993), The magnetosphere and its interaction with the solar wind and with the ionosphere. in: Dewitt r.n., duston d., hyder a.k. (eds), *The Behaviour of Systems in the Space Environment. NATO ASI Series (Series E: Applied Sciences)*, *245*, doi: 10.1007/978-94-011-2048-7_7.

Cowley, S., and M. Lockwood (1992), Excitation and decay of solar wind-driven flows in the magnetosphere-ionosphere system, *Annales Geophysicae*, *10*, 103–115.

Cowley, S. W. H., J. P. Morelli, and M. Lockwood (1991), Dependence of convection flows and particle precipitation in the high latitude dayside ionosphere on the x and y components of the interplanetary magnetic field, *J. Geophys. Res.*, *96*(A4), 5557–5564.

Craven, J. D., and L. A. Frank (1987), Latitudinal Motions of the Aurora During Substorms, *Journal of Geophysical Research: Space Physics*, *92*(A5), 4565–4573, doi: 10.1029/JA092iA05p04565.

de Larquier, S., P. Ponomarenko, A. J. Ribeiro, J. M. Ruohoniemi, J. B. H. Baker, K. T. Sterne, and M. Lester (2013), On the spatial distribution of decameter-scale subauroral ionospheric irregularities observed by superdarn radars, *Journal of geophysical research: Space Physics*, *118*, 5244–5254, doi:10.1002/jgra.50475.

Dungey, J. W. (1961), Interplanetary magnetic field and the auroral zones, *Physical Review Letters*, *6*(2), 47–48, doi:10.1103/PhysRevLett.6.47.

Elphic, R. C., M. Lockwood, S. W. Cowley, and P. E. Sandholt (1990), Flux transfer events at the magnetopause and in the ionosphere, *Geophysical Research Letters*, *17*(12), 2241–2244, doi:10.1029/GL017i012p02241.

Fejer, B. G., and M. C. Kelley (1980), Ionospheric Irregularities, *18*(2), 401–454, doi: 10.1016/j.apgeog.2011.10.013.

Feldstein, Y. I., and Y. I. Galperin (1985), The auroral luminosity structure in the highlatitude upper atmosphere: Its dynamics and relationship to the largescale structure of the Earth's magnetosphere, *Reviews of Geophysics*, *23*(3), 217–275, doi: 10.1029/RG023i003p00217.

Foster, J. C., and H. B. Vo (2002), Average characteristics and activity dependence of the subauroral polarization stream, *Journal of Geophysical Research: Space Physics*, *107*(A12), 1–10, doi:10.1029/2002JA009409.

Freeman, M. P., and D. J. Southwood (1988), The effect of magnetospheric erosion on mid- and high-latitude ionospheric flows, *Planetary and Space Science*, *36*(5), 509–522, doi:10.1016/0032-0633(88)90110-9.

Frey, H. (), Substorm onset observations by IMAGE-FUV., *J. Geophys. Res*, *109*.

Fuselier, S. A., A. G. Ghielmetti, T. E. Moore, M. R. Collier, J. M. Quinn, R. Wilson, P. Wurz, S. B. Mende, H. U. Frey, C. Jamar, J. Gerard, and L. Burch (1997), Ion outflow observed by IMAGE : regions and heating mechanisms Implications for source, *Image (Rochester, N.Y.)*, *28*(6), 1163–1166.

Goldston, R. J., and P. H. Rutherford (1995), *Introduction to Plasma Physics*.

Gosling, J. T., M. F. Thomsen, S. J. Bame, C. T. Russell, and R. C. Elphic (1990), Plasma flow reversals at the dayside magnetopause and the origin of asymmetric polar cap convection, *Journal of Geophysical Research*, *95*(A6), 8073, doi: 10.1029/ja095ia06p08073.

Greenwald, R. A., K. B. Baker, R. A. Hutchins, and C. Hanuise (1985), An HF phased array radar for studying small scale structure in the high latitude ionosphere, *Radio Science*, *20*(1), 63–79, doi:10.1029/RS020i001p00063.

Greenwald, R. a., K. B. Baker, J. R. Dudeney, M. Pinnock, T. B. Jones, E. C. Thomas, J.-P. Villain, J.-C. Cerisier, C. Senior, C. Hanuise, R. D. Hunsucker, G. Sofko, J. Koehler, E. Nielsen, R. Pellinen, a. D. M. Walker, N. Sato, and H. Yamagishi (1995), DARN/-SuperDARN, *Space Science Reviews*, *71*(1-4), 761–796, doi:10.1007/BF00751350.

Grocott, A., J. A. Wild, S. E. Milan, and T. K. Yeoman (2009), Superposed epoch analysis of the ionospheric convection evolution during substorms: Onset latitude dependence, *Annales Geophysicae*, *27*(2), 591–600, doi:10.5194/angeo-27-591-2009.

Grocott, A., S. Milan, T. Yeoman, N. Sato, A. Yukimatu, and J. Wild (2010), Superposed epoch analysis of the ionospheric convection evolution during substorms: IMF BY dependence., *J. Geophys. Res.*, *115*, doi:10.1029/2010JA015728.

Grocott, A., S. E. Milan, S. M. Imber, M. Lester, and T. K. Yeoman (2012), A quantitative deconstruction of the morphology of high-latitude ionospheric convection, *Journal of Geophysical Research: Space Physics*, *117*(5), 1–16, doi:10.1029/2012JA017580.

Grocott, A., H. J. Laurens, and J. A. Wild (2017), Nightside Ionospheric Convection Asymmetries During the Early Substorm Expansion Phase: Relationship to Onset Local Time, *Geophysical Research Letters*, *44*(23), 11,696–11,705, doi:10.1002/2017GL075763.

Haaland, S. E., A. Runov, and C. Forsyth (2017), American Geophysical Union, *Dawn-dusk asymmetries in planetary plasma environments*, *Hoboken*.

Harang, L. (1946), The auroral Luminosity-Curve, *Terrestrial Magnetism and Atmospheric Electricity*, *51*, doi:10.1029/TE051i003p00381.

Heppner, J. P., and N. C. Maynard (1987), Empirical high-latitude electric field models, *Journal of*, *92*, 4467–4489, doi:10.1029/JA092iA05p04467.

Hesse, M., M. Kuznetsova, and J. Birn (2004), The role of electron heat flux in guide-field magnetic reconnection, *Physics of Plasmas*, *11*(12), 5387–5397, doi:10.1063/1.1795991.

Holzworth, R. H., and C. I. Meng (1975), Mathematical Representation of the auroral oval, *Geophysical Research Letters*, *2*(9), 0–3.

Hones, E. W., and L. Alamos (1979), Transient phenomena in the magnetotail and their relation to substorms , *23*(June 1978), 393–410.

Hubert, B., A. T. Aikio, O. Amm, T. Pitkänen, K. Kauristie, S. E. Milan, S. W. Cowley, and J. C. Gérard (2010), Comparison of the open-closed field line boundary location inferred using IMAGE-FUV SI12 images and EISCAT radar observations, *Annales Geophysicae*, *28*(4), 883–892, doi:10.5194/angeo-28-883-2010.

Imber, S. M., S. E. Milan, and M. Lester (2013), The Heppner-Maynard Boundary measured by SuperDARN as a proxy for the latitude of the auroral oval, *Journal of Geophysical Research: Space Physics*, *118*(2), 685–697, doi:10.1029/2012JA018222.

Jørgensen, T. S., E. Friis-Christensen, and J. Wilhjelm (1972), Interplanetary magnetic-field direction and high-latitude ionospheric currents, *Journal of Geophysical Research*, *77*(10), 1976–1977, doi:10.1029/ja077i010p01976.

Kauristie, K., J. Weygand, T. I. Pulkkinen, J. S. Murphree, and P. T. Newell (1999), Size of the auroral oval: UV ovals and precipitation boundaries compared, *J. Geophys. Res.*, *104*(A2), 2321–2331, doi:10.1029/1998ja900046.

Kelley, M. C., J. F. Vickrey, C. W. Carlson, and R. Torbert (1982), On the origin and spatial extent of high-latitude F region irregularities, *Journal of Geophysical Research: Space Physics*, *87*(A6), 4469–4475, doi:10.1029/JA087iA06p04469.

Kivelson, M. G., and C. T. Russell (1995), *Introduction to Space Physics*, 1 edition ed., 588 pp., Cambridge University Press; 1 edition (28 April 1995).

Koskinen, H. E. J., and T. I. Pulkkinen (1995), Midnight velocity shear zone and the concept of Harang discontinuity, *Journal of Geophysical Research*, *100*(A6), 9539, doi:10.1029/95ja00228.

Koustov, A. V., and R. A. D. Fiori (2016), Seasonal and solar cycle variations in the ionospheric convection reversal boundary location inferred from monthly SuperDARN data sets, *Annales Geophysicae*, *34*(2), 227–239, doi:10.5194/angeo-34-227-2016.

Lewis, R. V., M. P. Freeman, A. S. Rodger, G. D. Reeves, and D. K. Milling (1996), The electric field response to the growth phase and expansion phase onset of a small isolated substorm, *European Space Agency, (Special Publication) ESA SP*, *299*(389), 109–115.

Lockwood, M., S. W. H. Cowley, and M. P. Freeman (1990), The excitation of plasma convection in the high latitude ionosphere , *95*(A6), 7961–7972, doi:10.1029/JA095iA06p07961.

Longden, N., G. Chisham, M. P. Freeman, G. A. Abel, and T. Sotirelis (2010), Estimating the location of the open-closed magnetic field line boundary from auroral images, *Annales Geophysicae*, *28*(9), 1659–1678, doi:10.5194/angeo-28-1659-2010.

Lui, A. (1996), Current disruption in the Earth's magnetosphere: Observations and models., *J. Geophys. Res*, *101*, 13,067.

Lui, A. T. Y. (1991), A Synthesis of Magnetospheric Substorm Models, *Journal of Geophysical Research: Space Physics*, *96*(A2), 1849–1856, doi:10.1029/90JA02430.

Makita, K., C. I. Meng, and S. I. Akasofu (1983), The Shift of the Auroral Electron Precipitation Boundaries in the Dawn-Dusk Sector in Association with Geomagnetic Activity and Interplanetary Magnetic Field, *J. Geophys. Res.*, *88*(A10), 7967–7981, doi:10.1029/JA088iA10p07967.

Maynard, N. C. (2008), Electric field measurements across the Harang discontinuity, *Journal of Geophysical Research*, *79*(31), 4620–4631, doi:10.1029/ja079i031p04620.

Mende, S., H. Heetderks, H. Frey, M. Lampton, S. Geller, S. Habraken, E. Renotte, C. Jamar, P. Rochus, J. Spann, S. Fuselier, J.-C. Gerard, R. Gladstone, S. Murphree, and L. Cogger (2000a), Far ultraviolet imaging from the IMAGE spacecraft. 1. System design, *Space Science Reviews*, *91*(1/2), 243–270, doi:10.1023/A:1005271728567.

Mende, S. B., H. Heetderks, H. U. Frey, J. M. Stock, M. Lampton, S. P. P. Geller, R. Abiad, O. H. W. Siegmund, S. Habraken, E. Renotte, C. Jamar, P. Rochus, J.-C. Gerard, R. Sigler, and H. Lauche (2000b), Far ultraviolet imaging from the IMAGE spacecraft. 3. Spectral imaging of Lyman alpha and OI 135.6 nm, *Space Science Reviews*, *91*, 287–318, doi:10.1007/978-94-011-4233-5_10.

Meyer-Vernet, N. (2007), *Basics of the Solar Wind*, doi:10.1017/CBO9780511535765.

Milan, S. E., S. Imber, and M. Lester (), Eclat superdarn user guide.

Milan, S. E., T. K. Yeoman, M. Lester, E. C. Thomas, and T. B. Jones (1997), Initial backscatter occurrence statistics from the CUTLASS HF radars, *15*(6), 703–718, doi:10.1007/s00585-997-0703-0.

Milan, S. E., M. Lester, S. W. Cowley, J. Moen, P. E. Sandholt, and C. J. Owen (1999), Meridian-scanning photometer, coherent HF radar, and magnetometer observations of the cusp: A case study, *Annales Geophysicae*, *17*(2), 159–172, doi:10.1007/s00585-999-0159-5.

Milan, S. E., M. Lester, S. Cowley, K. Oksavik, M. Brittnacher, R. Greenwald, G. Sofko, and J.-P. Villain (2003), Variations in the polar cap area during two substorm cycles, *Annales Geophysicae*, *21*, 1121–1140, doi:10.5194/angeo-21-1121-2003.

Milan, S. E., G. Provan, and B. Hubert (2007), Magnetic flux transport in the Dungey cycle: A survey of dayside and nightside reconnection rates, *Journal of Geophysical Research: Space Physics*, *112*(1), 1–13, doi:10.1029/2006JA011642.

Milan, S. E., P. D. Boakes, and B. Hubert (2008), Response of the expanding/contracting polar cap to weak and strong solar wind driving: Implications for substorm onset, *Journal of Geophysical Research: Space Physics*, *113*(9), 1–11, doi: 10.1029/2008JA013340.

Milan, S. E., J. Hutchinson, P. D. Boakes, and B. Hubert (2009a), Influences on the radius of the auroral oval, *Annales Geophysicae*, *27*(7), 2913–2924, doi:10.5194/angeo-27-2913-2009.

Milan, S. E., A. Grocott, C. Forsyth, S. M. Imber, P. D. Boakes, and B. Hubert (2009b), A superposed epoch analysis of auroral evolution during substorm growth, onset and recovery: open magnetic flux control of substorm intensity, *Annales Geophysicae*, *27*(2), 659–668, doi:10.5194/angeo-27-659-2009.

Milan, S. E., J. S. Gosling, and B. Hubert (2012), Relationship between interplanetary parameters and the magnetopause reconnection rate quantified from observations of the expanding polar cap, *Journal of Geophysical Research: Space Physics*, *117*(3), 1–16, doi:10.1029/2011JA017082.

Mishin, V. M., A. D. Bazarzhapov, T. I. Saifudinova, S. B. Lunyushkin, D. S. Shirapov, J. Woch, L. Eliasson, H. Opgenoorth, and J. S. Murphree (1992), Different Methods to Determine the Polar Cap Area, *J. Geomag. Geoelectr.*, *44*(12), 1207–1214, doi: 10.5636/jgg.44.1207.

Mori, D., A. V. Koustov, P. T. Jayachandran, and N. Nishitani (2012), Resolute Bay CADI ionosonde drifts, PolarDARN HF velocities, and cross polar cap potential, *Radio Science*, *47*(3), 1–11, doi:10.1029/2011RS004947.

Nakai, H., and Y. Kamide (2002), Substorm-associated large-scale magnetic field changes in the magnetotail: A prerequisite for "magnetotail deflation" events, *Annales Geophysicae*, *21*(4), 869–879, doi:10.5194/angeo-21-869-2003.

Nakai, H., Y. Kamide, D. A. Hardy, and M. S. Gussenhoven (1986), Time scales of expansion and contraction of the auroral oval, *Journal of Geophysical Research*, *91*(A4), 4437, doi:10.1029/ja091ia04p04437.

Newell, P. T., W. J. Burke, E. R. Sánchez, C.-I. Meng, M. E. Greenspan, and C. R. Clauer (1991), The low-latitude boundary layer and the boundary plasma sheet at low altitude: Prenoon precipitation regions and convection reversal boundaries, *Journal of Geophysical Research: Space Physics*, *96*(A12), 21,013–21,023, doi:10.1029/91ja01818.

Newell, P. T., Y. I. Feldstein, Y. I. Galperin, and C. Meng (1996), Morphology of nightside precipitation, *Journal of Geophysical Research: Space Physics (19782012)*, *101*(A5), 10,737–10,748, doi:10.1029/95JA03516.

Pettigrew, E. D., S. G. Shepherd, and J. M. Ruohoniemi (2010), Climatological patterns of high-latitude convection in the Northern and Southern hemispheres: Dipole tilt dependencies and interhemispheric comparisons, *Journal of Geophysical Research: Space Physics*, *115*(7), 1–15, doi:10.1029/2009JA014956.

Phan, T., L. Kistler, H. Rème, L. Peticolas, S. Fuselier, J. McFadden, M. F. Marcucci, B. Klecker, M. Fujimoto, S. Petrinec, M. Dunlop, G. Paschmann, C. Carlson, R. Lundin, A. Balogh, H. U. Frey, J.-A. Sauvaud, A. Korth, I. Dandouras, C. Mouikis, G. Parks, E. Moebius, S. Mende, S. Frey, and J.-M. Bosqued (2003), Simultaneous Cluster and IMAGE observations of cusp reconnection and auroral proton spot for northward IMF, *Geophysical Research Letters*, *30*(10), n/a–n/a, doi:10.1029/2003gl016885.

Provan, G., M. Lester, S. Mende, and S. E. Milan (2004), Statistical study of high-latitude plasma flow during magnetospheric substorms, *22*, 3607–3624, doi:10.5194/angeo-22-3607-2004.

Reiff, P. H., and J. L. Burch (1985), IMF By-dependent plasma flow and birkeland currents in the dayside magnetosphere, *Journal of Geophysical Research: Space Physics*, *90*, 1595–1609.

Ridley, A. J., and C. R. Clauer (1996), Characterization of the dynamic variations of the dayside high-latitude ionospheric convection reversal boundary and relationship to interplanetary magnetic field orientation, *Journal of Geophysical Research*, *101*(A5), 10,919–10,938, doi:10.1029/JA101iA05p10919.

Ruohoniemi, J., and R. A. Greenwald (2005), Dependencies of high-latitude plasma convection: Consideration of interplanetary magnetic field, seasonal, and universal time factors in statistical patterns., *J. Geophys. Res.*, *110*, doi:10.1029/2004JA010815.

Ruohoniemi, J. M., and K. B. Baker (1998), Large-scale imaging of high-latitude convection with Super Dual Auroral Radar Network HF radar observations, *Journal of Geophysical Research*, *103*(A9), 20,797 —- 20,811, doi:10.1029/98JA01288.

Ruohoniemi, J. M., and R. A. Greenwald (1996), Statistical patterns of high-latitude convection obtained from Goose Bay HF radar observations, *Journal of Geophysical Research: Space Physics*, *101*(A10), 21,743–21,763, doi:10.1029/96JA01584.

Russell, C. T. (1972), The configuration of the magnetosphere, *Critical Problems of Magnetospheric Physics, Proceedings of the Symposium held 11-13 May, 1972 in Madrid, Spain. Edited by E.R. Dyer. Washington, DC: National Academy of Sciences, 1972., p.1.*

Shepherd, S. G. (2014), Altitude-adjusted corrected geomagnetic coordinates: Definition and functional approximations, *Journal of Geophysical Research: Space Physics*, *119*.

Shepherd, S. G., and J. M. Ruohoniemi (2000), Electrostatic potential patterns in the high-latitude ionosphere constrained by SuperDARN measurements, *Journal of Geophysical Research*, *105*(A10), 23,005, doi:10.1029/2000JA000171.

Siscoe, G. L., and T. S. Huang (1985), Polar Cap Inflation and Deflation, *Journal of Geophysical Research*, *90*(A1), 543–547, doi:10.1029/JA090iA01p00543.

Sonnerup, B. (1984), Magnetic field reconnection at the magnetopause: an overview, *Magnetic Reconnection in Space and Laboratory Plasmas, Geophysical Monograph 30*.

Sonnerup, B. U. O. (1974), Magnetopause Reconnection Rate, *Journal of Geophysical Research*, *79*(10).

Sotirelis, T., and P. T. Newell (2000), Boundary-oriented electron precipitation model, *Journal of Geophysical Research*, *105*(A8), 18,655, doi:10.1029/1999JA000269.

Sotirelis, T., J. M. Ruohoniemi, R. J. Barnes, P. T. Newell, R. A. Greemvald, J. P. Skura, and C. I. Meng (2005), Comparison of SuperDARN radar boundaries with DMSP particle precipitation boundaries, *Journal of Geophysical Research: Space Physics*, *110*(A6), 1–12, doi:10.1029/2004JA010732.

Sotirelis, T., M. R. Keller, K. Liou, D. Smith, R. J. Barnes, E. Talaat, and J. B. H. Baker (2017), Testing the expanding-contracting polar cap paradigm, *Journal of Geophysical Research: Space Physics*, *122*(7), 7077–7086, doi:10.1002/2017JA024238.

Svalgaard, L. (1973), Polar cap magnetic variations and their relationship with the interplanetary magnetic sector structure, *Journal of Geophysical Research*, *78*(13), 2064–2078, doi:10.1029/ja078i013p02064.

Thomas, E. G., and S. G. Shepherd (2018), Statistical Patterns of Ionospheric Convection Derived From Mid-latitude, High-Latitude, and Polar SuperDARN HF Radar Observations, *Journal of Geophysical Research: Space Physics*, *123*(4), 3196–3216, doi:10.1002/2018JA025280.

Tsunoda, R. T. (1988), Highlatitude F region irregularities: A review and synthesis, *Reviews of Geophysics*, *26*(4), 719–760, doi:10.1029/RG026i004p00719.

Vampola, A. L. (1971), Access of Solar Electrons to Closed Field Lines, *Journal of Geophysical Research*, *76*(1), 36–43, doi:0.1029/JA076i001p00036.

Weimer, D. R. (1999), Substorm influence on the ionospheric electric potentials and currents, *Journal of Geophysical Research: Space Physics*, *104*(A1), 185–197, doi:10.1029/1998ja900075.

Weimer, D. R. (2001), An improved model of ionospheric electric potentials including substorm perturbations and application to the Geospace Environment Modeling November 24, 1996, event, *Journal of Geophysical Research*, *106*(A1), 407, doi:10.1029/2000JA000604.

Weimer, D. R. (2005), Improved ionospheric electrodynamic models and application to calculating Joule heating rates, *Journal of Geophysical Research: Space Physics*, *110*(A5), 1–21, doi:10.1029/2004JA010884.

Wild, J., and A. Grocott (2008), The influence of magnetospheric substorms on SuperDARN radar backscatter, *Journal of Geophysical Research: Space Physics*, *113*, doi:10.1029/2007JA012910.

Yeoman, T., R. Lewis, H. Khan, S. Cowley, and J. Ruohoniemi (2000), Interhemispheric observations of nightside ionospheric electric fields in response to IMF B-z and B-y changes and substorm pseudobreakup, *Proceedings of the Fifth International Conference on Substorms*, *907*(8), 897–907, doi:10.1007/s005850050006.

Zou, S., L. R. Lyons, C.-P. Wang, J. C. Devlin, J. M. Ruohoniemi, P. C. Anderson, P. L. Dyson, and A. Boudouridis (2009), On the coupling between the Harang reversal evolution and substorm dynamics: A synthesis of SuperDARN, DMSP, and IMAGE observations, *Journal of Geophysical Research: Space Physics*, *114*(A1), n/a–n/a, doi:10.1029/2008ja013449.